

Radiative Effects of Arctic Clouds in Observations and Models

By  
Anne Sledd

A dissertation submitted in partial fulfillment of  
the requirements for the degree of

Doctor of Philosophy  
(Atmospheric and Oceanic Sciences)

at the  
UNIVERSITY OF WISCONSIN-MADISON  
2021

Date of final oral examination: 04/12/2021

The dissertation is approved by the following members of the Final Oral Committee:

Tristan L'Ecuyer, Professor, Atmospheric and Oceanic Sciences

Elizabeth Maroon, Assistant Professor, Atmospheric and Oceanic Sciences

Daniel Vimont, Professor, Atmospheric and Oceanic Sciences

Jeffrey Key, Adjunct Professor, NOAA

Stephen Vavrus, Research Scientist, Nelson Institute Center for Climatic Research

# Abstract

## Radiative Effects of Arctic Clouds in Observations and Models

by Anne Sledd

Decreasing sea ice and snow cover are reducing the surface albedo and changing the Arctic surface energy balance. How these surface albedo changes influence the top of atmosphere albedo and energy balance is a more complex question, though, that depends critically on the modulating effects of the intervening atmosphere and clouds. This thesis investigates the radiative impacts of clouds in the Arctic, particularly on shortwave fluxes, in observations and models. First, satellite observations are used to quantify the contribution of clouds to the planetary albedo and benchmark reanalyses. We find that the atmosphere accounts for the majority (>60%) of the planetary albedo throughout the sunlight months, and clouds further reduce the variability of the planetary albedo that is otherwise observed in the surface albedo. Next we investigate the impact of clouds on absorbed shortwave radiation in the Arctic. In the last two decades, trends in absorbed shortwave are statistically significant if calculated with clear-sky fluxes, but clouds reduce the magnitude of shortwave trends and increase the time needed to discern a statistically significant trend beyond the length of the current record. In the latest generation of climate models, this delaying effect of clouds is often underestimated, if it is present at all. Predicted changes over the 21<sup>st</sup> century of cloud cover and planetary albedo help explain these model discrepancies. Finally, we quantify how clouds can impact the ocean surface energy budget under different CO<sub>2</sub> forcings using a state of the art global climate model. Clouds have a limited impact on upper

ocean temperatures in the pre-industrial environment, but the connection between clouds and SSTs strengthens with higher CO<sub>2</sub> concentrations. Cloud cover is negatively related to fall SST in the Arctic, but the seasonal cycles of sea ice and radiative fluxes determine how effectively clouds can influence SSTs.

*This work is dedicated to myself: my younger self who thought science was boring, my current self who has been doing the work, and my future self who will hopefully put this to good use.*

# Acknowledgements

First I need to thank my advisor, Tristan, for making this possible at all. Thanks for taking a chance on me when I literally had no background in atmospheric science. I've learned so much about how to be a scientist and follow your gut, and I truly appreciate your understanding that there is life outside of graduate school.

I've been fortunate to be part of such a smart research group. Thank you to my fellow L'Ecuyer group members, past and present, for the help and encouragement - Ethan, Andrew, April, Juliet, James. Thank you Marian, Elin, and Julia for support in our Polar Coffee group, both before and during the pandemic. Julia, you were also the best office mate in the before-times. A big thank you to Claire Petterson for her advice and always advocating for me; I low-key think I owe you my career for each time you've told someone to hire me.

Thank you to my committee for input and guidance on my research. I'm grateful to Steve Vavrus and Jeff Key for taking the time to serve on my committee despite not being professors. I'm extra grateful to Elizabeth Maroon for joining my committee before even moving to Wisconsin and for invaluable help ever since. Thank you Dan Vimont for asking the hard questions during committee meetings and also saying the nicest things. Although Jen Kay was not on my committee, my research has also greatly benefited from her help.

Thank you to the AOS staff - Sue, Dee, Christi, Chelsea - for doing all the work that keeps the department running and of course Pete, for computing help over the years.

I wouldn't be any sort of scientist if it weren't for Joel Weisberg, whose astronomy and physics classes in college taught me how interesting science can be.

This work was funded by NASA. Computing resources for parts of this work were provided by NCAR, CISL and the CESM Polar Climate Working Group.

I feel lucky for all the friends and family that have supported me for the years. In particular, Harper and Olivia - thank you for all the love and rambling phone calls. All the shared hikes and dinners with Julia, James, Nick, and Charlotte have made my time here so much more enjoyable. Thank you Maggie, for being a role model as well as a sister - the familial support and commiseration have been invaluable. Thanks to Connie and Fritz for always opening up their home. Thank you also to the therapists that have quite literally helped keep me sane over the years.

Finally, I am grateful for my husband, Sam. I'm so appreciative you joined me in Wisconsin, and I can't wait to see where our next adventure takes us.

# Contents

<b>Abstract</b>	<b>i</b>
<b>Dedication</b>	<b>iii</b>
<b>Acknowledgements</b>	<b>iv</b>
<b>Contents</b>	<b>vi</b>
<b>List of Figures</b>	<b>ix</b>
<b>List of Tables</b>	<b>xvi</b>
<b>1 Introduction</b>	<b>1</b>
<b>2 How Much Do Clouds Mask the Impacts of Arctic Sea Ice and Snow Cover Variations? Different Perspectives from Observations and Reanalyses*</b>	<b>6</b>
2.1 Preface . . . . .	7
2.2 Methods . . . . .	8
2.2.1 Datasets . . . . .	8
2.2.1.1 Reanalyses . . . . .	10
2.2.2 Surface Partitioning . . . . .	14
2.2.3 Albedo Partitioning . . . . .	18
2.3 How does planetary albedo respond to surface cover? . . . . .	20
2.3.1 Effects of surface cover on TOA albedo . . . . .	20
2.3.2 Cloud Modulation of Ice-Albedo Relationships . . . . .	25
2.3.3 Representation in Reanalyses . . . . .	31
2.4 Discussion and Conclusions . . . . .	39
<b>3 The influence of clouds on absorbed solar radiation trends and detectability in observations and CMIP6</b>	<b>44</b>
3.1 Preface . . . . .	44
3.2 Data . . . . .	46
3.2.1 Observations . . . . .	46

3.2.2	CMIP6	48
3.3	Uncertainty in Forced and Natural Arctic Solar Absorption Variations in CMIP6 Models	50
3.3.1	Methods	50
3.3.1.1	Time to Emergence	50
3.3.1.2	Synthetic Time Series	52
3.3.1.3	Accumulated Absorbed Shortwave Radiation	54
3.3.2	Results and Discussion	58
3.3.2.1	A signal to noise problem	63
3.3.2.2	Impact of sea ice on TTE	69
3.3.2.3	Inconsistent Cloud Impacts on TTE	71
3.3.2.4	$SW_{acc}$ as a Proxy for Arctic and Global Change	75
3.3.3	Conclusions	77
3.4	A closer look at observations of the "New Arctic"	79
3.4.1	Results	80
3.4.2	Discussion and Conclusions	91
<b>4</b>	<b>Connections between Arctic TOA albedo and SW trends in CMIP6</b>	<b>95</b>
4.1	Preface	95
4.2	Methods	96
4.3	Results and Discussion	97
4.3.1	CMIP6 albedo partitioning mean state	97
4.3.2	Sea ice and SW albedos	101
4.3.3	SW albedos and trend detection	107
4.3.3.1	$SW_{acc}$ TTE and Equilibrium Climate Sensitivity	110
4.4	Conclusions	111
<b>5</b>	<b>The influence of clouds on Arctic SST in CESM2</b>	<b>113</b>
5.1	Preface	113
5.2	Methods	115
5.2.1	CESM2	115
5.2.2	Season definitions	116
5.3	Results and Discussion	117
5.4	Preliminary Conclusions and Future Work	123
<b>6</b>	<b>Synthesis</b>	<b>125</b>
<b>A</b>	<b>Supplemental Figures</b>	<b>128</b>
A.1	Supplemental Figures for Section 3.3	128
A.2	Supplemental Figure for Section 3.4	132

**Bibliography**

## List of Figures

2.1	a) Monthly average snow cover area (blue) and sea ice area (red) for 2002-2012 calculated from NSIDC SIC and SCF for the Arctic defined in Chapter 2. (b) June snow cover area (blue) and September sea ice area (red). . . . .	9
2.2	(a) Area in the Northern Hemisphere where 2002-2015 average 2-m air temperature from AIRS is less than or equal to 0. NCEP land fraction is used to define land ( $\leq 0.5$ ) and ocean ( $> 0.5$ ). This definition of the Arctic removes oceans north of the Atlantic that are continually ice free and behave differently than the rest of the Arctic. In this definition of the Arctic, 45% of area is ocean and 55% is land. (b) Fractional area of surface partitions averaged over 2002-2012 from NSIDC. All ice is defined as ocean grid cells with sea ice concentration (SIC) $> 0.85$ , no ice refers to grid cells with $\leq 0.15$ SIC, and all other grid cells are considered as having some ice. The same partitions are applied to land grid cells using snow cover fraction. . . . .	16
2.3	The Arctic radiative energy budget (CERES-EBAF) for (a) clear-sky and (b) all-sky conditions. Area averaged values over the domain presented in Fig. 2.2a from 2002-2012 are given in black. Fluxes are further partitioned by surface cover as follows: all sea ice (purple), some sea ice (red), no sea ice (blue), all snow (teal), some snow (gray), no snow (green). . . . .	17
2.4	Annual cycles of (a) top of atmosphere (TOA) albedo, (b) surface albedo, (c) atmospheric contribution to TOA albedo, and (b) surface contribution to TOA albedo averaged over the Arctic (solid black) and surface partitions (colored lines) for 2002-2012 from CERES. . . . .	21
2.5	Average monthly maps of snow cover and sea ice fractions from NSIDC and albedos and TOA albedo contributions calculated from CERES all-sky fluxes. Months are averaged over 2002-2012. Only March through September are shown as they account for approximately 95% of annual solar insolation in the Arctic. . . . .	22

2.6	Cloud impacts on atmospheric and surface contributions to the TOA albedo are calculated using CERES all-sky and clear-sky fluxes. The clear-sky value is subtracted from the all-sky value and multiplied by the solar insolation at the TOA. These values correspond to SW radiation directly reflected by clouds (atmospheric contribution) (a) and the amount of SW that would have been reflected if clouds were not present (surface contribution) (b). Their annual cycles are plotted for Arctic-wide averages (solid black line) and various surface partitions (colored lines) for 2002-2012. . . . .	25
2.7	Arctic-wide averages of (a) top of atmosphere (TOA) albedo, (b) surface albedo, (b) atmospheric contribution to TOA albedo, and (c) surface contribution to TOA albedo plotted against the average sea ice concentration for individual months (March-September) during 2002-2012. Albedos and TOA albedo contributions are calculated from CERES all-sky fluxes. Lines of best fit are calculated using a linear least-squares regression, the slopes of which are given in Table 2.3. . . . .	27
2.8	Same as Fig. 2.7 but with snow cover fraction. . . . .	30
2.9	Average monthly albedos and TOA albedo contributions for CERES and reanalyses averaged over the Arctic for 2002-2012. Error in observational albedos and contributions (shown in grey) is propagated from uncertainties in CERES fluxes. . . . .	32
2.10	Comparison of albedos and TOA albedo contributions between CERES and reanalyses partitioned by surface cover. Albedos and TOA albedo contributions are averaged over March-September, as these are the months that account for 95% of solar insolation in the Arctic. Error for observational albedo is propagated using CERES flux uncertainties. . . . .	34
2.11	Cloud impacts on atmospheric and surface contributions to TOA albedo. These values correspond to the amount of reflected SW due to clouds and the amount of SW that would have been reflected if clouds were not present. Top: annual cycles averaged over the Arctic for 2002-2012. Bottom: albedos and TOA albedo contributions are averaged over March-September from 2002-2012 for different surface partitions. . . . .	35
2.12	Total cloud fraction averaged over the Arctic up to 82 for 2007-2010. . . . .	37
2.13	Sensitivity of (a) TOA albedo, (b) surface albedo, (c) atmospheric contribution, and (d) surface contribution to sea ice concentration in reanalyses and observations for two months: June (circles) and September (triangles). . . . .	38

- 3.1 Monthly deseasonalized anomalies for Arctic surface (SFC) and top of atmosphere (TOA) albedos and Northern Hemisphere (NH) sea ice extent (SIE) from 2001-2017. Albedos are calculated using fluxes from CERES-EBAF Ed 4.1 and SIE estimates are from the NSIDC. Dashed vertical lines mark September 2007 and 2012, the lowest SIE on record. The surface albedo anomalies closely track the SIE anomalies and both exhibit clear negative trends over this time period. TOA albedo anomalies, on the other hand, are often decoupled from the surface and the trend is much more difficult to discern. . . . . 48
- 3.2 Trend detection using synthetic time series of surface clear-sky ( $SFC_{clr}$ ) accumulated shortwave ( $SW_{acc}$ ) over the Arctic from CERES-EBAF. (a) Synthetic time series (grey) are generated based on the variance and one-lag autocorrelation of the detrended CERES observations shown in black. A linear trend based on the CERES record is added to time series to generate the ensemble shown in light blue. A single realization from the resulting ensemble is highlighted in red. (b) For each synthetic time series, the linear trend is calculated from subsets of time periods increasing in length, e.g.  $[0,1]$ ,  $[0,2]$ ,... $[0,T]$ , where  $T$  is the full length of the time series. Trends calculated over the red time series in (a) are again highlighted. Initially trends can vary greatly, oscillating between positive and negative values before leveling off around the "true" trend, given by the solid black line. (c) When the trend is at least twice as large as the uncertainty, shown as the solid black line at  $|\frac{\hat{\omega}}{\sigma_{\hat{\omega}}}| = 2$  for the 95% confidence level, it is deemed to have "emerged". Theoretical values of time to emergence (TTE) are shown in (d) with ranges of variability ( $\sigma_N$ ), one-lag autocorrelation ( $\phi$ ), and trend found in models and observations. . . . . 53
- 3.3 Anomalies of accumulated shortwave ( $SW_{acc}$ ) at the top of the atmosphere with clouds ( $TOA_{all}$ ) (top) and the surface without clouds ( $SFC_{clr}$ ) (bottom) in CMIP6 models and observations (CERES-EBAF). The ensemble mean from CMIP6 is shown in black. Anomalies for CMIP6 models are relative to 1900-1999, and those from observations are calculated relative to 2001-2018 but shifted to align with the CMIP6 base state (the CMIP6 ensemble mean from 2001-2018 is calculated and added to the CERES anomalies). For a given model, clear-sky  $SW_{acc}$  anomalies at the surface are greater than all-sky anomalies at the TOA. However, there are large differences between models both in terms of the magnitude and variability of anomalies. . . . . 56

- 3.4 Autocorrelation functions (ACF) for accumulated shortwave ( $SW_{acc}$ ) anomalies at the top of the atmosphere with clouds ( $TOA_{all}$ ) (top row) and the surface without clouds ( $SFC_{clr}$ ) (bottom row) in observations (CERES-EBAF) (left column) and a typical climate model, MRI-ESM2-0 (right column). While no autocorrelations are significant at any lags (95% confidence interval shown as the dashed line), this may be in part due to the short record (18 years). When ACF are calculated over longer time periods in CMIP6 models, shown here for 1900-1999,  $SW_{acc}$  anomalies usually appear as red or white noise. . . . . 57
- 3.5 (a) Mean time to emergence (TTE) of accumulated shortwave ( $SW_{acc}$ ) trends from 300 synthetic time series based on CERES-EBAF observations and CMIP6 models. Variance and autocorrelation are calculated over 2001-2018 and forced with trends over 2001-2100 for CMIP6 models and 2001-2018 for CERES-EBAF. Error bars represent one standard deviation around the mean TTE. Two shared societal pathways (SSP) are shown: a "middle of the road" future (SSP245) and a "business as usual" future (SSP585). Observations suggest that trends in clear-sky surface ( $SFC_{clr}$ )  $SW_{acc}$  have emerged in the 18 year observational record while all-sky top of atmosphere ( $TOA_{all}$ )  $SW_{acc}$  will require more years of observations to discern. (b) TTE calculated from synthetic time series with variability based on CERES-EBAF forced with trends from CMIP6 models used in (a). The difference between (a) and (b) shows the impacts of model internal variability on  $SW_{acc}$  TTE. Values from bar plots are given in Tables 3.3 and 3.4 . . . . . 60
- 3.6 Time to emergence (TTE) and statistical properties of all-sky top of atmosphere ( $TOA_{all}$ ) and clear-sky surface ( $SFC_{clr}$ ) accumulated shortwave ( $SW_{acc}$ ) used to calculate TTE from four different time periods. Solid lines represent values from CERES-EBAF. TTE derived from EC-Earth3 (left) is generally independent of the time period used to calculate it in spite of large variations in  $SW_{acc}$  one-lag autocorrelation. Meanwhile, GFDL-ESM4 (right) TTEs vary by more than a factor of two between time periods. This variability is mostly due to differences in noise and autocorrelation as the  $SW_{acc}$  trends are fairly consistent, regardless of the starting year. While only time periods from SSP245 are shown, the results are consistent when using SSP585. 64
- 3.7 Mean time to emergence (TTE) and accumulated shortwave ( $SW_{acc}$ ) statistical properties from 2001-2018 (noise and autocorrelation) and 2001-2100 (trend) in CERES-EBAF and CMIP6. Error bars represent the  $2\sigma$  range of uncertainty in observations. The signal to noise ratio (SNR) has the strongest relationship to TTE as it represents the strength of the trend against the variability, both with clouds at the top of the atmosphere ( $TOA_{all}$ ) and without clouds at the surface ( $SFC_{clr}$ ). Clouds reduce the magnitude of  $SW_{acc}$  trends, and sometimes the noise, within a given model. In observations, clouds significantly reduce the SNR, but for most models in CMIP6 they only have a moderate effect on SNR. . . . . 67

3.8	Relationship between mean time to emergence (TTE) for accumulated shortwave ( $SW_{acc}$ ) and the statistical properties of sea ice area (SIA) averaged over the melt season (March-September) from 2001-2018 (noise and autocorrelation) and 2001-2100 (trend). Error bars represent the $2\sigma$ range of uncertainty in observations. The greater the SIA decline, the faster the $SW_{acc}$ trend emerges, regardless of cloud cover. SIA trend and signal to noise ratio (SNR) both impact $SW_{acc}$ at the surface without clouds ( $SFC_{clr}$ ) and the top of the atmosphere with clouds ( $TOA_{all}$ ). SIA noise is related to $SFC_{clr}$ TTE but has a minimal influence on $TOA_{all}$ TTE. . . . .	70
3.9	Dependence of the ratio of $TOA_{all}$ to $SFC_{clr}$ accumulated shortwave ( $SW_{acc}$ ) TTE to $SW_{acc}$ statistical properties. The shaded region represents TTE ratios below the minimum ratio if one more year of observations proved the $TOA_{all}$ trend significant. The relative strength of the signal to noise ratio (SNR) with and without clouds is negatively related to the relative length of TTE. When the TOA and surface $SW_{acc}$ trends are similar, the TOA $SW_{acc}$ trend may emerge sooner if the natural variability at the surface is larger than that at TOA. This relationship holds for both shared societal pathways (SSP). Most models underestimate the influence of clouds damping the $SW_{acc}$ trend and SNR has on the difference in TTE. . . . .	72
3.10	Role of 21st century cloud fraction (CF) trends in modulating the ratio of $TOA_{all}$ to $SFC_{clr}$ accumulated shortwave TTE. The atmosphere, and clouds in particular, account for much of the planetary albedo both globally and in the Arctic. Models that predict decreasing cloud cover over the 21st century amplify the effect of reduced surface albedo from sea ice on TOA $SW_{acc}$ by both lowering the atmospheric contribution to the planetary albedo and revealing dark open ocean. This impact is linked to the relative strength of $SW_{acc}$ trends and signal to noise ratio (SNR) with and without clouds in both shared societal pathways (SSP). . . . .	74
3.11	Relationships between (a) Arctic warming, (b) global warming, and (c) Arctic amplification (AA) and $TOA_{all}$ TTE from CMIP6. Temperature changes ( $\Delta T$ ) are derived from the difference in annual average surface temperature of 2081-2100 relative to 2001-2018. The time to emergence of all-sky absorbed SW radiation trends in the Arctic may be a good proxy for both Arctic and global temperature change in both warming pathways. Since sea ice loss drives much of the inter-model variability of TTE, models with more warming have quicker sea ice loss and lower TTE, as seen in (a). A similar relationship appears to hold for global temperature (b) but not AA (c). . . .	76
3.12	Mean accumulated SW ( $SW_{acc}$ ) over 2000-2019 from CERES-EBAF, calculated with top of the atmosphere clear-sky (a) and all-sky (b) fluxes. . . . .	80
3.13	Average sea ice concentration (SIC) and snow cover fraction (SCF) for March through September from 2000-2019 (a,d) and corresponding trends (c,d). Trends are calculated using linear least-squares regression. . . . .	82

3.14	Anomalies of accumulated SW from CERES-EBAF over ocean (navy) and land (pink) areas in the Arctic under all and clear-sky conditions. . . . .	84
3.15	Accumulated SW trends (a,c), standard deviations (b,e) and signal to noise ratios (SNR) (c,f) calculated with all-sky (a-c) and clear-sky (d-f) fluxes from CERES-EBAF over 2000-2019. Differences between all-sky and clear-sky conditions are shown in (g-i). SNR is calculated by dividing the trend by the standard deviation. Stippling represents grid boxes where trends have emerged in the observational record with 95% confidence. Note that trends and standard deviations have units of $\text{MJm}^{-2}$ since they have not been weighted by area. . . . .	85
4.1	Monthly means (left column) and standard deviations (right column) of TOA and surface albedos and TOA albedo partitions in CMIP6 during the melt season, March through September. Values are calculated from historical forcing years 1900-2015 and averaged over the area north of the Arctic Circle. . . . .	98
4.2	Fraction of the TOA albedo contributed by the atmosphere (a) and surface (c) over 2000-2015 in CMIP6 and observations (CERES-EBAF), March through September. Differences between historical and end of century (2080-2100) fractional TOA contributions are shown in (b) and (d), calculated with SSP585. . . . .	100
4.3	Correlations between albedos and SIA as they relate to each other during summer months. Correlation coefficients are calculated over the historical period, 1900-2015, using detrended anomalies. Correlation coefficients with magnitudes greater than 0.18 are considered statistically significant using a t-test with 95% significance level; shading in c) indicates statistically insignificant correlations. . . . .	103
4.4	Sensitivity of TOA and surface albedos to sea ice area (SIA) in summer months. Sensitivity is found from the regression of each albedo against SIA for a given month across the historical time period, 1900-2015 (a) and the overlap with the CERES observational record, 2000-2015 (b). . . . .	104
4.5	Regressions of TOA albedo sensitivity to SIA against the sensitivity to SIA of the surface albedo and TOA albedo partitions. Slopes that are statistically insignificant ( $p > 0.05$ ) are indicated by translucent shading, notably in c). . . . .	105
4.6	Sensitivity of TOA albedo to SIA as it relates to the ratio of all-sky to clear-sky $\text{SW}_{acc}$ TTE in September calculated with SSP585. . . . .	107
4.7	Total SW reflected due to the atmosphere ( $\text{Atm SW}_{ref}$ ) as it relates to accumulated SW ( $\text{SW}_{acc}$ ) ratios of all-sky to clear-sky for a) means, b) standard deviations, and c) trends and time to emergence (TTE). $\text{SW}_{acc}$ TTE are calculated using SSP585 over 2000-2100. . . . .	109

4.8 Relationship between all-sky  $SW_{acc}$  TTE and equilibrium climate sensitivity (ECS) in CMIP6. ECS values are from Zelinka et al. (2020), calculated using the Gregory method. Solid blue line is the mean all-sky  $SW_{acc}$  TTE from CERES, and blue shading represents  $/pm2$  standard deviations of TTE. . . . . 110

5.1 Daily time series of sea ice concentration (SIC; navy) and sea surface temperature (SST; red) for one grid cell ( $52^{\circ}N$ ,  $280^{\circ}E$ ) of one year in the pre-industrial control simulation. The last day SIC is greater than or equal to 0.95, the melt onset, is marked by the bright blue line, and the last day SIC is greater than or equal to 0.15, the heat onset, is marked by the purple line. The day of maximum SST is shown by the orange line. This figure is adapted from Steele and Dickinson (2016). . . . . 117

5.2 a) Annual cycle of ocean heat budget terms, summed over ocean grid cells poleward of  $60^{\circ}N$  for the upper 50m in pre-industrial control. b) Individual terms of the total surface flux term in (yellow line in a). Shading represents one and two standard deviations. . . . . 118

5.3 Sensitivity of downwelling LW (a) and SW (b) for total grid box cloud liquid water path (LWP) throughout the year. Sensitivity is calculated from the regression of all ocean grid cells north of  $60^{\circ}$  for each day of the year. . . . . 119

5.4 PI-control ( $CO_2=287.4ppm$ ) mean date of melt onset (a), heat onset (b), and length of heat season (c). Differences are given for near future ( $CO_2=424ppm$ ; d-f) and  $4xCO_2$  (1139ppm; g-i) values. . . . . 120

5.5 Correlations between  $SST_{max}$  and day of melt onset (DOY SIC<0.95; a,e,i), day of heat onset (DOY SIC<0.15; b,f,j), cloud LWP during the melt season ( $LWP_{melt}$ ; c,g,k) and heat season ( $LWP_{heat}$ ; d,h,l) for pre-industrial (287.4 ppm; a-d), near future (424 ppm; e-h) and  $4xPI$ -control (1139 ppm; i-l)  $CO_2$  levels. Stippling represents statistically significant correlations using a t-test with 95% confidence. . . . . 121

A.1 Maps of Arctic regions. (left) Area considered land or ocean in the Arctic based on regridded land fraction variable from NCCEP reanalysis. (right) Individual land areas and seas used in the text. Eurasia is the total area encompassing Europe and Siberia. NCEP land masks from ArORIS are also used to determine the individual land regions. Marginal seas are based on the Multisensor Analyzed Sea Ice Extent regions from the National Snow and Ice Data Center interpolated to the ArORIS grid. . . . . 132

# List of Tables

2.1	Summary of selected reanalyses characteristics. . . . .	11
2.2	Continued summary of selected reanalyses characteristics. . . . .	11
2.3	Sensitivities of TOA and surface albedos and albedo contributions to variations sea ice concentration (SIC) for March through September. Slopes $[\Delta \text{albedo}]/[\Delta \text{SIC}]$ , are found using linear least-squares regression in a given month, shown in Fig. 2.7. $R^2$ values are given in parentheses. Statistically significant relationships ( $p < 0.05$ ) are bold. . . . .	29
2.4	Same as Table 2.3 but using snow cover fraction instead of sea ice concentration. . . . .	30
2.5	Sensitivity of albedos and TOA albedo contributions to SIC for observations and reanalyses in dimensionless units $[\Delta \text{albedo}]/[\Delta \text{SIC}]$ . $R^2$ values are given in parentheses. Statistically significant relationships ( $p < 0.05$ ) are bold. . . . .	39
3.1	Models included from phase six of the Coupled Model Intercomparison Project. . . . .	49
3.2	CERES-EBAF properties for all-sky top of atmosphere ( $\text{TOA}_{all}$ ) and clear-sky surface ( $\text{SFC}_{clr}$ ) accumulated shortwave ( $\text{SW}_{acc}$ ). Noise, one-lag autocorrelations and trends are from 2001-2018. Mean time to emergence (TTE) is calculated from 300 synthetic time series using these statistics, with standard deviations given in parentheses. . . . .	58
3.3	Mean time to emergence (TTE) from 300 synthetic time series based on models only with noise and autocorrelation calculated from 2001-2018 forced with trends from 2001-2100. Standard deviations are given in parentheses. . . . .	61
3.4	Mean time to emergence (TTE) from 300 synthetic time series based on noise and autocorrelation from observations (CERES-EBAF) forced with trends from CMIP6 models over 2001-2100. Standard deviations are given in parentheses. . . . .	62
3.5	Characteristics of all-sky accumulated shortwave radiation over the Arctic domains defined in Figure S1. The TTE is the mean number of years needed for a trend emerge from 300 synthetic time series based on the trend, standard deviation and autocorrelations. The standard deviation of TTE from the synthetic ensemble is given in parentheses. Trends that have emerged in the current observational record, are noted with asterisks. Regions are noted with a + if all-sky and clear-sky mean TTE are statistically different using a students t-test with $p < 0.05$ . . . . .	88

3.6 As in Table 3.5 but for clear-sky  $SW_{acc}$  . . . . . 89

# Chapter 1

## Introduction

The Arctic is one of the most rapidly changing regions on Earth. Sea ice loss has negative trends for all months over the beginning of the satellite era (Onarheim et al., 2018) with many regions transitioning from perennial to seasonal ice cover in recent years (Comiso, 2002). The remaining sea ice is younger and thinner (Lindsay and Schweiger, 2015, Stroeve et al., 2012) as its decline accelerates (Comiso et al., 2008). On land, snow cover is also declining, with longer melt seasons (Wang et al., 2018) and a "greener" Arctic (Myers-Smith et al., 2020, Zhu et al., 2016). These surface cover changes coincide with increasing surface temperatures, almost 2°C over the last century (Box et al., 2019), that are 2-3 times greater than the global average, a phenomenon known as Arctic Amplification (AA) (Serreze et al., 2009). AA is driven by various feedback mechanisms that manifest themselves through changes in the Arctic energy budget (Serreze and Barry, 2011). The observed changes in surface cover impact the surface-atmosphere heat and moisture exchanges (Serreze and

Barry, 2011) and have created a fundamentally different environment, termed the “New Arctic” (Carmack et al., 2015).

We can understand the evolving new Arctic by studying the energy budget, the balance of energy entering and leaving the Arctic system. At the top of the atmosphere (TOA), the energy balance is determined solely by the exchange of incoming shortwave (SW) and outgoing longwave (LW) radiative fluxes. The amount of SW radiation that is absorbed versus reflected is, in turn, determined by the planetary, or TOA, albedo. At the surface, latent and sensible heat fluxes also play a role, offsetting some of the excess SW absorption in summer and fall when sea ice extent is reduced. While the surface and TOA are linked, only excess energy at the surface can melt sea ice and snow or heat the ocean. Decreases in sea ice extent and snow cover have, in turn, been linked to decreases in surface and TOA albedos over Arctic waters in observations (Gorodetskaya et al., 2006, Pistone et al., 2014, Riihelä et al., 2013). Sea ice has a much higher albedo than open ocean, so when sea ice melts the ocean absorbs more SW radiation. More SW radiation at the surface warms the ocean and further melts additional sea ice (Curry et al., 1995) both by increasing maximum sea surface temperatures (Steele et al., 2008) and heat release in fall and winter that delays sea ice growth (Tietsche et al., 2011), creating the ice-albedo feedback central to AA (Screen and Simmonds, 2010).

Yet while sea ice and snow play critical roles in the Arctic energy balance, their influence is strongly modulated by the atmosphere and, in particular, cloud cover (Sedlar et al., 2011). Clouds affect both LW and SW radiation throughout the atmospheric column. They can

decrease the SW radiation that reaches the surface as well as increase the downwelling LW radiation. Thus, clouds modulate surface melting, warming the surface by trapping thermal radiation or cooling it by reflecting solar radiation (Intrieri et al., 2002, Perovich, 2018). The Arctic has high cloud cover throughout the year, typically greater than 65% Comiso and Hall (2014), and the impact of clouds on SW is particularly large during summer when the sun shines continuously above the Arctic Circle, and clouds further reduce the strength of the ice-albedo feedback (Hwang et al., 2018, Soden et al., 2008).

However, while our knowledge of Arctic cloud properties has improved over the past decades with increased satellite observations (Kay et al., 2016), the precise magnitude of the modulating influence of clouds is still unresolved. Because clouds strongly influence the planetary albedo and, therefore, how much SW radiation reaches the surface, the future of clouds is critical to the future of the Arctic climate (Kay et al., 2016). Observational studies have found some evidence that increased cloud cover may offset decreases in surface albedo in the Arctic (Kattlein et al., 2017, Kato et al., 2006), although trends in cloud cover are small and both regionally and seasonally dependent (Kay and Gettelman, 2009, Letterly et al., 2018, Wang et al., 2012). These studies have also relied on satellites with passive sensors that struggle to identify cold bright clouds over cold bright surfaces in the Arctic. While data from active sensors, e.g. radar and lidar aboard CloudSat and CALIPSO, have greatly improved our understanding of cloud processes in the Arctic (Kay and L'Ecuyer, 2013, Morrison et al., 2018) they have only been in orbit since 2006 and suffer from limited nadir sampling.

An abundance of data would be ideal to study these problems, but data are more difficult to gather in the Arctic than at lower latitudes. Due to harsh environmental conditions, continuous ground observations are relatively sparse. While field campaigns provide invaluable ground truth they are limited in time and space. Satellites have improved spatial and temporal coverage. Unfortunately, satellite observations do not all cover the same time periods or all variables that are desired. As such, reanalyses are commonly used in studying the Arctic to fill in the gaps of observations, but their accuracy is often questioned given the lack of independent observations to validate them, (e.g. Huang et al., 2017, Lindsay et al., 2014, Tjernström et al., 2008). In addition, global climate models (GCMs), allow the bulk effects of various forcing and feedback mechanisms to be analyzed with a plethora of prognostic and diagnostic variables that span for far longer time periods than observations. However, studying the future of polar climate using GCMs presents its own challenges due to ongoing difficulties accurately representing modern day cloud processes and feedbacks (Dolinar et al., 2015, Li et al., 2013). Each model contains its own biases that influence what conclusions can be drawn from it (Bintanja and Krikken, 2016). Differences in cloud parameterizations have thus led to biases, relative to satellite and ground observations, in the SW energy budget in GCMs (Gorodetskaya et al., 2006). While progress has been made studying cloud feedbacks in the Arctic (e.g. Morrison et al., 2019), the challenge of realistically representing clouds persists across generations of GCMs (Vignesh et al., 2020), casting uncertainty on projected rates of AA and accompanying Arctic sea ice loss. As with all data sources, one must be aware of their limitations to draw accurate conclusions.

In this work we unpack the effects of clouds on radiative fluxes in the Arctic, largely focusing on reflected and absorbed SW radiation. In Chapter 2 we quantify the surface and atmospheric contributions to the TOA albedo and compare values over different surface types based on snow and sea ice cover. The masking effect of clouds as seen from the TOA is compared across surface types, and further used to explain why the TOA albedo behaves differently than the surface albedo. These values are calculated with broadband fluxes from satellite observations, and the results are used to evaluate several reanalyses. In Chapter 3 we examine how clouds impact trends of absorbed SW radiation in observations and phase six of the Climate Model Intercomparison Project (CMIP6). A statistical framework is employed to determine how many years of observations are needed to determine a trend is statistical significant, given the interannual variability. An additional section dives into the regional impacts of clouds on SW absorption in observations, using the same statistical framework. Chapter 4 connects the two earlier chapters. The albedo partitioning scheme is applied to GCMs and compared to observations. Their representations of albedos and cloud masking are then related to the emergence of SW absorption trends. Finally, in Chapter 5 we turn to the implications of cloud masking on ocean warming. We investigate if clouds can influence sea surface temperatures in the Arctic Ocean using a state of the art climate model. We end by discussing the broader implications of this work and future directions in Chapter 6.

## **Chapter 2**

# **How Much Do Clouds Mask the Impacts of Arctic Sea Ice and Snow Cover Variations? Different Perspectives from Observations and Reanalyses\***

---

\*This is a lightly modified version of: Sledd, Anne, and Tristan L'Ecuyer. "How much do clouds mask the impacts of Arctic sea ice and snow cover variations? Different perspectives from observations and reanalyses." *Atmosphere* 10.1 (2019): 12.

## 2.1 Preface

This chapter quantifies how clouds modulate the TOA albedo and sea ice loss using satellite observations and compares the results with reanalyses. The TOA albedo is determined by both the surface and the atmosphere, the latter being heavily influenced by clouds (Stephens et al., 2015). Past studies have partitioned the TOA albedo into surface and atmospheric components both globally and at high latitudes (Donohoe and Battisti, 2011, Qu and Hall, 2005). Observations reveal that the atmosphere dominates the TOA albedo across the Earth, even in the Arctic where the surface albedo is quite high. Although the surface does not make the largest contribution to the TOA albedo, it is responsible for the majority of *variability* in the Arctic TOA albedo. From Qu and Hall (2005), more than 50% of TOA albedo interannual variability is due to the changes in the surface albedo. Since the atmospheric contribution is dominated by clouds, the albedo partitioning scheme from Donohoe and Battisti (2011), discussed next, can be further used to quantify the effects of clouds on TOA albedo response to changing surface cover in the Arctic and evaluate their representation in reanalyses.

This chapter seeks to answer two fundamental questions: How do clouds modulate the impact of surface cover changes on the TOA albedo? And how well are these effects captured in modern reanalyses that are often used in polar climate studies? We partition the surface based on sea ice and snow cover to show the effects of surface cover on the energy balance over a time period with large surface cover variability. The surface partitioning is further applied to the TOA albedo and its contributions to show their sensitivities to changes in

surface cover. We use new metrics to quantify the effects of clouds on the TOA albedo by comparing the all-sky and clear-sky TOA albedo contributions. These metrics are further used to evaluate five modern reanalyses in their representations of clouds and surface cover feedbacks in the Arctic.

## 2.2 Methods

### 2.2.1 Datasets

This study utilizes the Arctic Observations and Reanalysis Integrated System (ArORIS), a collection of satellite, in situ and reanalysis datasets focused on the Arctic and created to support Arctic climate research (Christensen et al., 2016). All data in ArORIS is re-gridded to a uniform 2.52.5rid and averaged to monthly timescales. We use radiative fluxes from the Clouds and Earth’s Radiant Energy System Energy Balance and Filled (CERES-EBAF) version 2.8 on board the Terra and Aqua NASA satellites. TOA fluxes in the CERES-EBAF dataset are adjusted within their ranges of uncertainty to be consistent with global ocean heat uptake from in situ ocean observations (Kato et al., 2013). Errors in gridded downwelling SW fluxes at the TOA are  $0.5 \text{ Wm}^{-2}$  and  $5 \text{ Wm}^{-2}$  in outgoing all-sky SW irradiance for January—June 2002 and  $4 \text{ Wm}^{-2}$  thereafter (CERES, 2014, L’Ecuyer et al., 2015). Outgoing clear-sky SW irradiance has an estimated error of  $2.6 \text{ Wm}^{-2}$ . At the surface, uncertainties are  $11 \text{ Wm}^{-2}$  in both downwelling and reflected SW fluxes (CERES, 2020). Total cloud fraction is derived from the CloudSat 2B-GEOPROF-LIDAR product that utilizes a

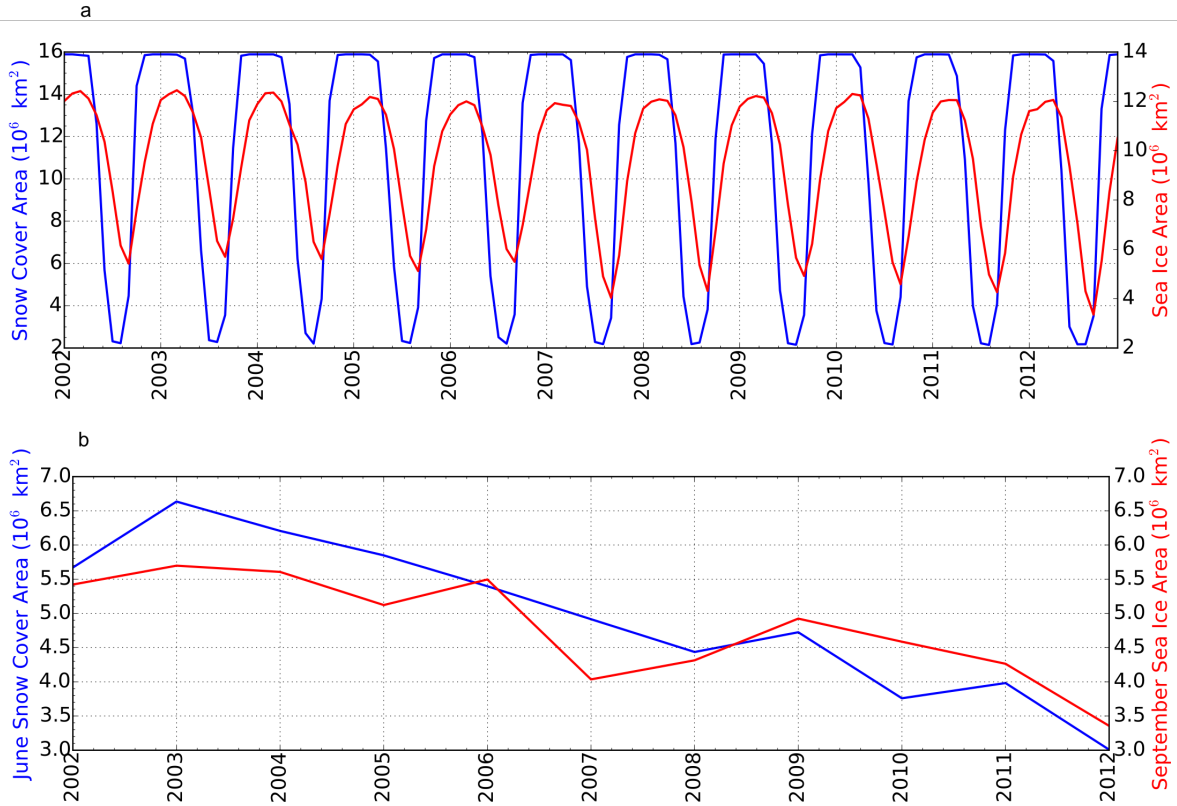


FIGURE 2.1: a) Monthly average snow cover area (blue) and sea ice area (red) for 2002-2012 calculated from NSIDC SIC and SCF for the Arctic defined in Chapter 2. (b) June snow cover area (blue) and September sea ice area (red).

combination of Cloud Profiling Radar (CPR) and Cloud-Aerosol Lidar with Orthogonal Polarization (CALIOP) observations. These active sensors are able to detect clouds over bright surfaces and surface inversions that are common in the Arctic (Tanelli et al., 2008, Winker et al., 2009). CloudSat/CALIPSO data are only available for 2007-2010 over 82-82. For this work we use the years 2002-2012, corresponding to the period for which CERES was available in ArORIS. This period spans a time of high sea ice variability when the September minimum sea ice extent has ranged from 3.4 to 6.0 million  $\text{km}^2$ . Figure 2.1 shows the variability of monthly sea ice and snow cover areas as well as the decline of June snow cover area and September sea ice area over 2002-2012.

Surface ice and snow cover variables derive from the National Snow and Ice Data Center (NSIDC) Equal-Area Scalable Earth grid (EASE) weekly product. A long-term record of sea ice concentration (SIC) dating back to 1978 is estimated using brightness temperature from the Nimbus-7 Scanning Multichannel Microwave Radiometer (SMMR), the Defense Meteorological Satellite Program (DMSP) -F8, -F11 and -F13 Special Sensor Microwave/Imagers (SSM/Is), and the DMSP-F17 Special Sensor Microwave Imager/Sounder (SSMIS). The EASE weekly product also summarizes snow cover over land. Snow cover fraction (SCF) is created when grid cells flagged as snow covered (defined as  $\geq 50\%$  snow cover of the original 25 km grid cell) are interpolated from the EASE grid to larger grid cells. In Chapter 3 we use SIC to calculate sea ice area (SIA) by multiplying the SIC in each grid box by its area and summing over the Arctic, defined as the area north of the Arctic circle (66.5).

### **2.2.1.1 Reanalyses**

Relationships between albedos, clouds and surface cover derived from the above observations are compared to five reanalyses: European Centre for Medium-Range Weather Forecasting (ECMWF) Interim (ERA-Interim), Modern Era Retrospective-Analysis for Research and Applications 2 (MERRA-2), National Center for Environmental Prediction/Department of Energy reanalysis 2 (NCEP R2), and the Arctic System Reanalysis versions 1 and 2 (ASRv1 and ASRv2). A summary of the specific reanalyses parameters used in this study is given in Tables 2.1 and 2.2.

Name	Original Resolution	Clouds
ASR v1, v2	30 km (v1), 15 km (v2)	PWRF single-moment 5-class microphysics scheme (v1), PWR 2-moment Morrison scheme (v2)
ERA-Interim	0.75° 0.75	Fully prognostic equations using 3-class two moment scheme
MERRA-2	1.25 1.25	Prognostic scheme and single-phase condensate with two species
NCEP R2	1.25 1.25	Diagnostic cloud scheme with parameterized relative humidity-cloud cover (empirical) relationship

TABLE 2.1: Summary of selected reanalyses characteristics.

Name	Sea Ice Concentration	Sea Ice Albedo	Snow Cover Fraction	Snow Albedo
ASR v1, v2	Prescribed from SSM/I and AMSRE	Annually varying seasonal cycle	Vary seasonally with assimilations from NESDIS observations	
ERA-Interim	Assimilated from various NCEP datasets	Monthly climatology	Calculated from snow water equivalent and snow density	Monthly climatology
MERRA-2	Prescribed from various ocean datasets	Seasonal cycle from SHEBA observations	NASA Catchment land surface model	MODIS climatology
NCEP R2	Prescribed from AMP-II		NSIDC snow cover fraction	Fixed with latitude dependent values

TABLE 2.2: Continued summary of selected reanalyses characteristics.

ERA-Interim is an ECMWF global reanalysis based on ERA-40 (Uppala et al., 2005) that uses a four-dimensional variable assimilation (4D var) (Dutra et al., 2010). Sea ice albedos in ERA-Interim are monthly values based on Ebert and Curry (1993) that are interpolated to the forecast time. Bare sea ice is assumed to represent the summer sea ice values, and the dry snow albedo is used for winter. Sea ice concentration is assimilated from NCEP real-time global (RTG) for January 2002—January 2009 and Operational Sea Surface Temperature (SST) and Sea Ice Analysis (OSTIA) for February 2009 to present. In ERA-Interim, snow cover fraction (SCF) is a function of snow water equivalent ( $SWE$ ) and snow density,

$\rho$ :

$$SCF = \min\left(1, \frac{\frac{SWE}{\rho}}{0.1}\right). \quad (2.1)$$

Only net clear-sky fluxes are available for ERA-Interim. To calculate the up-welling and down-welling clear-sky SW fluxes at the surface, surface albedo,  $\alpha_{SFC}$ , is calculated from the all-sky fluxes at the surface,

$$\alpha_{SFC} = \frac{SW^{\uparrow}}{SW^{\downarrow}}, \quad (2.2)$$

and is used to solve for the desired flux components. While this is the suggested method (Hogan, 2017), it is noted that the results are not precisely what is produced by the model because of differences in direct and diffuse shortwave radiation due to the absence of clouds. As with all reanalyses used here, ERA-Interim does not directly assimilate cloud observations. It uses prognostic equations for cloud liquid water and ice and cloud fraction from a three-class two moment scheme Gregory et al. (2000), Tiedtke (1993). Clouds are assumed to be maximum-random overlapped.

MERRA-2 is the continuation of MERRA (Rienecker et al., 2011), which includes enhancements to the meteorological assimilation, the Goddard Earth Observing System (GEOS) model, and the representation of ice sheets (Gelaro et al., 2017). In MERRA-2, the sea ice albedo varies seasonally based on flux tower observations from the Surface Heat Budget of

the Arctic Ocean (SHEBA) field campaign (Duynderke and de Roode, 2001). Monthly values are calculated from SHEBA and interpolated to instantaneous values. Sea ice concentration is prescribed from various ocean datasets (Bosilovich, 2015). Glaciated surfaces (e.g. Greenland) have dynamic energy and hydrologic properties that allow snow densification, meltwater runoff, percolation, and refreezing to be represented. The glacial model used includes updates to the NASA Catchment land surface model for snow cover, which has a prognostic surface albedo variable. MERRA-2 also includes a prognostic cloud scheme from Bacmeister et al. (2006) and assumes cloud are maximum-random overlapped.

NCEP R2 is an updated version of NCEP (Kalnay et al., 1996) correcting known errors, including sea ice and snow cover representation. These now follow the sea ice specifications of AMP-II (Kanamitsu et al., 2002). Snow cover is interpolated from the NSIDC weekly EASE-grid product to daily values, and the model is forced to match observations. For permanent snow, the albedo is set to 0.75 for latitudes above  $70^\circ$  and 0.6 for lower latitudes with a snow depth of at least 1 cm. NCEP R2 also updated several parametrizations of physical processes, including the radiative transfer model. However, NCEP R2 does not have clear-sky radiative fluxes available, which limits the analysis of radiative cloud effects. NCEP R2 uses a diagnostic cloud scheme with a parameterized relative humidity-cloud cover relationship and assumes random overlap.

Finally, ASR is a high-resolution regional reanalyses for the Arctic using an optimized version of the Polar Weather Research and Forecast (PWRF) model with ERA-Interim data

for initial and lateral boundary conditions (Bromwich et al., 2010, 2018). We compare versions 1 and 2 in this study. ASR employs the Noah Land Surface Model (LSM) with several improvements, including fractional sea ice within each grid cell and specified sea ice characteristics (e.g. thickness, snow cover over sea ice, albedo). Sea ice fractions are prescribed from daily NSIDC SSMI/I microwave radiometer measurements for the Polar WRF model. These prescribed values include first-order seasonal variations for the Arctic Ocean that depend on latitude and time of year. A seasonal cycle is used for the sea ice albedo which varies annually based on melt/freeze dates from satellite observations. Snow cover and snow albedo are assimilated from the National Environmental Satellite, Data, and Information Service (NESDIS) observations and vary seasonally, again, to represent melting and freezing. ASRv1 uses the PWRf single-moment five-class microphysics scheme, and ASRv2 uses the PWRf two-moment Morrison scheme. 2D total cloud fraction is not readily available in either version.

### **2.2.2 Surface Partitioning**

The goal of this work is to quantify the extent to which cloud cover modulates how the TOA albedo responds to changing sea ice and snow cover. This requires definitions of the Arctic and the areas covered by ice and snow. In this study, the Arctic is defined based on the mean 2-m air temperature from the Atmospheric Infrared Sounder (AIRS) on the Aqua satellite for 2002-2015. Grid cells in the NH with an annual mean temperature at or below 0 are considered part of the Arctic, as shown in Fig. 2.2a. Defining the Arctic with this method removes most of the warm waters from the Atlantic Ocean that remain ice free throughout

the year and behave differently than the majority of the Arctic (Morrison et al., 2018). There are various definitions of the Arctic, including area north of the Arctic circle (66.5), other latitudes at or above 60, the Arctic tree line, or the 10 July isotherm (Serreze and Barry, 2014, Smithson et al., 2013). Our definition of the Arctic bears resemblance to the latter two definitions. Using this Arctic definition, grid cells considered ocean (defined as having a land fraction less than 0.5) are further divided into three categories based on the SIC: all sea ice for  $SIC > 0.85$ , no sea ice for  $SIC \leq 0.15$ , and some sea ice for values between these limits. The same conditions are used to characterize land grid cells based on SCF. Note that no further delineation between different types of sea ice or snow covered surfaces is made here (e.g. snow covered ice or surface melt ponds). While the albedos of these surfaces can vary significantly, the objective of this study is to document the aggregate impacts of these surfaces on albedos. The mean annual cycle of these surface partitions over 2002-2012 are shown in Fig. 2.2b. Sea ice has the expected minimum in September and maximum in March with at least a small area of open water present throughout the year. Snow cover leads sea ice by one to two months, reaching a minimum in July and August. The area covered by some or all snow is fairly constant the rest of the year, and bare land is only present May-October. This partitioning will be used to isolate the contributions of ice- and snow-covered surfaces to the TOA albedo, determine the roles clouds play in modulating these effects, and assess how well reanalyses capture these relationships.

To set the stage for determining responses to surface cover variations, Fig. 2.3 decomposes the annual mean Arctic radiative energy budget from CERES observations into each surface type for the period 2002-2012. Both diagrams show marked differences in surface upwelling

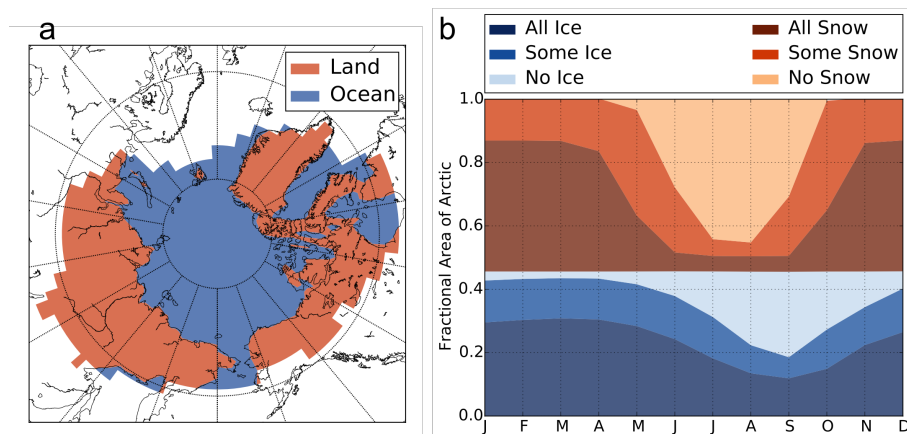


FIGURE 2.2: (a) Area in the Northern Hemisphere where 2002-2015 average 2-m air temperature from AIRS is less than or equal to 0. NCEP land fraction is used to define land ( $\leq 0.5$ ) and ocean ( $> 0.5$ ). This definition of the Arctic removes oceans north of the Atlantic that are continually ice free and behave differently than the rest of the Arctic. In this definition of the Arctic, 45% of area is ocean and 55% is land. (b) Fractional area of surface partitions averaged over 2002-2012 from NSIDC. All ice is defined as ocean grid cells with sea ice concentration (SIC)  $> 0.85$ , no ice refers to grid cells with  $\leq 0.15$  SIC, and all other grid cells are considered as having some ice. The same partitions are applied to land grid cells using snow cover fraction.

SW fluxes between surface types. In the all-sky energy budget (Fig. 2.3b), the difference in upwelling SW over open ocean and over ice covered ocean is  $40 \text{ Wm}^{-2}$ , and the difference between bare land and snow covered land is  $79 \text{ Wm}^{-2}$ . Similar differences are observed in clear skies (Fig. 2.3a) where the sea ice increases the upwelling SW relative to open water by  $44 \text{ Wm}^{-2}$  while snow cover increases upwelling SW by  $74 \text{ Wm}^{-2}$  relative to bare land. But the TOA energy budget tells a different story. Figure 2.3b suggests that the effects of surface cover on TOA fluxes are muted in the presence of clouds. The difference in outgoing SW between open water and ice-covered ocean is only  $5 \text{ Wm}^{-2}$ , in Fig. 2.3b as opposed to  $34 \text{ Wm}^{-2}$  in Fig. 2.3a. Likewise, the difference between bare and snow-covered land is reduced from  $72 \text{ Wm}^{-2}$  in clear-skies to  $35 \text{ Wm}^{-2}$  when cloudy skies are included. Clearly clouds play an important role in modulating SW radiation in the Arctic.

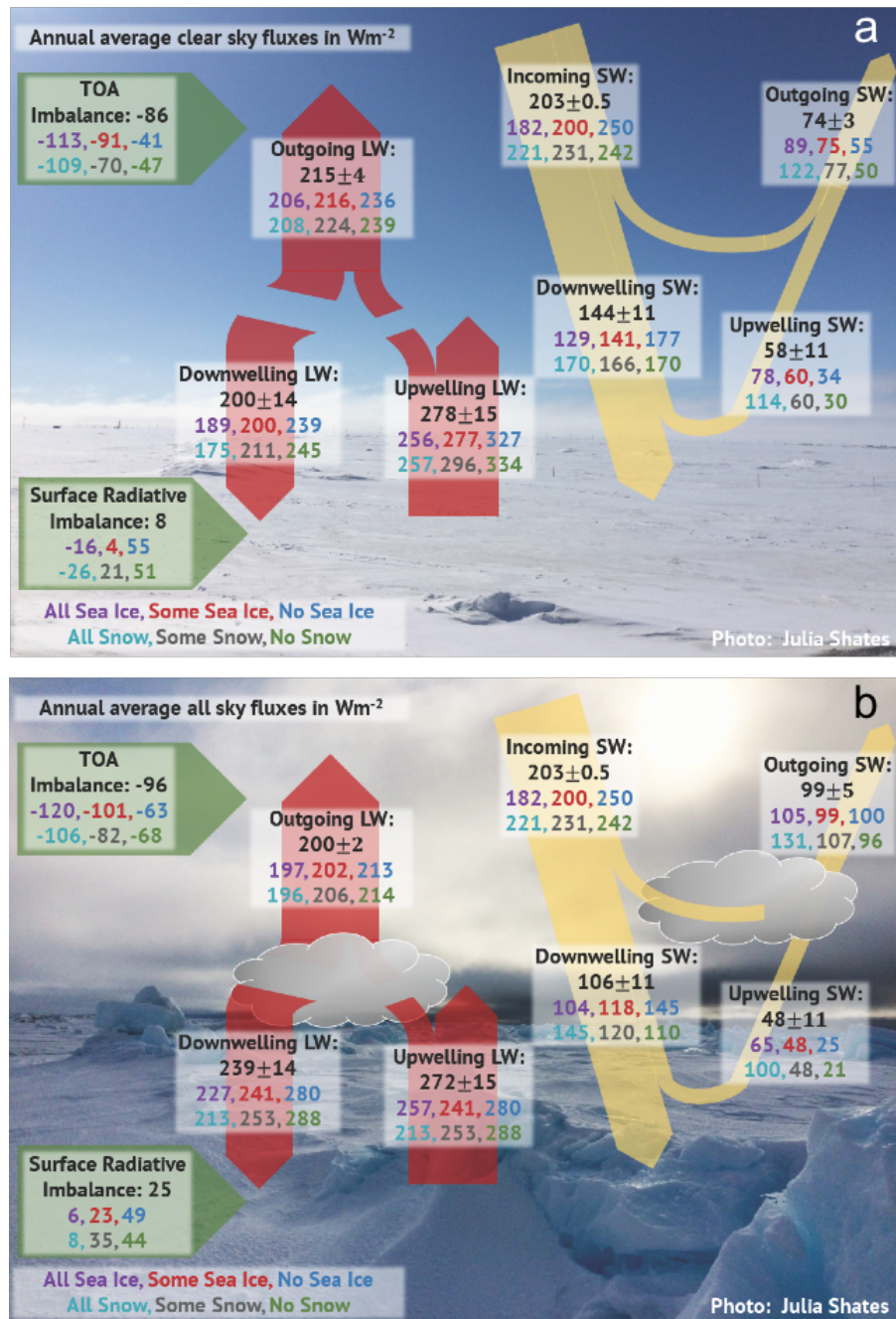


FIGURE 2.3: The Arctic radiative energy budget (CERES-EBAF) for (a) clear-sky and (b) all-sky conditions. Area averaged values over the domain presented in Fig. 2.2a from 2002-2012 are given in black. Fluxes are further partitioned by surface cover as follows: all sea ice (purple), some sea ice (red), no sea ice (blue), all snow (teal), some snow (gray), no snow (green).

### 2.2.3 Albedo Partitioning

To quantify the effects of clouds in modulating surface cover on TOA albedo, we partition the TOA albedo into surface and atmospheric components using the method of Donohoe and Battisti (2011). The reader is referred to that study for a detailed derivation. In this framework, each grid cell is considered as having a single atmospheric layer over an underlying reflective surface. The model accounts for three SW radiation processes: atmospheric absorption, atmospheric reflection, and surface reflection. All three processes are assumed isotropic. Surface and TOA albedos,  $\alpha$ , can each be calculated by applying

$$\alpha = \frac{SW^\uparrow}{SW^\downarrow}, \quad (2.3)$$

at the appropriate boundary, where  $SW^\uparrow$  and  $SW^\downarrow$  are upwelling and downwelling SW, respectively. The TOA albedo is then partitioned into two contributions, one from the atmosphere and one from the surface. The atmospheric contribution,  $\alpha_{TOA,ATM}$ , is equal to the direct reflectance,  $R$ , of SW radiation by the atmosphere,

$$\alpha_{TOA,ATM} = \frac{SW_{SFC}^\downarrow \times SW_{SFC}^\uparrow - SW_{TOA}^\downarrow \times SW_{TOA}^\uparrow}{(SW_{SFC}^\uparrow)^2 - (SW_{TOA}^\downarrow)^2} = R. \quad (2.4)$$

The surface contribution to the TOA albedo,  $\alpha_{TOA,SFC}$ , encompasses the amount of SW radiation that is reflected by the surface and passes through the atmosphere, eventually exiting at the TOA, including the effects of multiple reflections between the atmosphere and surface

$$\alpha_{TOA,SFC} = \alpha_{SFC} \frac{(1 - R - A)^2}{1 - R \times \alpha_{SFC}}, \quad (2.5)$$

where  $A$  is the atmospheric absorption

$$A = \frac{SW_{TOA}^{\downarrow} - SW_{TOA}^{\uparrow} - SW_{SFC}^{\downarrow} + SW_{SFC}^{\uparrow}}{SW_{SFC}^{\uparrow} + SW_{TOA}^{\downarrow}}. \quad (2.6)$$

Together, the atmospheric and surface contributions sum to the TOA albedo as calculated by Eq. 2.3. Partitioning the TOA albedo in this way allows the impacts of changing surface conditions and atmospheric constituents on the planetary albedo to be separated.

To further isolate the effects of clouds on this partitioning, we can take the difference between each contribution to the TOA albedo for all-sky and clear-sky conditions. Multiplying this difference by the solar insolation at the TOA converts it into flux units. Mathematically, the difference between all- and clear-sky TOA albedos multiplied by incoming SW is equivalent to the SW cloud radiative effect (CRE) (with the opposite sign):

$$\begin{aligned} (\alpha_{TOA,all} - \alpha_{TOA,clr}) \times SW_{TOA}^{\downarrow} &= \left( \frac{SW_{TOA}^{\uparrow,all}}{SW_{TOA}^{\downarrow}} - \frac{SW_{TOA}^{\uparrow,clr}}{SW_{TOA}^{\downarrow}} \right) \times SW_{TOA}^{\downarrow} \\ &= SW_{all}^{\uparrow} - SW_{clr}^{\uparrow} = -CRE_{SW,TOA}, \end{aligned} \quad (2.7)$$

remembering that  $\alpha_{TOA} = \alpha_{TOA,ATM} + \alpha_{TOA,SFC}$ . Thus, the partitioning of TOA albedo into its two contributions, in all- and clear-sky conditions, is directly related to SW CRE, but

the method also allows direct evaluation of the impact of surface conditions on TOA radiation. The difference in atmospheric contributions represents the amount of reflected SW radiation due to clouds at the TOA, and the difference in surface contributions represents the amount of SW flux that would have been reflected by the surface under clear-sky conditions (Stephens et al., 2015). We apply this framework to investigate the dependence of each of the aforementioned quantities on sea ice and snow cover.

## **2.3 How does planetary albedo respond to surface cover?**

### **2.3.1 Effects of surface cover on TOA albedo**

The surface and planetary albedos exhibit distinct annual cycles that depend on surface type. Mean monthly albedos over the Arctic domain for 2002-2012 calculated from CERES all-sky fluxes are shown in Fig. 2.4 for each surface condition. The Arctic-mean surface albedo reaches a peak of 0.68 in March when snow and sea ice cover are both at their maxima. Surface albedo decreases with snow/ice cover throughout the summer reaching a minimum of 0.23 in August, approximately one third of the spring maximum. Spatially, (Fig. 2.5) the exposed land and open ocean have much lower albedos once sea ice and snow melt. Evidence of surface melt is seen in the central Arctic ocean beginning in June where observed surface albedo decreases despite the high SIC. Land areas with high SCF through the summer, e.g. the Greenland ice sheet (GIS), maintain high surface albedos,  $>0.8$ , throughout the year due to their perpetually glaciated surfaces. They are the brightest surfaces from June to October.

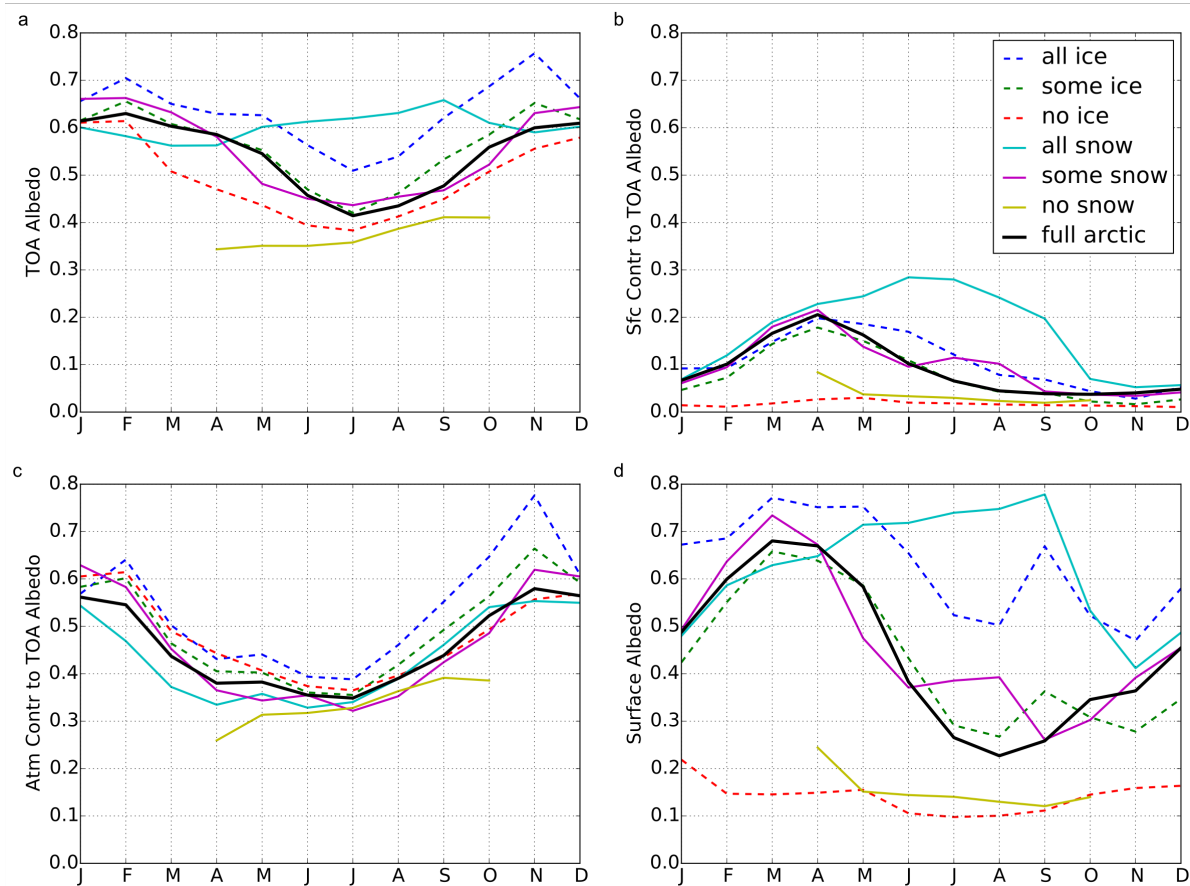


FIGURE 2.4: Annual cycles of (a) top of atmosphere (TOA) albedo, (b) surface albedo, (c) atmospheric contribution to TOA albedo, and (b) surface contribution to TOA albedo averaged over the Arctic (solid black) and surface partitions (colored lines) for 2002-2012 from CERES.

The TOA albedo has a markedly different annual cycle than that of the surface. In Fig. 2.4, the TOA albedo peaks in February and is at a minimum in July, leading the surface albedo by a month. Furthermore, the amplitude of the annual cycle is dramatically reduced: the February (0.63) and December (0.61) maxima are less than the maximum surface albedo, and only 50% larger than the July minimum (0.41), which is almost twice as large as the minimum surface albedo. The TOA albedo also varies less spatially across the Arctic than the surface albedo, seen in Fig. 2.5. While the enhanced reflection from the GIS and the

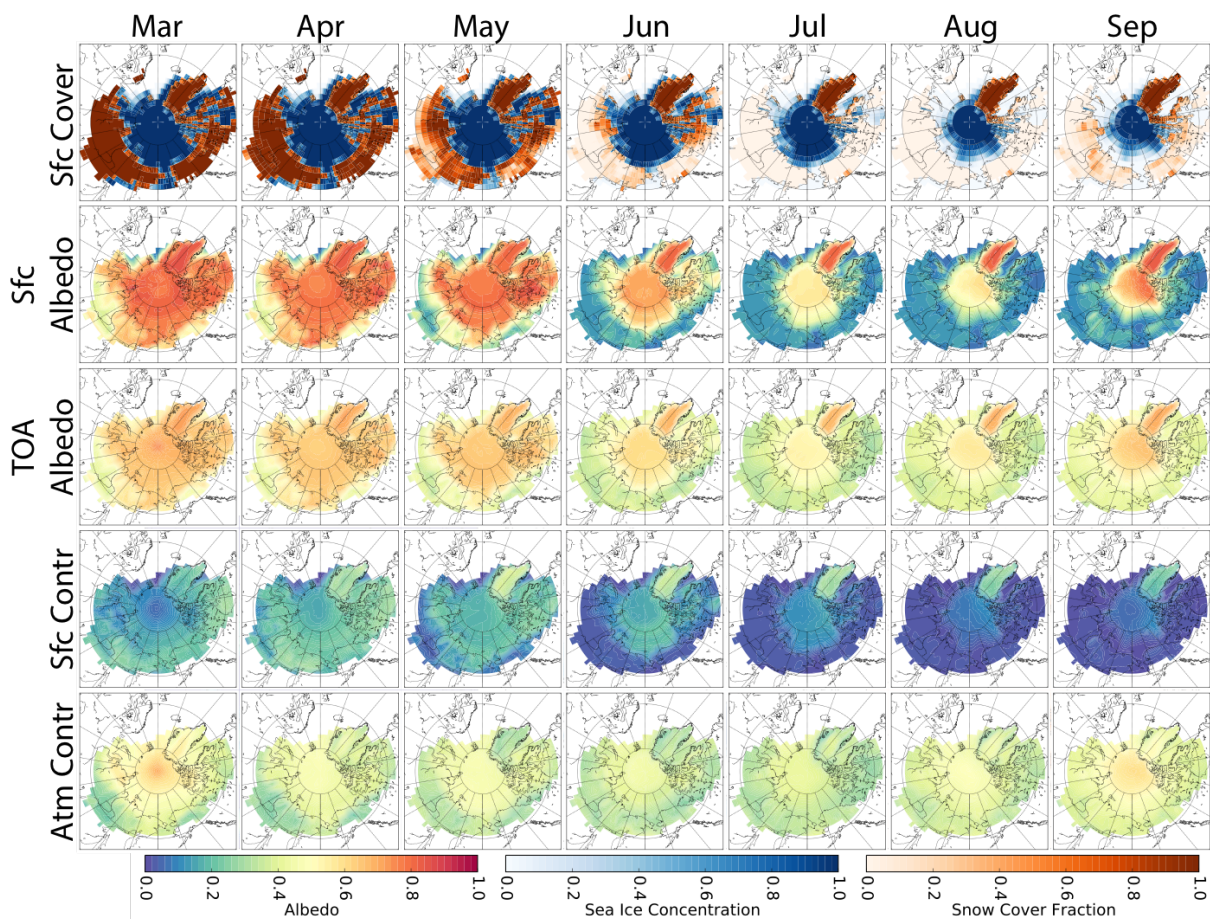


FIGURE 2.5: Average monthly maps of snow cover and sea ice fractions from NSIDC and albedos and TOA albedo contributions calculated from CERES all-sky fluxes. Months are averaged over 2002-2012. Only March through September are shown as they account for approximately 95% of annual solar insolation in the Arctic.

sea ice extent in the central Arctic ocean are visible at the TOA, these signals are less pronounced and the strong contrasts between open ocean and sea ice seen at the surface are muted at the TOA.

These findings are consistent with previous work that has shown that the TOA albedo is dominated by the atmospheric contribution (i.e. clouds) that masks the surface albedo (Donohoe and Battisti, 2011, Qu and Hall, 2005). Figure 2.4 demonstrates that, without exception, the atmospheric contribution to the TOA albedo is consistently larger than that

of the surface, even over the brightest surfaces (e.g. GIS) throughout the year. The atmospheric contribution therefore dominates the seasonal cycle of TOA albedo, rising to 0.58 in winter and falling to 0.35 in July, accounting for an average 84% of the TOA albedo. As with the TOA albedo, the atmospheric contribution is also much less varied spatially across the Arctic than the surface albedo (Fig. 2.5), although there is still contrast between land and ocean in early spring.

Although the surface contribution to the TOA albedo is proportional to the surface albedo, its average annual behavior is quite different. The spring peak has a maximum of 0.21 in April when surface ice and snow cover are high and cloud cover is relatively low (Curry et al., 1996, Sedlar, 2018), contributing 35% of the TOA albedo. By June the surface contribution decreases to 0.1, about 10% of the TOA albedo, when snow on land has largely receded, and remains low for the remainder of the year. These surface contributions are 2-3 times smaller than the actual surface albedo. As the surface albedo decreases, clouds play an increasingly dominant role in defining the TOA albedo since the surface reflects less SW radiation. The one exception to this trend is the GIS where the surface contribution increases to 0.28 in summer relative to spring and fall. This is likely a result of the fact that as wetter snow at mid-latitudes recedes, snow cover in the summer is dominated by the high-altitude, brighter snow on the GIS.

Figures 2.4 and 2.5 both clearly indicate that the large differences in surface albedo between the different surface partitions are muted at the TOA. The surface albedos for fully ice- and snow-covered surfaces are roughly 3-5 times greater than ice- and snow-less surfaces in all

months when these surfaces are present (as seen in Fig. 2.2b, on average, land without snow is only present April through September). Conversely, the TOA albedo over snow- and ice-covered surfaces are at most 1.7 times larger than their bare counterparts. The differences in surface albedo are being masked by clouds.

The contributions to TOA albedo also have notably different behaviors across the different surfaces. The surface contribution to the TOA albedo shows similar patterns to the surface albedo across surface types: uncovered ocean and land are low throughout the year; partially covered ocean and land follow the Arctic-wide average; and fully snow covered land is larger than all other surfaces through the summer. Although the surface contribution has small absolute differences relative to other albedos, the maximum difference between surface contributions is a factor of 13 greater between snow-covered land (0.27) and open ocean (0.02) in the summer. In contrast to the surface contribution, the atmospheric contribution behaves similarly for all surface types throughout the year. The maximum difference between atmospheric contributions is only a factor 1.33 between 0.3 (land with no snow) and 0.4 (ice-covered ocean) during the summer, a fractional difference ten times less than the surface contribution. This shows that the atmospheric contribution has reduced dependence on the underlying surface.

Comparing Figs. 2.4 and 2.5, the relative roles of the atmosphere and surface contributions to the TOA albedo variability can be summarized as follows: the annual cycle of Arctic-wide average TOA albedo is dominated by the annual cycle of the atmospheric contribution while the surface contribution is responsible for variations in the spatial pattern of TOA

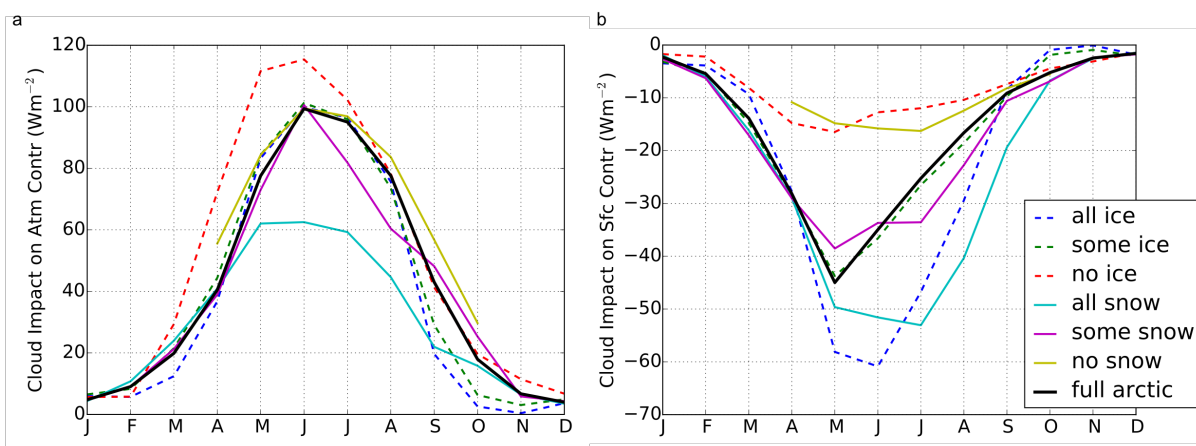


FIGURE 2.6: Cloud impacts on atmospheric and surface contributions to the TOA albedo are calculated using CERES all-sky and clear-sky fluxes. The clear-sky value is subtracted from the all-sky value and multiplied by the solar insolation at the TOA. These values correspond to SW radiation directly reflected by clouds (atmospheric contribution) (a) and the amount of SW that would have been reflected if clouds were not present (surface contribution) (b). Their annual cycles are plotted for Arctic-wide averages (solid black line) and various surface partitions (colored lines) for 2002-2012.

albedo between surface types. This is clear since the TOA albedo over most surfaces, with the exception of snow-covered land surfaces, exhibit similar annual cycles as the Arctic-mean (and the atmospheric contribution). Snow-covered land has a larger TOA albedo during summer when the Arctic overall sees a decrease; however, the peak at the TOA (0.61) is still damped compared to at the surface (0.78).

### 2.3.2 Cloud Modulation of Ice-Albedo Relationships

To cast these atmospheric effects into energetic units, the difference between all-sky and clear-sky contributions is multiplied by TOA solar insolation, giving the cloud impacts on surface and atmospheric contributions to TOA albedo. Recall that the difference between all- and clear-sky atmospheric contributions represents the amount of reflected SW radiation owing to clouds, and the difference for surface contributions shows the amount of SW

radiation that would have been reflected at the surface if clouds were not present. When summed together these cloud effect contributions have the same magnitude as the TOA SW CRE, which is opposite in sign to TOA LW CRE and larger April through September.

The atmospheric contribution cloud effect (Fig. 2.6c) follows the cycle of solar insolation with near zero reflection in winter and a June maximum of  $100 \text{ Wm}^{-2}$  for the Arctic-wide average. The different surface types follow the same pattern as the Arctic average, but surface cover clearly exerts a strong influence on the magnitude of reflected SW due to clouds. During months with significant solar insolation, clouds exert a much stronger influence over less reflective surfaces. For example, clouds reflect nearly twice as much SW radiation over open ocean in June ( $115 \text{ Wm}^{-2}$ ) than over land with all snow ( $62 \text{ Wm}^{-2}$ ). It is this compensating cloud effect that explains how the atmospheric contribution dominates the TOA albedo while itself having negligible dependence on surface cover.

This result is illustrated more directly by the surface contribution cloud effect in Fig. 2.6b. In general, clouds reduce the surface contribution to TOA albedo because they block radiation reflected at the surface from reaching the TOA, but this effect is much more pronounced over brighter surfaces that reflect more SW radiation in the absence of clouds. The overall magnitude of this *cloud masking* effect is 5-6 times larger over ice and snow covered surfaces than open water or bare land. Collectively these analyses quantify two important effects: the extent to which surface conditions modulate clouds effects on the planet's albedo and the masking influence of clouds on the effect of surface albedo changes on SW absorption.

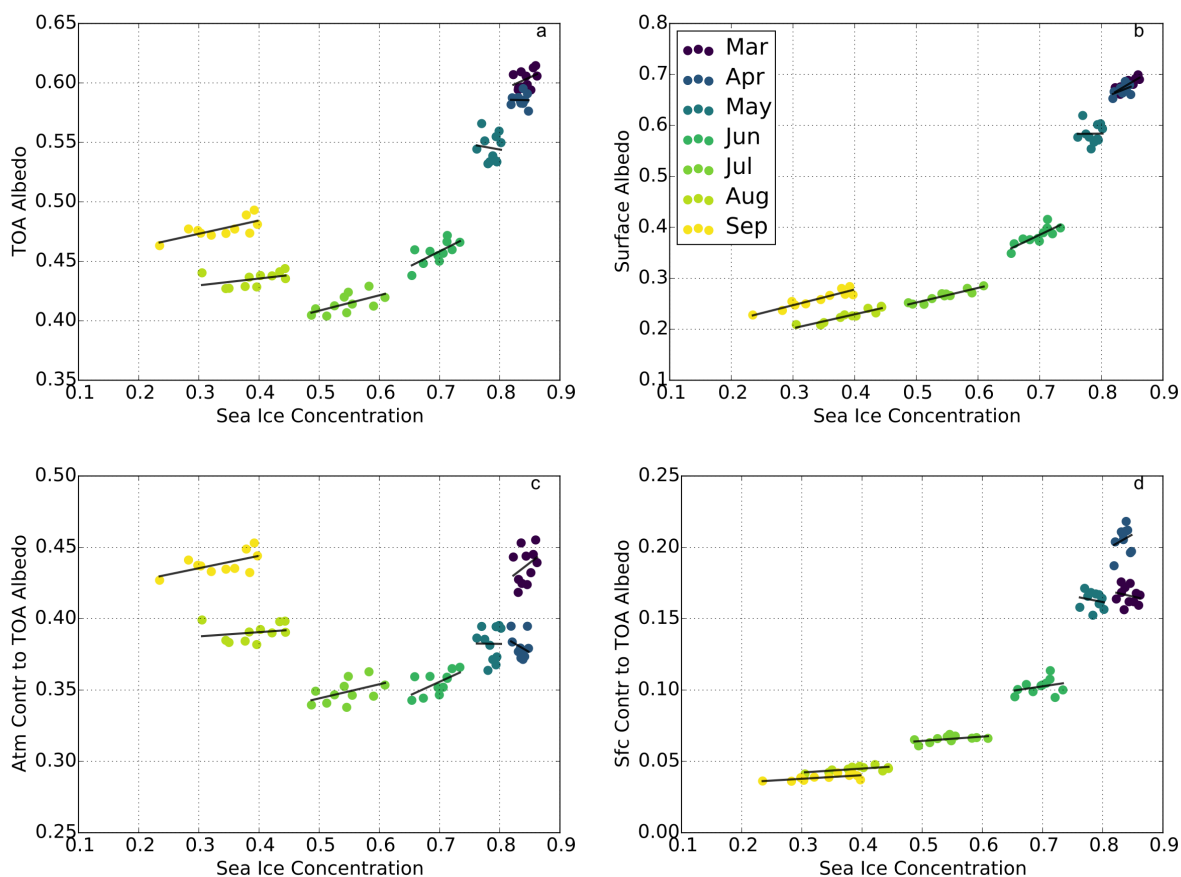


FIGURE 2.7: Arctic-wide averages of (a) top of atmosphere (TOA) albedo, (b) surface albedo, (b) atmospheric contribution to TOA albedo, and (c) surface contribution to TOA albedo plotted against the average sea ice concentration for individual months (March-September) during 2002-2012. Albedos and TOA albedo contributions are calculated from CERES all-sky fluxes. Lines of best fit are calculated using a linear least-squares regression, the slopes of which are given in Table 2.3.

While different surfaces have a strong influence on surface albedo, clouds significantly reduce the magnitude of these variations across the seasonal cycle. From a climate perspective, this leads us to ask: to what extent do clouds further modulate the ice-albedo feedback on longer timescales? While the length of the data record examined here is too short to examine trends, the large variations in SIC (Fig. 2.1) over the period examined allow the impacts of clouds on year-to-year surface cover variations to be quantified.

In pursuit of answering this question, we examine the response of monthly mean Arctic albedos and the TOA albedo contributions to average SIC and SCF for March through September in Figs. 2.7 and 2.8. In each month, the surface albedo and the surface contribution both exhibit strong positive relationships with SIC as expected (Fig. 2.7). Both surface albedo and TOA albedo decrease from March through July. From July to August the TOA albedo increases due to the increased atmospheric contribution during these months, as opposed to the surface albedo which is reduced further as sea ice approaches its September minimum. The atmospheric contribution has a parabolic shape that depends less on surface cover and more on clouds.

In addition to these larger patterns between albedos and SIC, there are also trends within individual months owing to inter-annual variations in SIC. Linear fits for each month reveal that the sensitivity of surface albedo to SIC is quite constant ( $\sim 0.3$ ) July through September (Table 2.3). TOA albedos and average SIC have less spread and no consistent trends in early spring (March-May). Beginning in June, surface albedo increases linearly with SIC. The surface contribution also increases with SIC but exhibits smaller trends due to the cloud masking effects described above. Further evidence of these effects are observed in the much weaker variation of monthly mean TOA albedo with SIC. The atmospheric contribution is fairly constant after July. This indicates that clouds are not particularly sensitive to changes in surface cover, consistent with the findings of Kay et al. (2016) who note that cloud feedbacks may be limited to fall in the Arctic.

The relationships between albedos and SCF, Fig. 2.8, are largely determined by the cycle

TABLE 2.3: Sensitivities of TOA and surface albedos and albedo contributions to variations sea ice concentration (SIC) for March through September. Slopes  $[\Delta \text{albedo}]/[\Delta \text{SIC}]$ , are found using linear least-squares regression in a given month, shown in Fig. 2.7.  $R^2$  values are given in parentheses. Statistically significant relationships ( $p < 0.05$ ) are bold.

Month	SFC Albedo	TOA Albedo	Atm Contr to TOA Albedo	Sfc Contr to TOA Albedo
Mar	<b>0.72 (0.68)</b>	0.23 (0.15)	0.32 (0.12)	-0.10 (0.04)
Apr	0.49 (0.23)	-0.01 (0.00)	-0.25 (0.08)	0.24 (0.06)
May	0.01 (0.00)	-0.09 (0.01)	-0.01 (0.00)	-0.08 (0.03)
Jun	<b>0.57 (0.67)</b>	<b>0.25 (0.48)</b>	<b>0.19 (0.38)</b>	0.06 (0.09)
Jul	<b>0.29 (0.88)</b>	<b>0.13 (0.39)</b>	0.10 (0.23)	0.03 (0.28)
Aug	<b>0.27 (0.88)</b>	0.06 (0.18)	0.03 (0.04)	<b>0.03 (0.41)</b>
Sep	<b>0.31 (0.88)</b>	<b>0.11 (0.52)</b>	0.09 (0.36)	<b>0.02 (0.52)</b>

of snow cover. The largest interannual variations in SCF occur in the melt season (May and June) and accumulation season (September). In May and June the surface albedo decreases as the snow melts, with sensitivities of 0.26 and 0.20, respectively (Table 2.4). To a lesser extent, variations in the timing of snow cover accumulation in September lead to a similar relationship between surface albedo and SCF (0.37) but over a smaller range of SCF. Surface albedos in early spring and late summer have no significant relationship with SCF because there is either widespread snow cover or widespread bare land, as seen in Fig. 2.5. The TOA albedo and its contributions follow this same pattern to varying degrees. TOA albedo has an overall linear relationship with SCF for March-September, but when focusing on individual months, May and June are again the months with statistically significant sensitivities, approximately half (0.14 and 0.10) those of the surface albedo. As with SIC, the surface contribution and surface albedo have similar patterns, but the surface contribution is roughly five to ten times smaller. The sensitivity of the atmospheric contribution is relatively large during May and June (0.12 and 0.07) but there is notable spread. While the TOA albedo is slightly more sensitive to SCF (0.16) than SIC (0.14) in May, by June SIC

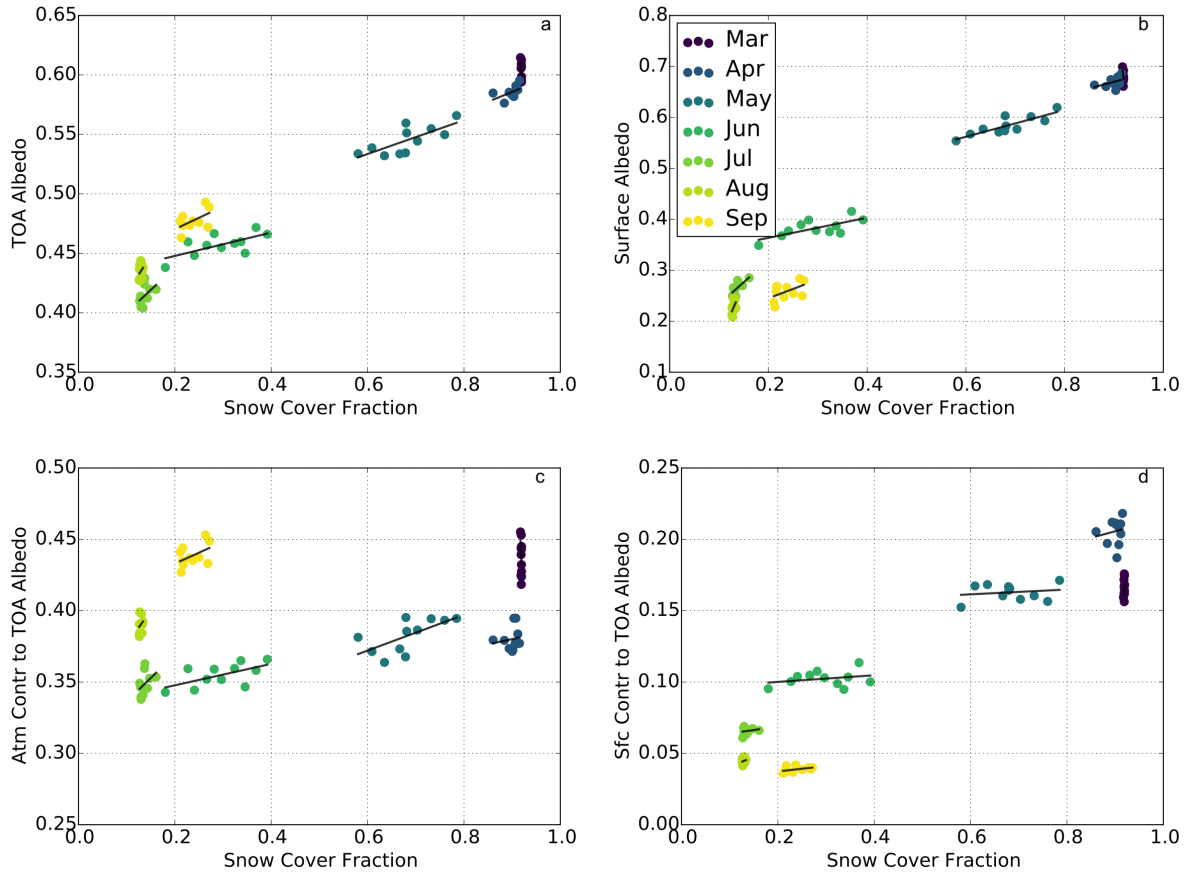


FIGURE 2.8: Same as Fig. 2.7 but with snow cover fraction.

TABLE 2.4: Same as Table 2.3 but using snow cover fraction instead of sea ice concentration.

Month	SFC Albedo	TOA Albedo	Atm Contr to TOA Albedo	Sfc Contr to TOA Albedo
Mar	-7.33 (0.18)	-4.72 (0.17)	-7.82 (0.17)	3.10 (0.10)
Apr	-0.26 (0.19)	0.16 (0.27)	0.07 (0.02)	0.09 (0.03)
May	<b>0.26 (0.72)</b>	<b>0.14 (0.55)</b>	<b>0.12 (0.43)</b>	0.02 (0.03)
Jun	<b>0.20 (0.51)</b>	<b>0.10 (0.45)</b>	<b>0.07 (0.37)</b>	0.02 (0.08)
Jul	<b>0.87 (0.55)</b>	0.38 (0.23)	0.33 (0.18)	0.05 (0.05)
Aug	2.24 (0.24)	0.62 (0.08)	0.48 (0.05)	0.14 (0.04)
Sep	0.37 (0.26)	0.19 (0.30)	0.15 (0.22)	0.04 (0.19)

(0.25) has a stronger influence than SCF (0.10) at the TOA.

### 2.3.3 Representation in Reanalyses

Clearly clouds exert a significant influence on how strongly the effects of surface cover change influence the Arctic radiation balance. Reanalyses are also frequently used to study climate variations in this region of few observations. Given their pervasiveness in studying the Arctic regional processes and driving models (Box et al., 2004, Zhang and Rothrock, 2003), it is imperative to assess how well reanalyses capture the observed modulating effects of clouds.

It is therefore important to ask how well reanalyses represent these cloud effects in the Arctic. The five reanalyses considered generally capture the shape of the annual albedo cycles but not necessarily their amplitudes. Given that a 0.05 difference in June albedo corresponds to  $25 \text{ Wm}^{-2}$  difference in summer, biases of this magnitude are sufficient to exert a significant influence on surface processes, as noted by Cao et al. (2016). Winter months account for less than 5% of incoming SW radiation and have large errors in observations (Fig. 2.9), so large biases during these months are less concerning than the rest of the year. In line with that fact, the largest differences in surface albedo occur in the winter, with over-estimations on the order of 0.10-0.20 but within the uncertainty of observations. The reanalyses perform better during the rest of the year, with surface albedo biases ranging from 0.01 (MERRA-2) to 0.1 (NCEP R2).

The spread in TOA albedo in the reanalyses is large in summer months owing primarily

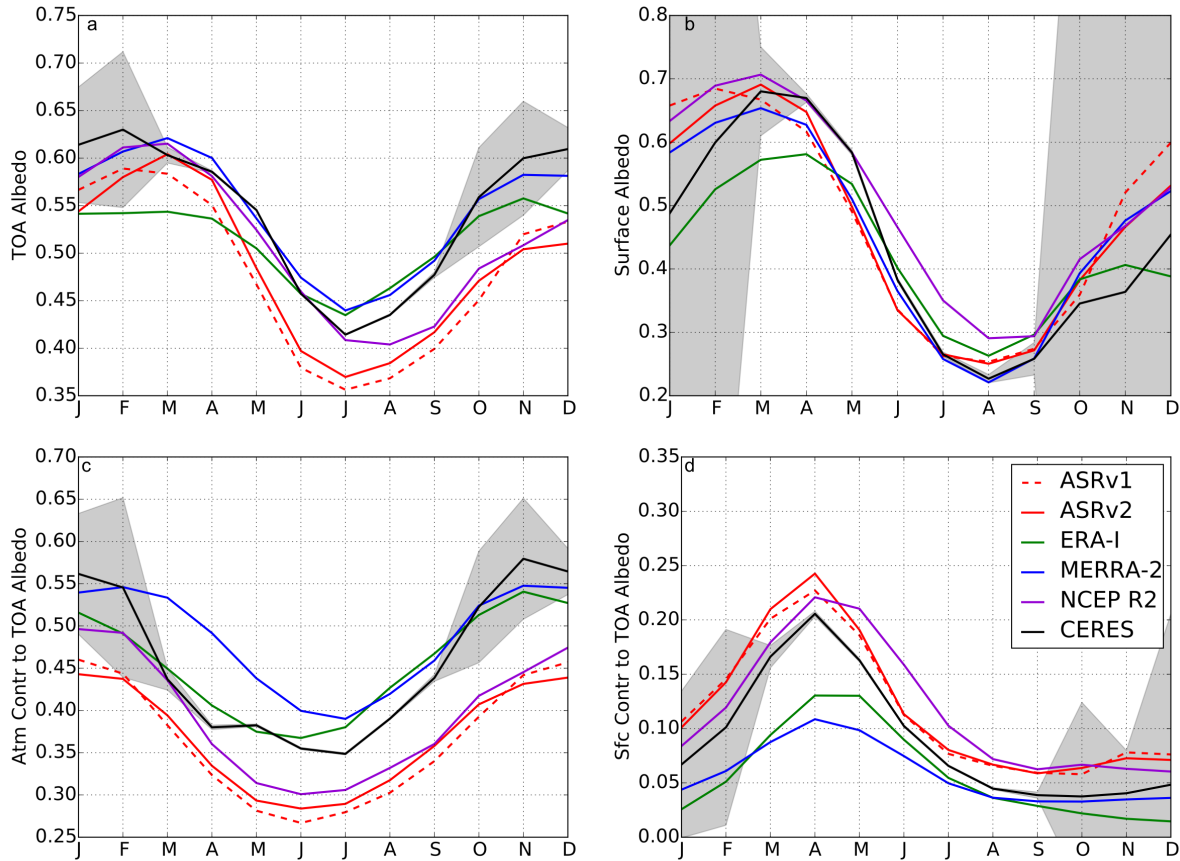


FIGURE 2.9: Average monthly albedos and TOA albedo contributions for CERES and re-analyses averaged over the Arctic for 2002-2012. Error in observational albedos and contributions (shown in grey) is propagated from uncertainties in CERES fluxes.

to the underestimation by ASR. ASRv2 moderately improves relative to ASRv1 but still underestimates TOA albedo by up to  $0.08$  ( $40 \text{ Wm}^{-2}$ ) in the summer peak. The performance of the other reanalyses vary more by season. For example, ERA-Interim predicts a smaller annual cycle in TOA albedo than CERES, as well as surface albedo, while the minimum in NCEP R2 lags observations by a month.

Figure 2.9 demonstrates that the discrepancies in TOA albedo largely result from differences in the atmospheric contribution. The annual cycles of biases between reanalyses and observations map closely onto those in TOA albedo. ASRv1, ASRv2, and NCEP R2

underestimate the atmospheric contribution to TOA albedo for all months, while MERRA-2 and ERA-Interim overestimate it for all but the winter months. This is not necessarily surprising since the atmospheric contribution is dominated by clouds, which is a common problem for reanalyses (Walsh et al., 2009).

Biases in the surface contribution to the TOA albedo are significant in spring when the spread in reanalyses approaches a factor of four. Both ASR versions and NCEP R2 represent the spring maximum in surface contribution relatively well, overestimating it by 0.05 or less. ERA-Interim and MERRA-2, on the other hand, underestimate the surface contribution to TOA albedo throughout the year with biases on the order of 0.1 (50%) during the spring maximum. This difference is enough to completely offset a positive bias in the atmospheric contribution in MERRA-2, artificially leading to a good agreement with observed TOA albedo that masks substantial biases in the partitioning of energy between the atmosphere and surface. In ERA-Interim, the large bias in springtime surface reflection leads to a substantial over-estimation of SW absorption in the spring (March-May).

Figure 2.10 presents albedos and contributions averaged over March-September for each surface condition. With the exception of NCEP R2, which overestimates the albedo of all ocean surfaces, the reanalyses capture surface albedos for the surface partitions. Potentially more serious, however, are the biases in ERA-Interim over land with and without snow. ERA-Interim predicts an average surface albedo over land without snow (0.31) that is over twice that seen in observations (0.14). ERA-Interim also underestimates the surface albedo of snow-covered land (0.62 versus 0.71 in observations), which leads to a much

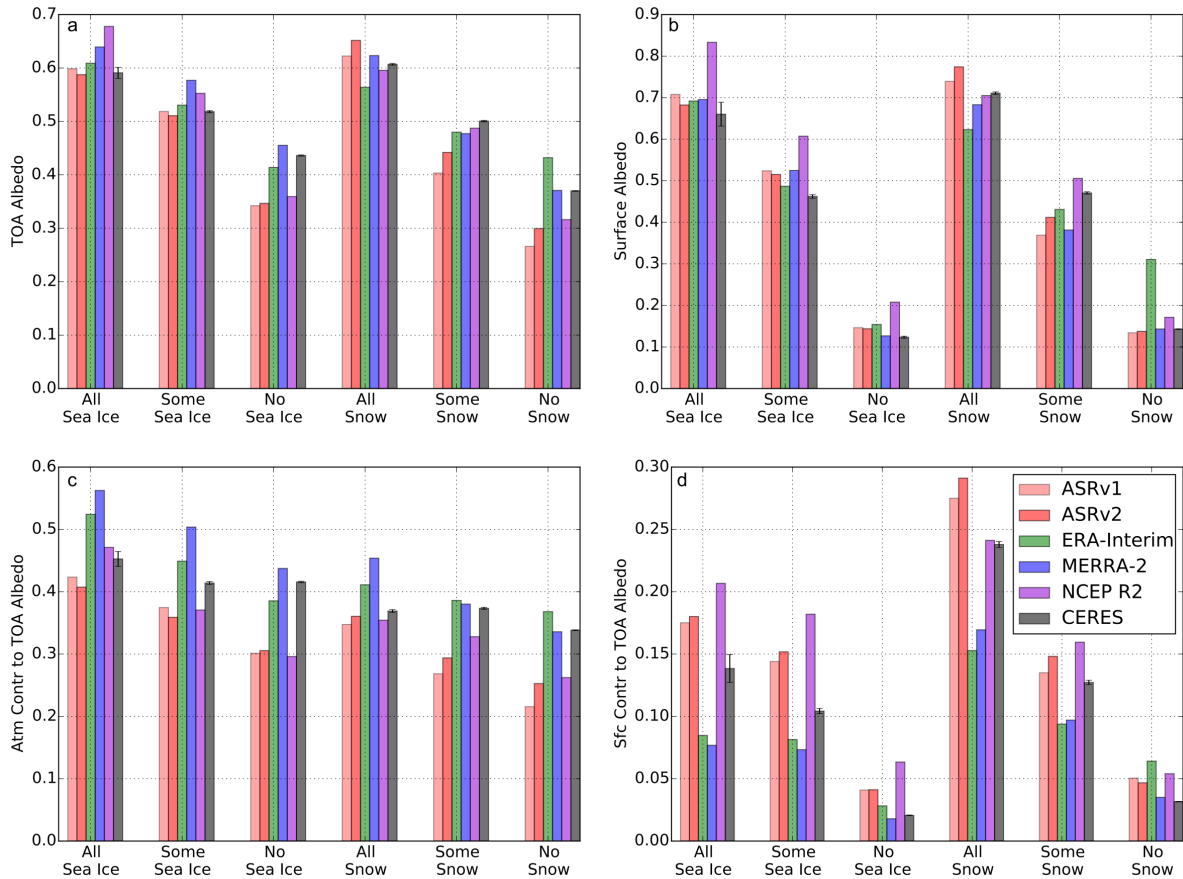


FIGURE 2.10: Comparison of albedos and TOA albedo contributions between CERES and reanalyses partitioned by surface cover. Albedos and TOA albedo contributions are averaged over March-September, as these are the months that account for 95% of solar insolation in the Arctic. Error for observational albedo is propagated using CERES flux uncertainties.

lower contrast between land with and without snow (0.31) compared with observations (0.57). This suggests that the effects of snow cover changes may be significantly underestimated in ERA-Interim. In general the other reanalyses represent variations in TOA albedo with surface conditions fairly well. The contributions to TOA albedo, however, are more widely spread relative to observations and each other. Both versions of ASR and NCEP R2 have positively biased surface contributions and negatively biased atmospheric

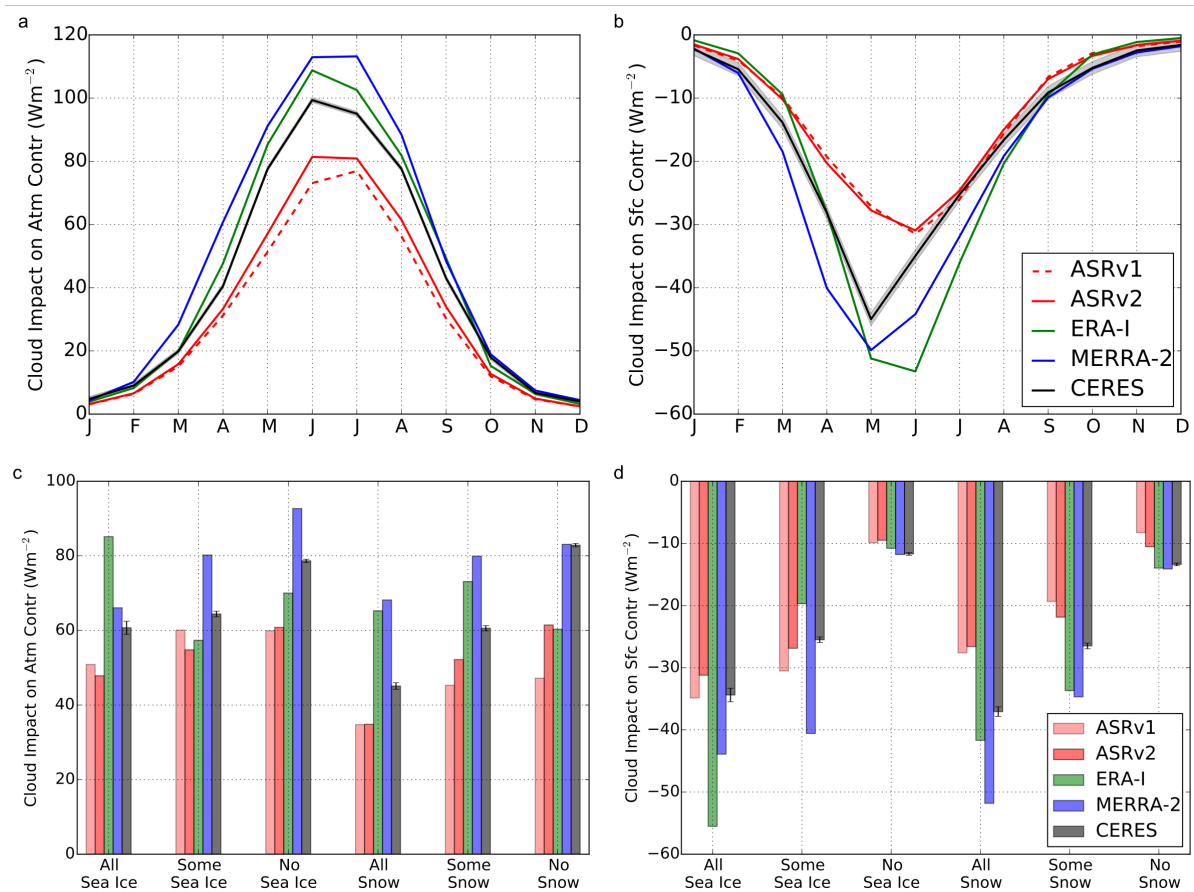


FIGURE 2.11: Cloud impacts on atmospheric and surface contributions to TOA albedo. These values correspond to the amount of reflected SW due to clouds and the amount of SW that would have been reflected if clouds were not present. Top: annual cycles averaged over the Arctic for 2002-2012. Bottom: albedos and TOA albedo contributions are averaged over March-September from 2002-2012 for different surface partitions.

contributions ( $\leq 0.1$ ), compared to observations, that tend to cancel in the TOA albedo. Inversely, ERA-Interim and MERRA-2 have positive biases in atmospheric contributions that are compensated by negative biases in their surface contributions across most surface types. Thus the apparent agreement in Fig. 2.10a derives from a fortuitous cancellation of atmospheric and surface biases that have significant implications for how energy is partitioned between the atmosphere and surface in the reanalyses.

The observations suggest that clouds play an important role in moderating sea ice/snow cover albedo effects. In order to accurately predict surface warming and melt rates associated with climate responses, reanalyses must also capture these relationships between albedos and clouds. The biases in Figs. 2.11c and d can be traced to errors in these relationships. While the three reanalyses with available clear-sky fluxes capture the annual cycle of cloud TOA albedo contributions in Figs. 2.11a and 2.11b, they all vary in magnitude for the summer maximum, with a range of  $\pm 20 \text{ Wm}^{-2}$  for the atmospheric contribution and  $\pm 15 \text{ Wm}^{-2}$  for the surface contribution. The maxima and minima often lag observations by a month as well. This bias is also reflected at the TOA but is partially compensated by an enhanced atmospheric contribution.

When partitioned by surface type (Figs. 2.11c and 2.11d), the three reanalyses exhibit mixed behaviors. MERRA-2 and both versions of ASR capture the cloud effects on atmospheric and surface TOA albedo contributions. ERA-Interim shows the opposite trend - the atmospheric contribution cloud effect is larger over sea ice than open water and there is no clear dependency of it on snow cover. All three reanalyses show that the surface contribution cloud effect increases with surface brightness, although ERA-Interim overestimates the change between high and low albedo surfaces by nearly a factor of two over oceans ( $45 \text{ Wm}^{-2}$  versus  $23 \text{ Wm}^{-2}$  from CERES).

Some of the biases in reanalyses albedos can be attributed to their representations of clouds. Average cloud fraction over the Arctic up to 82 is compared between CloudSat/CALIPSO

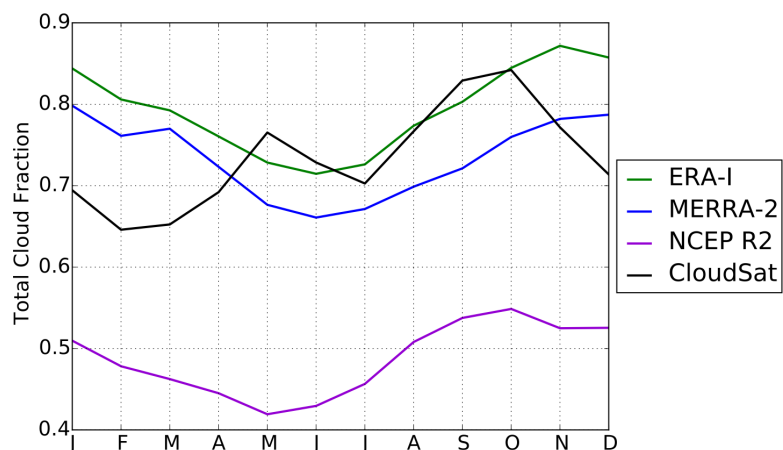


FIGURE 2.12: Total cloud fraction averaged over the Arctic up to 82 for 2007-2010.

and reanalyses, Fig. 2.12. ERA-Interim matches observations fairly well May through October and overestimates the amount of clouds November through April. MERRA-2 is also near observations in summer and fall, although it underestimates cloud fraction during March-October and again overestimates cloud amount in winter. NCEP R2 underestimates cloud fraction for the entire year by 0.2-0.3. While none of these reanalyses directly assimilate cloud observations, the prognostic schemes used by ERA-Interim and MERRA-2 seem to perform better than the diagnostic cloud scheme from NCEP R2. The reader is directed to Liu and Key (2016), Wesslén et al. (2014), and Chernokulsky and Mokhov (2012) for more detailed investigation of cloud representation in reanalyses.

The reanalyses capture broad relationships between surface cover and albedos but struggle to accurately represent the relative magnitudes between different surfaces and TOA albedo contributions. To test the implications of these differences on the representation of interannual variability in the Arctic, the sensitivities of albedos and contributions to SIC in reanalyses and observations for June and September are presented in Fig. 2.13 and Table

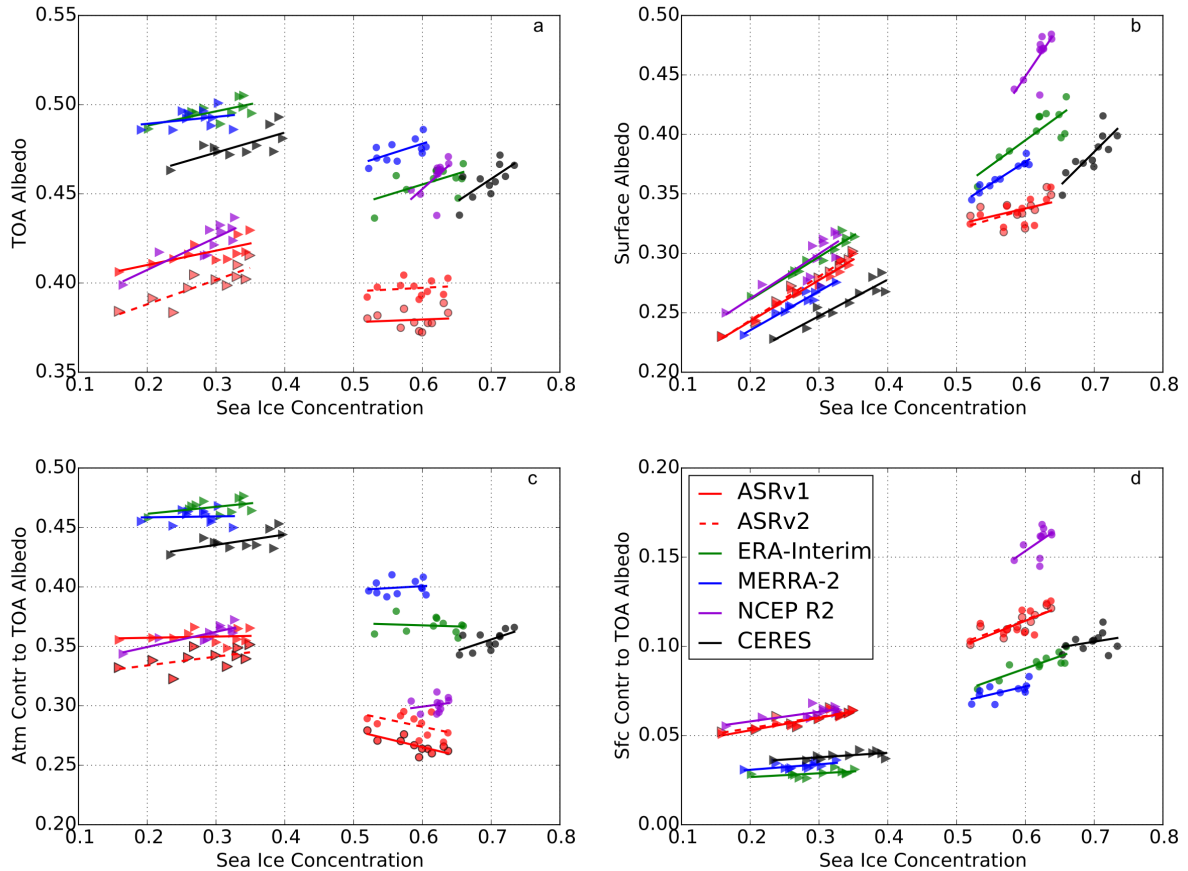


FIGURE 2.13: Sensitivity of (a) TOA albedo, (b) surface albedo, (c) atmospheric contribution, and (d) surface contribution to sea ice concentration in reanalyses and observations for two months: June (circles) and September (triangles).

2.5. Surface albedo and surface contribution sensitivities to SIC are well represented by all five reanalyses in September and marginally less so in June. All reanalyses show that surface albedo is sensitive to SIC in June but have a range of 0.13 (ASR) to 0.85 (NCEP R2) with observations falling in the middle (0.57). Larger biases are present in the TOA albedo sensitivity to SIC. ASRv1 and ASRv2 show essentially no influence of SIC on the TOA albedo in June, contrary to observations. NCEP R2 tends to over estimate the influence of SIC on the TOA albedo. Reanalyses predict sensitivities closer to observations in September, although the MERRA-2 predicts no significant influence of SIC and NCEP R2 again overestimates

TABLE 2.5: Sensitivity of albedos and TOA albedo contributions to SIC for observations and reanalyses in dimensionless units  $[\Delta \text{ albedo}]/[\Delta \text{ SIC}]$ .  $R^2$  values are given in parentheses. Statistically significant relationships ( $p < 0.05$ ) are bold.

		CERES	ASR	ASRv2	ERA-Int	MERRA-2	NCEP R2
SFC Albedo	Jun	<b>0.57 (0.67)</b>	0.13 (0.20)	0.17 (0.32)	<b>0.42 (0.71)</b>	<b>0.37 (0.93)</b>	<b>0.85 (0.57)</b>
	Sep	<b>0.31 (0.88)</b>	<b>0.37 (0.98)</b>	<b>0.35 (0.97)</b>	<b>0.36 (0.94)</b>	<b>0.33 (0.94)</b>	<b>0.38 (0.77)</b>
TOA Albedo	Jun	<b>0.25 (0.47)</b>	0.01 (0.01)	0.02 (0.03)	0.12 (0.33)	<b>0.12 (0.40)</b>	0.34 (0.39)
	Sep	<b>0.11 (0.52)</b>	<b>0.14 (0.71)</b>	<b>0.08 (0.51)</b>	<b>0.08 (0.43)</b>	0.04 (0.08)	<b>0.18 (0.72)</b>
Atm Contr to TOA Albedo	Jun	<b>0.19 (0.38)</b>	<b>-0.14 (0.57)</b>	-0.12 (0.23)	-0.02 (0.01)	0.03 (0.03)	0.08 (0.04)
	Sep	0.09 (0.36)	0.07 (0.28)	0.01 (0.01)	0.06 (0.22)	0.01 (0.00)	<b>0.13 (0.70)</b>
Sfc Contr to TOA Albedo	Jun	0.06 (0.09)	<b>0.15 (0.70)</b>	<b>0.12 (0.44)</b>	<b>0.14 (0.76)</b>	<b>0.09 (0.40)</b>	0.26 (0.30)
	Sep	<b>0.02 (0.43)</b>	<b>0.06 (0.72)</b>	<b>0.07 (0.87)</b>	0.02 (0.28)	<b>0.03 (0.39)</b>	<b>0.05 (0.57)</b>

the influence.

The differences between observations and reanalyses at the TOA can be found in the surface and atmospheric contributions. In June, all of the reanalyses overestimate the influence of SIC on the surface contribution. They either underestimate its influence on the atmospheric contribution (MERRA-2, NCEP R2) or predict the opposite relationship (ASRv1, ASRv2, ERA-Interim). These competing biases result in greatly reduced TOA albedo sensitivity to sea ice, with the exception of NCEP R2 that has a much larger surface contribution compared to observations. Most reanalyses are better aligned with observations in September when their biases in SIC influence on TOA albedo contributions are smaller.

## 2.4 Discussion and Conclusions

While Arctic amplification is an important component of climate change, the mechanics are not fully understood, particularly the effects of clouds. In this paper we have quantified how clouds modulate albedos in the Arctic. The surface albedo changes with snow and sea

ice cover through the seasons, but the TOA albedo varies only half as much. Reanalyses do not capture this relationship, generally predicting that SIC has less influence on the TOA albedo than seen in observations. In satellite observations, the atmosphere contributes 2-3 times more to the TOA albedo than the surface throughout the year. Clouds are the main contributor to the atmospheric contribution, increasing the atmospheric reflectivity and blocking SW reflected from the surface from leaving the Earth system. The atmospheric contribution to TOA albedo also depends less on the underlying surface, meaning that changes to the surface cover may have less impact on it. Despite differences in methods, our sensitivities are similar to the radiative effectiveness reported by Gorodetskaya et al. (2006).

The reduced sensitivity of TOA albedo to surface cover is important for the ice-albedo feedback. Our work supports previous studies that have found reduced ice-albedo feedback parameters due to clouds (Hwang et al., 2018, Soden et al., 2008). We have found that clouds mask the surface albedo and damp changes in surface cover at the TOA. When the surface albedo is sensitive to SIC changes in the summer and fall, the surface contribution to the TOA albedo is low, leading to reduced changes at the TOA. There is nuance, though. Clouds do not simply replace underlying snow and ice. While clouds have higher albedos than open ocean, there is still a measurable difference ( $\sim 0.15$ ) in TOA albedo between land with and without snow cover and ocean with and without sea ice cover. Clouds may reduce the ice-albedo feedback, but the radiative effects of clouds at the TOA are unlikely to be large enough to prevent the ice-albedo feedback from continuing and contributing to Arctic amplification.

Since the interaction between clouds and albedos is essential to understanding and modeling the evolution of the Arctic, it is important that datasets used to study the Arctic, i.e. reanalyses, accurately portray these relationships. These results demonstrate that reanalyses cannot always be taken as proxies for observational datasets, especially in regions where limited observations are assimilated and for variables that cannot be directly measured. In such instances, models rely heavily on underlying parameterized physics rely upon parameterizations that are frequently based on lower latitudes where more abundant observations are available. To that end, the observational benchmarks provided here are also used to evaluate modern reanalyses. While no single reanalysis perfectly represents these variables for all months, most trends seen in observations are captured to some extent. The timing of annual maximum and minimum albedos and TOA albedo contributions are fairly accurate in reanalyses, but their magnitudes vary considerably. Reanalyses show that surface and TOA albedos and the surface contribution to TOA albedo all increase with higher snow and ice surface cover, to varying degrees. The reanalyses also show that the atmospheric contribution to TOA albedo varies with SIC and SCF, but this is not seen in the observations. While averaged surface and TOA albedos have relatively low biases compared to observations, the partitioning of TOA albedo contributions and surface cover vary far more. The consequences of this are highlighted in the differing sensitivities of reanalyses to SIC where reanalyses show a spread of changes in response to SIC. These discrepancies are important as reanalyses are frequently used to study the rapidly evolving Arctic and drive other models, and differences between reanalyses will affect the outcome depending on the chosen reanalysis (e.g., Lindsay et al. (2014)).

Many of the biases found in partitioning reanalyses are related to their representations of clouds. MERRA-2 and ERA-Interim overestimate the atmospheric contribution during summer and underestimate the surface contribution for the entire year. This is likely due to clouds that are too bright given the reasonable cloud fractions during summer. Overestimating the cloud effect on the TOA albedo surface contribution leads to higher TOA albedos which means too little SW absorption. This in turn reduces melt rates at the surface. NCEP R2 has too few clouds from their diagnostic scheme leading to overestimated surface contributions and underestimated atmospheric contributions for much of the year. ASRv1, and ASRv2 likely suffer from too few clouds as well. It has been noted that the microphysics used in ASRv1 is known to under-represent liquid water in polar clouds Hines and Bromwich (2017). Although the cloud microphysics was updated in ASRv2, it does not seem to have a large impact. ASRv1 also has large radiative biases at the surface, particularly SW fluxes in excess of  $40 \text{ Wm}^{-2}$  at high latitudes. While ASRv2 improved these biases, they still deviate from observations by approximately  $20\text{-}30 \text{ Wm}^{-2}$ . The trade-off with a more complex microphysics scheme is that there are more inputs that must be finely tuned, meaning there are more chances to be wrong. Reanalyses with simpler cloud schemes, e.g. ERA-Interim, have more realistic outputs, but their results may be due to better tuning and assimilation rather than accurate representation of the physics.

This work has shown the behavior of surface and TOA albedos with changing surface cover in the Arctic. Because the atmosphere contributes more to the TOA albedo than the surface, we have found that clouds have a damping effect on the TOA albedo. While we have

touched on the sensitivity of albedos and TOA albedo contributions to SIC and SCF, more work should be done to quantify these relationships.

## Chapter 3

# The influence of clouds on absorbed solar radiation trends and detectability in observations and CMIP6

©Copyright 2021 AMS\*

### 3.1 Preface

In the previous chapter we quantified the contribution of clouds to the planetary albedo and found that clouds dampen changes in surface albedo due to sea ice and snow cover when viewed from space. Now we turn to the effect of clouds on SW absorption into the Arctic

---

\*Sections 3.1-3.3 in this chapter are lightly modified from: Sledd, Anne, and Tristan L'Ecuyer. "Uncertainty in Forced and Natural Arctic Solar Absorption Variations in CMIP6 Models." *Journal of Climate* 34.3 (2021): 931-948. Section 3.4 is being prepared as a manuscript for submission with coauthor T. S. L'Ecuyer.

climate system. The first piece in this chapter utilizes the growing record of satellite-based Earth radiation budget observations and a statistical framework for assessing the time to emergence (TTE) of forced climate trends in the Arctic. We combine these tools to establish whether the recent observational record is long enough to distinguish forced changes in absorbed SW radiation in the Arctic from interannual variability with statistical confidence and to understand how clouds impact our ability to discern such trends. We further examine the character of Arctic absorbed SW radiation trends in modern climate models. Specifically, we address the following questions: 1) how do clouds impact trends in absorbed SW radiation and their TTE? 2) how do predicted SW trends in GCMs compare to observations? and 3) what aspects of modeled Arctic climate variability drive differences in TTE relative to observations? We estimate the TTE of absorbed SW radiation trends from satellite observations and GCMs from phase six of the Coupled Model Intercomparison Project (CMIP6) over the 21st century. A mathematical understanding of the factors that influence SW trend detection is presented and then related to the physical changes occurring in today's Arctic.

The second piece of this chapter focuses exclusively on satellite observations from the last two decades. This recent time period coincides with a drastic reduction of perennial sea ice and emergence of a fundamentally different Arctic climate, the "New Arctic". In the second section we calculate spatial SW absorption trends spatially over the Arctic and quantify regional differences for land, ocean, and individual regions as seen from space. We explicitly determine the impact of clouds over these partitions by comparing absorbed SW radiation trends from all-sky and clear-sky fluxes. By analyzing the significance of these trends and

their variability, we quantify the expected record length needed to observe statistically significant trends and how those values are impacted by clouds. Taken together we use this work to highlight how dramatic changes in the "New Arctic" are.

## **3.2 Data**

### **3.2.1 Observations**

Both observational datasets used in this study are extracted from the Arctic Observations and Reanalysis Integrated System (ArORIS), a collection of datasets created to support Arctic climate research (Christensen et al., 2016). All datasets in ArORIS are re-gridded to a uniform 2.52.5rid and averaged to monthly timescales.

We use radiative fluxes from the the Clouds and Earth's Radiant Energy System Energy Balance and Filled (CERES-EBAF) edition 4.1 on board the Terra and Aqua NASA satellites. TOA fluxes in the CERES-EBAF dataset are adjusted within their ranges of uncertainty to be consistent with the global heating rate from in situ ocean observations (Kato et al., 2018, Loeb et al., 2018). We use all-sky fluxes at the TOA and total-region clear-sky fluxes at the surface. Previously, clear-sky fluxes from CERES only represented fluxes in areas that were free of clouds at the time of observation. Total-region clear-sky fluxes are intended to facilitate direct comparisons with models that typically determine clear-sky fluxes over a grid box by ignoring clouds in the atmospheric column in the radiative transfer calculation. To that end, CERES total-region clear-sky fluxes include an adjustment factor given by the difference of calculating clear-sky fluxes for cloud-free regions and calculating them with

a radiative transfer model while ignoring clouds in the atmospheric column (Loeb et al., 2020). Uncertainty for net SW flux at the TOA under all-sky conditions is  $2.5 \text{ Wm}^{-2}$  (Loeb et al., 2018). At the surface under clear-sky conditions in the Arctic, uncertainty in SW fluxes are 14 and  $16 \text{ Wm}^{-2}$  for downwelling and upwelling radiation, respectively (Kato et al., 2018).

Sea ice concentrations (SIC) and extent are derived from the National Snow and Ice Data Center (NSIDC) Equal-Area Scalable Earth grid (EASE) weekly product (Brodzik and Armstrong, 2013). Their long-term record of SIC dating back to 1978 is estimated using brightness temperature from the Nimbus-7 Scanning Multichannel Microwave Radiometer (SMMR), the Defense Meteorological Satellite Program (DMSP) -F8, -F11 and -F13 Special Sensor Microwave/Imagers (SSM/Is), and the DMSP-F17 Special Sensor Microwave Imager/Sounder (SSMIS). We use SIC to calculate sea ice area (SIA) by multiplying the SIC in each grid box by its area and summing over the Arctic, defined as the area north of the Arctic circle (66.5).

Figure 3.1 shows deseasonalized anomalies of monthly Northern Hemisphere sea ice extent, surface albedo and planetary albedo calculated using clear-sky and all-sky SW fluxes, respectively, from the CERES over the area above of 60 from 2001 to 2017. even over this relatively short time period there are significant negative trends in sea ice extent and surface albedo anomalies. The time series of surface albedo anomalies closely follows that of sea ice extent, as is expected given the high albedo of sea ice and its marked transition to low albedo ocean. On the other hand, anomalies in the planetary albedo derived from TOA fluxes are, to some degree, decoupled from sea ice extent. For example, September

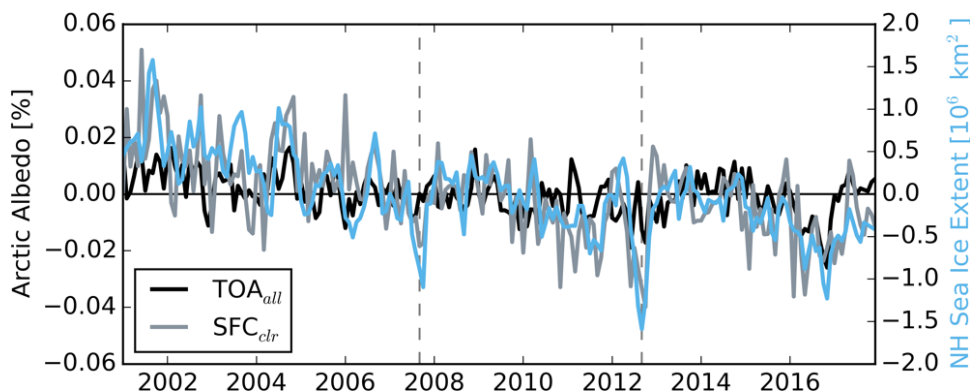


FIGURE 3.1: Monthly deseasonalized anomalies for Arctic surface (SFC) and top of atmosphere (TOA) albedos and Northern Hemisphere (NH) sea ice extent (SIE) from 2001-2017. Albedos are calculated using fluxes from CERES-EBAF Ed 4.1 and SIE estimates are from the NSIDC. Dashed vertical lines mark September 2007 and 2012, the lowest SIE on record. The surface albedo anomalies closely track the SIE anomalies and both exhibit clear negative trends over this time period. TOA albedo anomalies, on the other hand, are often decoupled from the surface and the trend is much more difficult to discern.

2012 had the lowest sea ice extent recorded during the satellite era, and the reduced sea ice in turn clearly lowered the surface albedo. Viewed from space, however, the September 2012 decline in TOA albedo was less than half that at the surface. This decoupling is largely due to clouds in the intervening atmosphere that are observed to modulate the influence of surface albedo on the TOA albedo by as much as a factor of two (Sledd and L'Ecuyer, 2019).

### 3.2.2 CMIP6

To investigate the changes in SW absorption beyond our observational record in Chapter 5, we analyze the output of 18 models participating in CMIP6 (Eyring et al., 2016), listed in Table 3.1. We use the historical forcing run, that covers the years from 1850 to 2014, and two shared societal pathways (SSPs) from the ScenarioMIP deck. We compare SSP2 ("middle of the road" scenarios with moderate population and economic growth) with an end of

TABLE 3.1: Models included from phase six of the Coupled Model Intercomparison Project.

<b>Model</b>	<b>Modeling Center</b>	<b>ATM Grid (lon/lat)</b>	<b>OCN Grid (lon/lat)</b>
ACCESS-CM2	Commonwealth Scientific and Industrial Research Organisation	192 x 144	360 x 300
ACCESS-ESM1-5	Commonwealth Scientific and Industrial Research Organisation	192 x 145	360 x 300
BCC-CSM2-MR	Beijing Climate Center	320 x 160	360 x 232
CESM2	National Center for Atmospheric Research	288 x 192	320 x 384
CESM2-WACCM	National Center for Atmospheric Research	288 x 192	320 x 384
CanESM5	Canadian Centre of Climate Modelling and Analysis	128 x 64	361 x 290
EC-Earth3	EC-Earth Consortium	512 x 256	362 x 292
EC-Earth3-Veg	EC-Earth Consortium	512 x 256	362 x 292
GFDL-ESM4	NOAA Geophysical Fluid Dynamics Laboratory	360 x 180	720 x 576
INM-CM4-8	Institute for Numerical Mathematics	180 x 120	360 x 318
INM-CM5-0	Institute for Numerical Mathematics	180 x 120	720 x 720
IPSL-CM6A-LR	Institut Pierre-Simon Laplace	144 x 143	362 x 332
MIROC6	Japan Agency for Marine-Earth Science and Technology	256 x 128	360 x 256
MPI-ESM1-2-LR	Max Planck Institute for Meteorology	192 x 96	256 x 220
MPI-ESM1-2-HR	Max Planck Institute for Meteorology	384 x 192	802 x 404
MRI-ESM2-0	Meteorological Research Institute	320 x 160	128 x 64
NESM3	Nanjing University of Information Science and Technology	192 x 96	362 x 292
NorESM2-LM	Norwegian Climate Center	144 x 96	360 x 384

century radiative forcing of  $4.5 \text{ Wm}^{-2}$  (SSP245) and SSP5 ("business as usual" scenarios with strong economic growth relying on fossil-fuels) with radiative forcing of  $8.5 \text{ Wm}^{-2}$  (SSP585) (O'Neill et al., 2016). These scenarios include years 2015-2100. The first ensemble member (r1i1p1f1) is used from each model, and the native resolution of each model is kept before each variable is averaged or summed over the Arctic. Variables that are averaged (e.g. total cloud fraction, surface air temperature) are weighted by grid box area, while most other variables are cumulative (e.g. sea ice area) and are summed over the Arctic. For grid boxes that contain the Arctic circle, the area is recalculated such that only the area north of  $66.5$  is included in the sum or average.

## 3.3 Uncertainty in Forced and Natural Arctic Solar Absorption Variations in CMIP6 Models

### 3.3.1 Methods

#### 3.3.1.1 Time to Emergence

This analysis uses the detection of statistically significant forced responses in time series that include natural variability to query the existence of observed SW absorption trends in the Arctic and evaluate their representation in modern GCMs. While hypothesis testing can determine when a trend is different from zero for a chosen confidence level, it does not take into account variance or autocorrelation that are common in geophysical time series. In the 1990s, Tiao et al. (1990) and Weatherhead et al. (1998) published methods for trend detection in geophysical applications that take these issues into account. Their methods of trend detection first assume the time series of interest can be modeled as the sum of a mean state with a linear trend,  $\omega$ , and noise. The noise is assumed to be an autoregressive order one (AR(1)) process with one-lag autocorrelation  $\phi$  and variance  $\sigma^2$ . The common variance (of the random fluctuations about zero in the noise that is assumed to be a white noise process),  $\sigma_e^2$ , is related to the variance of the noise by

$$\sigma_e^2 = \text{Variance}(N_t) = \sigma_N^2 * (1 - \phi^2). \quad (3.1)$$

The variance and autocorrelation are calculated from the de-trended time series of anomalies.

As in Weatherhead et al. (1998) and Chepfer et al. (2018), we consider a trend to have emerged at the 95% confidence level when it is at least twice as large as the standard deviation of the measured trend:  $|\hat{\omega}/\sigma_{\hat{\omega}}| > 2$ . The standard deviation of the trend,  $\sigma_{\hat{\omega}}$ , can be approximated as

$$\sigma_{\hat{\omega}} \approx \sigma_N \left[ \frac{12dt(1+\phi)}{T^3(1-\phi)} \right]^{1/2}, \quad (3.2)$$

where  $T$  is the length of the time series and  $dt$  is the time interval, in our case  $dt = 1$  for our annual observations discussed more below. This equation is adapted for annual time series, based on Lian (2017), from its original form using monthly time series ( $dt = 1/12$ ).

The time to emergence (TTE) is defined as how many years of observations are needed for a measured trend to be statistically significant. For a given time series, a trend is calculated and tested for significance over intervals of increasing length, e.g.  $[0,dt]$ ,  $[0,2dt]$ ,  $[0,3dt]$ ... $[0,T]$ . The confidence for each time interval is calculated from Eq. 3.2; the trend has emerged when it remains greater than two. This process is shown in Fig. 3.2 for an ensemble of synthetic time series, discussed shortly.

Chepfer et al. (2018) demonstrate that such an analysis provides a statistical basis for determining how long it takes forced climate changes to emerge from interannual variability in observational data records. Similar techniques were used to project trend detection of

broadband and spectral albedos (Feldman et al., 2011) and to inform instrument requirements for future climate monitoring satellite missions (Wielicki et al., 2013). When applied to global mean TOA irradiances, Phojanamongkolkij et al. (2014) found no discernible trend over 2000-2011 in reflected SW or emitted longwave radiation from CERES.

### 3.3.1.2 Synthetic Time Series

As in Chepfer et al. (2018) we combine TTE with synthetic time series to estimate the time needed for trends to be measurably greater than the climate variability. Synthetic time series are created that maintain the statistical behavior, e.g. autocorrelation and variance, of the original time series.

To calculate these synthetic time series, we again assume the data can be represented by the sum of a linear trend and noise. We take the variance calculated from Eq. 3.1 and generate a series of random noise with zero mean from it. On top of this noise we can add a linear trend, illustrated in Fig. 3.2a. Synthetic time series are continued to 150 years, which is long enough for trends from all CMIP6 models to emerge under both SSP245 and SSP585. Synthetic ensembles are composed of 300 individual time series. This process can be applied to models as well as observations to create ensembles of time series. While large ensembles from GCMs are an incredibly powerful tool for determining shifts in climate beyond the inherent internal variability (e.g. Onarheim and Årthun 2017), the authors know of no way to create a true large ensemble from observations as can be done with

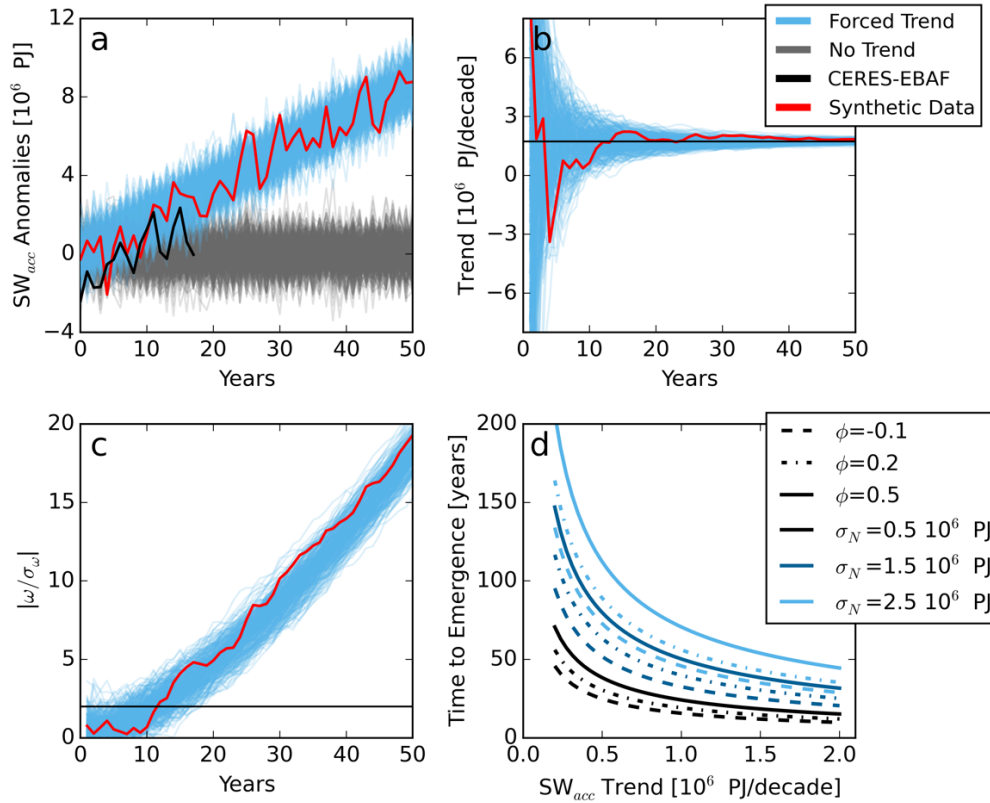


FIGURE 3.2: Trend detection using synthetic time series of surface clear-sky ( $SFC_{clr}$ ) accumulated shortwave ( $SW_{acc}$ ) over the Arctic from CERES-EBAF. (a) Synthetic time series (grey) are generated based on the variance and one-lag autocorrelation of the detrended CERES observations shown in black. A linear trend based on the CERES record is added to time series to generate the ensemble shown in light blue. A single realization from the resulting ensemble is highlighted in red. (b) For each synthetic time series, the linear trend is calculated from subsets of time periods increasing in length, e.g.  $[0,1]$ ,  $[0,2]$ ,... $[0,T]$ , where  $T$  is the full length of the time series. Trends calculated over the red time series in (a) are again highlighted. Initially trends can vary greatly, oscillating between positive and negative values before leveling off around the "true" trend, given by the solid black line. (c) When the trend is at least twice as large as the uncertainty, shown as the solid black line at  $|\hat{\omega}| = 2$  for the 95% confidence level, it is deemed to have "emerged". Theoretical values of time to emergence (TTE) are shown in (d) with ranges of variability ( $\sigma_N$ ), one-lag autocorrelation ( $\phi$ ), and trend found in models and observations.

GCMs. Using synthetic time series also allows us to examine GCMs that do not have large ensembles associated with them, expanding the number of models available for analysis.

### 3.3.1.3 Accumulated Absorbed Shortwave Radiation

The strong seasonality of the Arctic poses unique challenges for time series analysis. As mentioned earlier, this trend detection method is predicated on the assumption that the noise can be represented by an AR(1) process that is stationary. Many monthly time series in the Arctic do not meet these requirements, including monthly sea ice, albedo, and absorbed shortwave, as the variance and/or trends differ significantly throughout the seasons. We therefore calculate the net SW energy absorbed over the melt season, March through September. These months account for 95% of incoming SW radiation in the Arctic (Cao et al., 2016). The *accumulated SW*,  $SW_{acc}$ , is found by calculating the net SW flux ( $SW^\downarrow - SW^\uparrow$ ) absorbed at each grid box multiplied by the area of its grid box, converting it to a measure of power (with units Watts). Further multiplying by the duration (in seconds) of each month yields an accumulated energy (with units Joules). This average net SW energy is then summed over the Arctic, defined as the area north of the Arctic Circle, and summed over the melt season:

$$SW_{acc} = \sum_{m=3}^9 \sum_{i,j} (SW^\downarrow - SW^\uparrow)_{i,j} \times A_{i,j} \times t_m, \quad (3.3)$$

where  $A_{i,j}$  is the area of grid box  $i, j$  and  $t_m$  is the seconds in each month  $m$ .

Accumulated SW is a fundamental driver of Arctic climate variability. It is the net amount of SW energy input into the Arctic system that can go to melting sea ice and snow or heating the surface. Accumulated SW also behaves as a stationary time series, once de-trended, unlike many other variables in the Arctic. We calculate  $SW_{acc}$  at the TOA with all-sky fluxes ( $TOA_{all}$ ) and at the surface with clear-sky fluxes ( $SFC_{clr}$ ). Using these two boundaries and conditions allows us to quantify the difference clouds make at the TOA as compared to the surface if there were no clouds. Anomalies of  $SW_{acc}$  are shown in Fig. 3.3 for CMIP6 and observations. As seen with surface and TOA albedo anomalies (Fig. 3.1) clear-sky  $SW_{acc}$  increases faster than all-sky  $SW_{acc}$  at the TOA over the 21st century in all models.

Recall that the trend detection method assumes the detrended anomalies whose noise be represented by an AR(1) process. Increasing the time step, e.g. summing over the melt season, is intended to help meet this requirement, as mentioned in Gero and Turner (2011). In observations the noise has no significant autocorrelations at the 95% confidence level, which would suggest a white noise process, but this may be due to the short record length requiring large autocorrelations ( $\geq 0.47$ ) to count as significant, shown in Fig. 3.4. In the majority of CMIP6 models,  $SW_{acc}$  noise appears as white or red noise over 1900-1999, for example MRI-ESM2-0 in Fig. 3.4. According to Phojanamongkolkij et al. (2014), the method of Weatherhead et al. (1998) is more accurate for white or red noise scenarios compared to other more general methods, e.g. Leroy et al. (2008), and they further suggest it is more appropriate for reflected SW irradiances.

Figure 3.2d shows the effect of trend, autocorrelation and variance on TTE using values

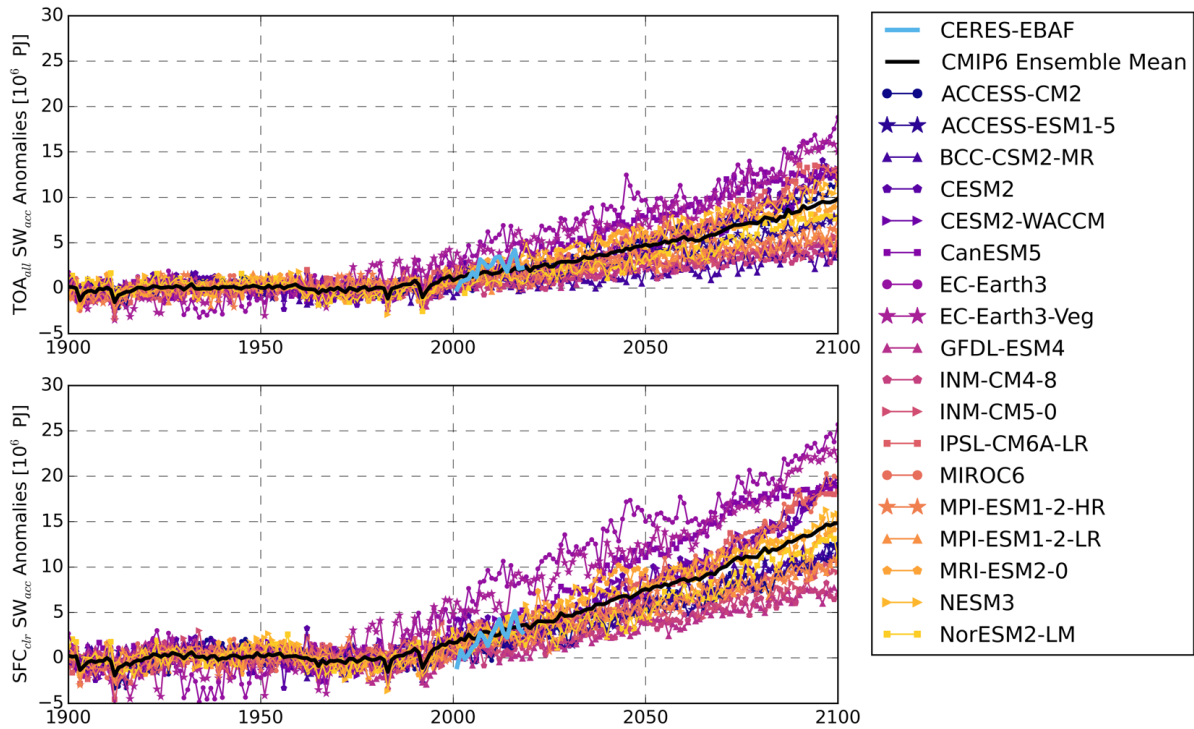


FIGURE 3.3: Anomalies of accumulated shortwave ( $SW_{acc}$ ) at the top of the atmosphere with clouds ( $TOA_{all}$ ) (top) and the surface without clouds ( $SFC_{clr}$ ) (bottom) in CMIP6 models and observations (CERES-EBAF). The ensemble mean from CMIP6 is shown in black. Anomalies for CMIP6 models are relative to 1900-1999, and those from observations are calculated relative to 2001-2018 but shifted to align with the CMIP6 base state (the CMIP6 ensemble mean from 2001-2018 is calculated and added to the CERES anomalies). For a given model, clear-sky  $SW_{acc}$  anomalies at the surface are greater than all-sky anomalies at the TOA. However, there are large differences between models both in terms of the magnitude and variability of anomalies.

representative of observations and CMIP6 from Eq. 3 in Weatherhead et al. (1998). For smaller trends ( $\lesssim 0.1 \times 10^6$  PJ/decade) TTE is more sensitive to the trend than the noise or autocorrelation, but for  $SW_{acc}$  trends larger than approximately  $0.2 \times 10^6$  PJ/decade, noise and autocorrelation can have a more significant impact. The magnitude of trends that TTE is sensitive to also depends on the level of noise. When a time series has greater variance it is more difficult to distinguish between what is just noise and what is indeed a consistent trend. For example, the solid black line ( $\phi=0.5$  and  $\sigma_N=0.5 \times 10^6$  PJ) is flatter across trends

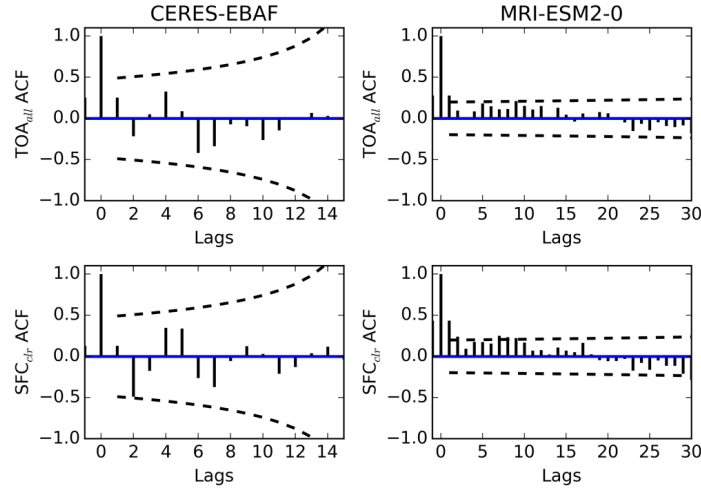


FIGURE 3.4: Autocorrelation functions (ACF) for accumulated shortwave ( $SW_{acc}$ ) anomalies at the top of the atmosphere with clouds ( $TOA_{all}$ ) (top row) and the surface without clouds ( $SFC_{clr}$ ) (bottom row) in observations (CERES-EBAF) (left column) and a typical climate model, MRI-ESM2-0 (right column). While no autocorrelations are significant at any lags (95% confidence interval shown as the dashed line), this may be in part due to the short record (18 years). When ACF are calculated over longer time periods in CMIP6 models, shown here for 1900-1999,  $SW_{acc}$  anomalies usually appear as red or white noise.

ranging from  $0.1-0.2 \times 10^6$  PJ/decade than the solid light blue line ( $\phi=0.5$  and  $\sigma_N=2.5 \times 10^6$  PJ) over the same range. Similarly, if a time series has high autocorrelation, what might appear to be a trend could simply be the propagation of an anomaly forward in time.

While the time series of annual  $SW_{acc}$  is a statistically convenient variable, using it instead of monthly averages shortens the data record length from monthly to annual reporting, from  $12 \times 18$  data points to just 18. With such a short time period, it is reasonable to wonder if 18 years of satellite measurements are enough to observe a trend even with the rapid changes observed in the Arctic. The answer will be discussed in the following section.

TABLE 3.2: CERES-EBAF properties for all-sky top of atmosphere ( $TOA_{all}$ ) and clear-sky surface ( $SFC_{clr}$ ) accumulated shortwave ( $SW_{acc}$ ). Noise, one-lag autocorrelations and trends are from 2001-2018. Mean time to emergence (TTE) is calculated from 300 synthetic time series using these statistics, with standard deviations given in parentheses.

	<b>Noise [<math>10^6</math> PJ]</b>	<b>Autocorrelation</b>	<b>Trend [<math>10^6</math> PJ/dec]</b>	<b>TTE [years]</b>
$TOA_{all}$	0.77	0.29	0.72	22 (5)
$SFC_{clr}$	0.84	0.14	1.7	12 (3)

### 3.3.2 Results and Discussion

From the 18 year CERES record, the trend in  $SW_{acc}$  at the surface without clouds,  $1.7 \times 10^6$  PJ/decade, is statistically significant using the criteria  $|\frac{\hat{\omega}}{\sigma_{\hat{\omega}}}| > 2$ , but the trend in  $SW_{acc}$  at the TOA under all-sky conditions,  $0.7 \times 10^6$  PJ/decade, is not. These trends and other statistics for CERES are listed in Table 3.2. The limited period of observations exhibits the striking feature that it is long enough to unambiguously detect anthropogenically-forced clear-sky variations in absorbed SW radiation but not overall all-sky trends. If the  $TOA_{all}$  trend calculated over 2001-2018 continues into the future, we find that it would take an average of 22 years for it to emerge above interannual variability. This extrapolation of the observed  $TOA_{all}$   $SW_{acc}$  trend into the future to derive a hypothetical observational TTE is intended to suggest an approximate length of observational record where we might anticipate observing a significant measured trend; it is not an exact prediction of when the trend will emerge. This hypothetical  $TOA_{all}$  TTE ( $TTE_{all}$ ) is nearly twice as long as that for  $SFC_{clr}$  found using a synthetic ensemble (12 years). The difference in observational TTE with and without clouds stems from the fact that the measured  $SFC_{clr}$  trend is more than twice as large as that of  $TOA_{all}$ , consistent with Sledd and L’Ecuyer (2019), while the noise and autocorrelations are similar (Table 3.2).

We can compare the results of calculating TTE from observations and models. Figure 3.5a shows the mean TTE from synthetic ensembles derived from CMIP6 models only using the variance and autocorrelation over 2001-2018 forced with the trend evaluated from 2001-2100 for SSP245 and SSP585. Mean TTE from Fig. 3.5a are listed in Table 3.3. Across CMIP6, models predict the  $SW_{acc}$  trends emerging within 8-35 years without clouds at the surface and 8-39 years with clouds at the TOA. The range of mean  $SFC_{clr}$  TTE ( $TTE_{clr}$ ) in models is larger than the  $2\sigma$  uncertainty of observations, 6-18 years, but more than half of the models predict mean TTE within one standard deviation of the observational TTE for at least one of the SSP. However, there are some differences between models and observations. Under SSP245 (585), six (16) models predict mean  $TOA_{all}$  trends to have emerged within the observational record, contrary to our earlier findings. For  $SFC_{clr}$  trends, 17 models under SSP245 suggest a longer record would be needed for the trend emerge, reducing to only 11 models under SSP585, which is also in contrast to the observational results.

Different relationships between  $TTE_{all}$  and  $TTE_{clr}$  also emerge in Fig. 3.5a compared to TTE calculated using CERES. Under SSP245, half of the 18 models show clouds lengthening the TTE as in observations. Three models have mean TTE that are equal with and without clouds, and six of models actually show the opposite behavior of observations, with the all-sky  $SW_{acc}$  trend emerging before the clear-sky trend. This result is unexpected based on our understanding of how clouds influence albedo in present day observations, as shown in Fig. 3.1. When TTE is calculated using SSP585, only six models show clouds lengthening the TTE, three models show clouds having no effect on TTE, and nine models predict that clouds shorten the TTE.

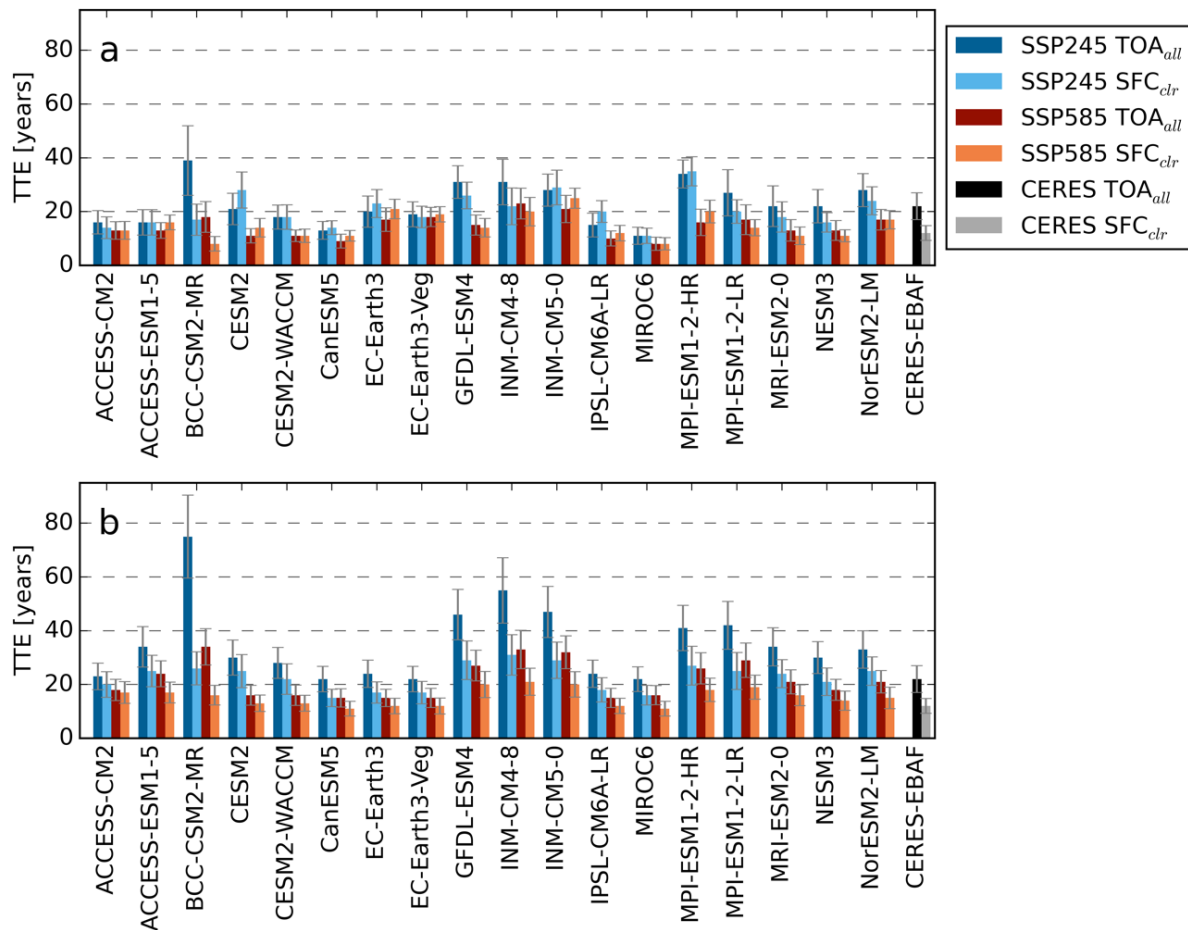


FIGURE 3.5: (a) Mean time to emergence (TTE) of accumulated shortwave ( $SW_{acc}$ ) trends from 300 synthetic time series based on CERES-EBAF observations and CMIP6 models. Variance and autocorrelation are calculated over 2001-2018 and forced with trends over 2001-2100 for CMIP6 models and 2001-2018 for CERES-EBAF. Error bars represent one standard deviation around the mean TTE. Two shared societal pathways (SSP) are shown: a "middle of the road" future (SSP245) and a "business as usual" future (SSP585). Observations suggest that trends in clear-sky surface ( $SFC_{clr}$ )  $SW_{acc}$  have emerged in the 18 year observational record while all-sky top of atmosphere ( $TOA_{all}$ )  $SW_{acc}$  will require more years of observations to discern. (b) TTE calculated from synthetic time series with variability based on CERES-EBAF forced with trends from CMIP6 models used in (a). The difference between (a) and (b) shows the impacts of model internal variability on  $SW_{acc}$  TTE. Values from bar plots are given in Tables 3.3 and 3.4

TABLE 3.3: Mean time to emergence (TTE) from 300 synthetic time series based on models only with noise and autocorrelation calculated from 2001-2018 forced with trends from 2001-2100. Standard deviations are given in parentheses.

	<b>TOA<sub>all</sub> TTE [years]</b>		<b>SFC<sub>clr</sub> TTE [years]</b>	
	<b>SSP245</b>	<b>SSP585</b>	<b>SSP245</b>	<b>SSP585</b>
ACCESS-CM2	16 (5)	13 (5)	14 (5)	13 (5)
ACCESS-ESM1-5	16 (7)	13 (8)	16 (6)	16 (6)
BCC-CSM2-MR	39 (15)	18 (15)	17 (6)	8 (6)
CESM2	21 (6)	11 (6)	28 (6)	14 (6)
CESM2-WACCM	18 (6)	11 (6)	18 (6)	11 (6)
CanESM5	13 (5)	9 (5)	14 (3)	11 (3)
EC-Earth3	20 (5)	17 (5)	23 (4)	21 (4)
EC-Earth3-Veg	19 (5)	18 (5)	18 (4)	19 (4)
GFDL-ESM4	31 (9)	15 (9)	26 (7)	14 (7)
INM-CM4-8	31 (12)	23 (12)	22 (7)	20 (7)
INM-CM5-0	28 (9)	21 (9)	29 (7)	25 (7)
IPSL-CM6A-LR	15 (5)	10 (5)	20 (5)	12 (4)
MIROC6	11 (5)	8 (5)	11 (4)	8 (4)
MPI-ESM1-2-LR	34 (8)	16 (8)	35 (7)	20 (7)
MPI-ESM1-2-HR	27 (9)	17 (9)	20 (7)	14 (7)
MRI-ESM2-0	22 (7)	13 (7)	18 (5)	11 (5)
NESM3	22 (6)	13 (6)	16 (5)	11 (5)
NorESM2-LM	28 (7)	17 (7)	24 (5)	17 (5)

To distinguish the influence of internal variability from modeled trends, we generate new synthetic time series that combine the statistical characteristics ( $\sigma$  and  $\phi$ ) from observations with trends from CMIP6 models calculated over the 21st century (2001-2100), shown in Fig. 3.5b and listed in Table 3.4. To disentangle biases in model internal variability versus the external forcing, we can compare TTE calculated solely from models to TTE calculated from observations forced by model trends. A significant difference between Figs. 3.5a and 3.5b is the impact of clouds on TTE magnitude. Unlike in Fig. 3.5a, clouds always increase the TTE in Fig. 3.5b, consistent with observations, since in all models the SFC<sub>clr</sub> trend is larger than the TOA<sub>all</sub> trend. Biases in model noise and autocorrelations therefore must be

TABLE 3.4: Mean time to emergence (TTE) from 300 synthetic time series based on noise and autocorrelation from observations (CERES-EBAF) forced with trends from CMIP6 models over 2001-2100. Standard deviations are given in parentheses.

	<b>TOA<sub>all</sub> TTE [years]</b>		<b>SFC<sub>clr</sub> TTE [years]</b>	
	<b>SSP245</b>	<b>SSP585</b>	<b>SSP245</b>	<b>SSP585</b>
ACCESS-CM2	23 (5)	18 (5)	20 (5)	17 (5)
ACCESS-ESM1-5	34 (8)	24 (7)	25 (6)	17 (6)
BCC-CSM2-MR	75 (15)	34 (15)	26 (6)	16 (6)
CESM2	30 (6)	16 (6)	25 (6)	13 (6)
CESM2-WACCM	28 (6)	16 (6)	22 (6)	13 (6)
CanESM5	22 (5)	15 (5)	15 (3)	11 (3)
EC-Earth3	24 (5)	15 (5)	17 (4)	12 (4)
EC-Earth3-Veg	22 (5)	15 (5)	17 (4)	12 (4)
GFDL-ESM4	46 (9)	27 (9)	29 (7)	20 (7)
INM-CM4-8	55 (12)	33 (12)	31 (7)	21 (7)
INM-CM5-0	47 (9)	32 (9)	29 (7)	20 (7)
IPSL-CM6A-LR	24 (5)	15 (5)	18 (4)	12 (4)
MIROC6	22 (5)	16 (5)	16 (4)	11 (4)
MPI-ESM1-2-HR	41 (8)	26 (8)	27 (7)	18 (7)
MPI-ESM1-2-LR	42 (9)	29 (9)	25 (7)	19 (7)
MRI-ESM2-0	34 (7)	21 (7)	24 (5)	16 (5)
NESM3	30 (6)	18 (6)	21 (5)	14 (5)
NorESM2-LM	33 (7)	21 (7)	25 (5)	15 (5)

a significant driver of why clouds shorten TTE in some models.

Figure 3.5b further suggests that few models capture the difference between TOA<sub>all</sub> and SFC<sub>clr</sub> trends. Under either SSP, nine of the 18 models predict TTE<sub>clr</sub> within one standard deviation of observations. Of these models, all but one (NorESM2-LM) predict that the TOA<sub>all</sub> trend should have emerged within the CERES record, which we do not observe. This is to say models may capture trends at one boundary but rarely both. Although we cannot know in the present what the trend in TOA<sub>all</sub> SW<sub>acc</sub> will be over the coming decades, we can characterize its current behavior, and it seems that many models may not fully capture the impact of clouds on SW<sub>acc</sub> in the Arctic.

The remainder of this study investigates how the statistical properties of  $SW_{acc}$  affect TTE, what physically drives those properties, and why some models show behavior different than observations in regards to clouds lengthening TTE.

### 3.3.2.1 A signal to noise problem

In this section we assess the relative importance of  $SW_{acc}$  trend, autocorrelation and variability on TTE across climate models, beginning with how these statistics themselves can vary between distinct epochs within an individual model. While the observational record provides a limited number of years from which to calculate these statistics, that is not a limitation when using climate models. With the longer time series available from CMIP6 the influence of using different time periods on estimated TTE can be investigated, with the results being model-dependent. Using synthetic ensembles created by varying the starting year and length of time used to calculate the noise and autocorrelation (1983-2000, 1983-2018, 2001-2018, 2001-2036) we find that only seven (six) of the 18 models generate mean TTE for  $TOA_{all}$  trends ( $SFC_{clr}$ ) within one standard deviation of each other regardless of which time period is used to generate the synthetic time series. The distinct behaviors of different models are exemplified by EC-Earth3 in Fig. 3.6, which exhibits a tightly constrained TTE, and GFDL-ESM4 where TTE can more than double across the range of time periods explored (plots for all models are provided in the supplemental material). In all cases, trends are held constant for each model computed from either 1983 or 2001 through 2100.

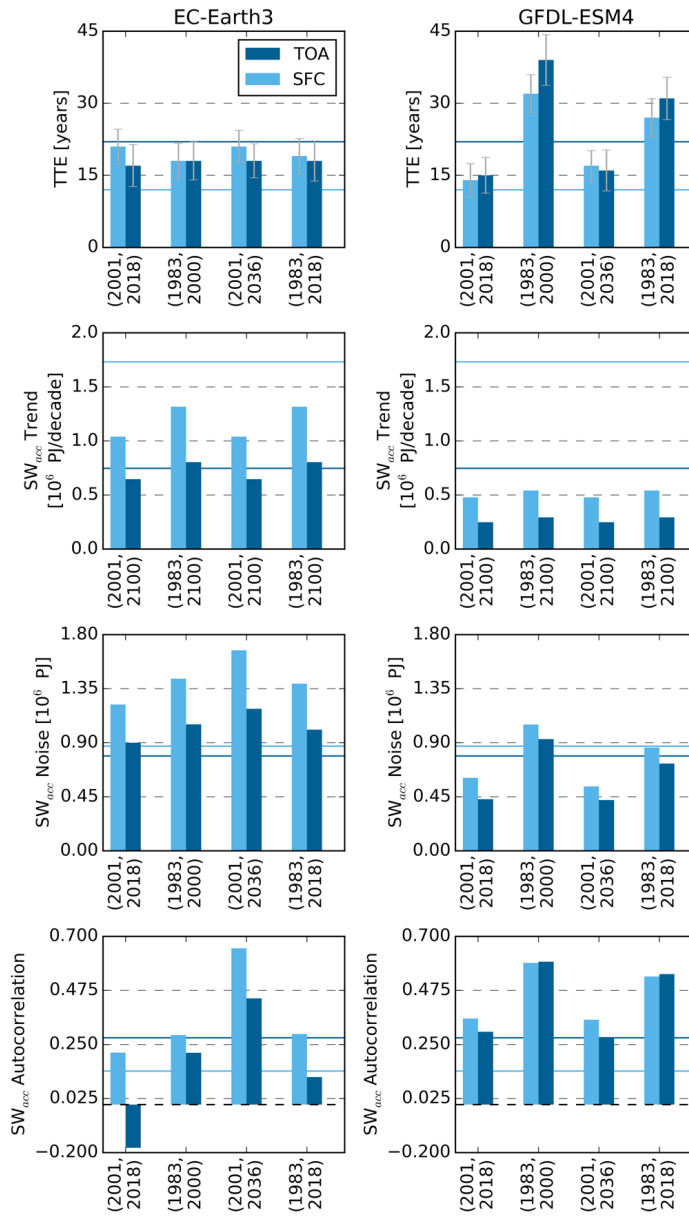


FIGURE 3.6: Time to emergence (TTE) and statistical properties of all-sky top of atmosphere ( $TOA_{all}$ ) and clear-sky surface ( $SFC_{clr}$ ) accumulated shortwave ( $SW_{acc}$ ) used to calculate TTE from four different time periods. Solid lines represent values from CERES-EBAF. TTE derived from EC-Earth3 (left) is generally independent of the time period used to calculate it in spite of large variations in  $SW_{acc}$  one-lag autocorrelation. Meanwhile, GFDL-ESM4 (right) TTEs vary by more than a factor of two between time periods. This variability is mostly due to differences in noise and autocorrelation as the  $SW_{acc}$  trends are fairly consistent, regardless of the starting year. While only time periods from SSP245 are shown, the results are consistent when using SSP585.

For models where TTE varies markedly with epoch, the noise and autocorrelation are more sensitive to the time period than the trend is. Furthermore, noise and autocorrelation seem to be more sensitive to which epoch is used rather than the length of the time period analyzed. For example, noise and autocorrelation in GFDL-ESM4 are relatively low during 2001-2018 and 2001-2036, while they increase during time periods that start in 1983 (1983-2000 and 1983-2018). On the other hand, trends in  $SW_{acc}$  are fairly constant regardless of the time period for all models when determined over the 21st century. The consistency is likely due, in part, to the fact that the trend is measured over many decades, regardless of the starting year. This supports the assertion that we are testing for a consistent and measurable trend due to the external forcing. However, we note that if trends are calculated over shorter time periods, such as over 2001-2018 to compare to our observational record, they are often not representative of the true forcing, and are in fact occasionally negative (not shown). While only four different time periods are shown in Fig. 3.6, the same conclusions are drawn when more time periods are tested.

In the remaining analysis, we adopt the synthetic ensembles Fig. 3.5a is based on, where 2001-2018 is used to calculate the variance and autocorrelation and 2001-2100 is used to calculate trends. While the relationships between TTE and environmental factors discussed later are robust regardless of the chosen time periods, this choice of years allows a more

---

The changes in measured  $SW_{acc}$  variability may be due to the eruption of Mt. Pinotubo in 1991 that caused a decrease in  $SW_{acc}$ . For models with relatively low variability, this decrease in  $SW_{acc}$  would appear large and increase the variance for time periods including 1991 as compared to time periods without it. For models with relatively large  $SW_{acc}$  variability, the decrease in  $SW_{acc}$  due to Mt. Pinotubo would not be atypical and therefore have a minimal impact on the measured variability.

consistent comparison with observations. Even in this one time period there are large inter-model differences in  $SW_{acc}$  forced trends and internal variability, shown in Fig. 3.7. Trends in  $SW_{acc}$  vary by an order of magnitude under SSP585 both with and without clouds and under SSP245 without clouds. Internal variability also varies significantly, doubling or even quadrupling across models, depending on the boundary and SSP. Seven of the models have variances within observational uncertainty for all boundaries and SSPs (using an F-test with 95% confidence). Twice as many models (eight) differ significantly from observations for  $TOA_{all}$  than  $SFC_{clr}$  (four). While models disagree on the sign of  $SW_{acc}$  autocorrelation, most fall within the  $2\sigma$  range of uncertainty for the observational values.

These inter-model differences in  $SW_{acc}$  trend, autocorrelation and variability in turn lead to differences in TTE. Mathematically, the main influence on TTE is the ratio of the forced  $SW_{acc}$  trend to the internal variability, i.e. the climate signal to noise ratio (SNR), shown in Fig. 3.7a. The SNR captures the primary question of TTE, that is, when does a trend rise above the noise? Larger trends or smaller variability can increase SNR and reduce the TTE, but neither the trend (Fig. 3.7b) nor noise (Fig. 3.7c) alone is as strongly correlated to TTE as their ratio, both with and without clouds. Across models the trend has a greater impact on TTE than noise because it can vary by an order of magnitude while the noise varies by a factor of four. Overall the autocorrelation is weakly related to the TTE, despite ranging from positive to negative (Fig. 3.7d).

For a given model, the greatest differences between SSPs are in the strength of the forced  $SW_{acc}$  trends and the resulting SNR. As previously mentioned, SSP585 shows stronger trends

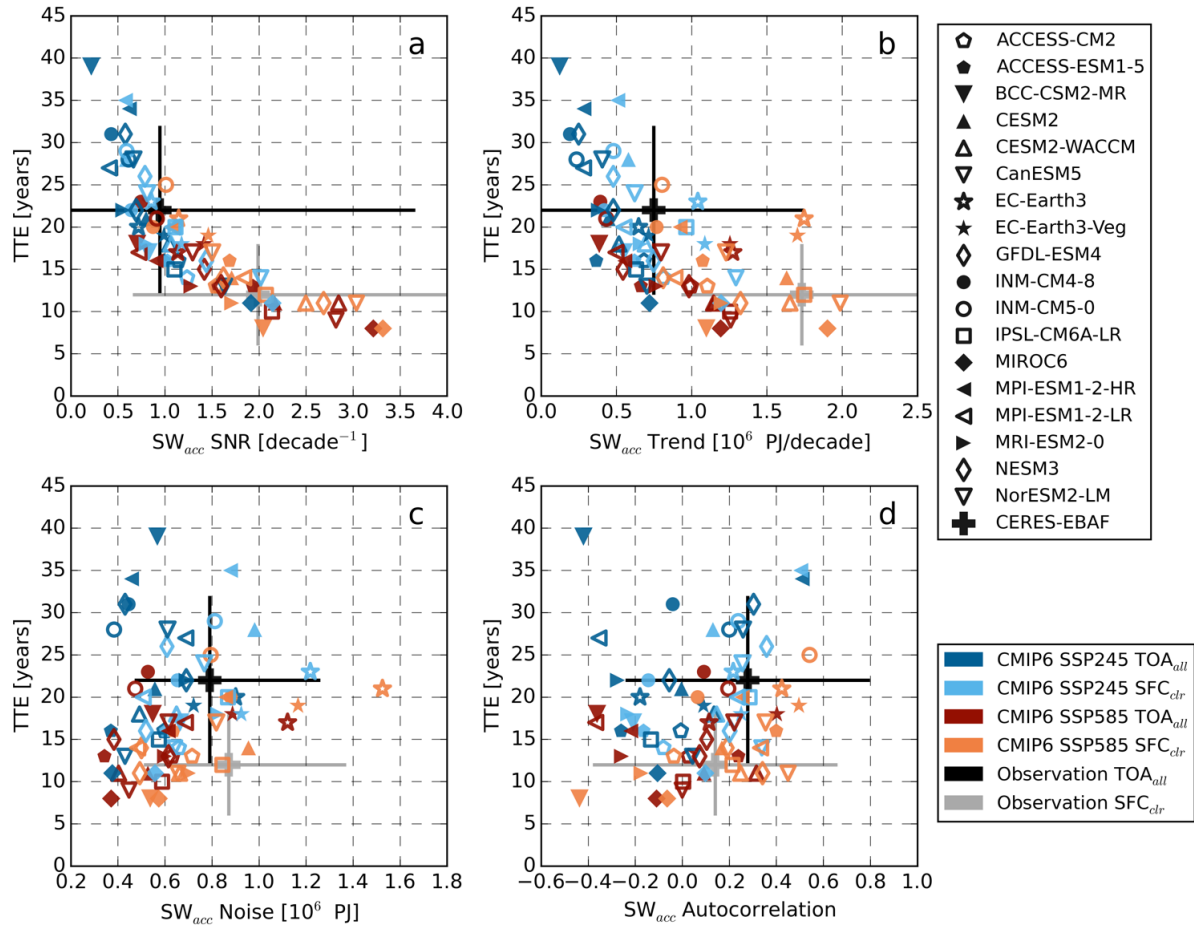


FIGURE 3.7: Mean time to emergence (TTE) and accumulated shortwave ( $SW_{acc}$ ) statistical properties from 2001-2018 (noise and autocorrelation) and 2001-2100 (trend) in CERES-EBAF and CMIP6. Error bars represent the  $2\sigma$  range of uncertainty in observations. The signal to noise ratio (SNR) has the strongest relationship to TTE as it represents the strength of the trend against the variability, both with clouds at the top of the atmosphere ( $TOA_{all}$ ) and without clouds at the surface ( $SFC_{clr}$ ). Clouds reduce the magnitude of  $SW_{acc}$  trends, and sometimes the noise, within a given model. In observations, clouds significantly reduce the SNR, but for most models in CMIP6 they only have a moderate effect on SNR.

in  $SW_{acc}$  than in SSP245, and therefore shorter TTE. Models with smaller trends than observations (+ in Fig. 3.7) often have longer TTE, and vice-versa. Such is the case under SSP245 where  $SFC_{clr}$  trends (light blue) are underestimated in Fig. 3.7b. The inverse may be true for  $TOA_{all}$  trends (dark red) under SSP585, but it is uncertain given that the  $TOA_{all}$

trend has not emerged in the observations. Because of the different trend magnitudes, under SSP245 the  $SW_{acc}$  trend is a stronger predictor of TTE than noise because TTE is more sensitive to trend at these lower magnitudes, whereas noise and autocorrelation influence TTE more under SSP585, consistent with our discussion of theoretical TTE with Fig. 3.2d in Section 3.3.1.3. Both SSPs have similar ranges of noise and autocorrelation across models, which is consistent with the SSPs not diverging until 2015. While the full range of  $SW_{acc}$  variability encompasses the observations in Fig. 3.7c, more models underestimate the observed variability in  $SW_{acc}$ , particularly at the TOA with clouds.

Differences between  $TOA_{all}$  and  $SFC_{clr}$   $SW_{acc}$  behavior are fairly consistent across SSPs as well. As mentioned previously, clouds dampen the  $SW_{acc}$  trend at the TOA but not at the surface, and in models clouds also appear to reduce the variance of  $SW_{acc}$ . This impact has a few consequences. First, it means that trends are more linearly related to TTE for  $TOA_{all}$ , especially for SSP245 (dark blue in Fig. 3.7b), whereas  $SFC_{clr}$  noise and autocorrelation have stronger relationships to TTE than  $TOA_{all}$ , more notably for SSP585 (orange in Figs. 3.7c and 3.7d). Because clouds both dampen the signal and noise in models, the SNR are similar for  $SFC_{clr}$  and  $TOA_{all}$ .

Not all of these impacts of clouds are seen in observations, though. In observations, clouds reduce the measured  $SW_{acc}$  trends by more than a factor of two (black versus gray + in Fig. 3.7b). Clouds have only a small impact on the noise and autocorrelation, so they ultimately reduce the SNR by a factor of two between  $SFC_{clr}$  and  $TOA_{all}$  as well. This impact of clouds

is not always found in CMIP6 models despite the observational values being within the ensemble ranges.

### 3.3.2.2 Impact of sea ice on TTE

Sea ice influences numerous aspects of the Arctic climate, including  $SW_{acc}$ . The more rapidly and consistently sea ice disappears, the faster the  $SW_{acc}$  trend emerges, as shown in Fig. 3.8. Trends in sea ice area (SIA) over the 21st century strongly influence the TTE both with and without clouds and under SSP245 and SSP585, Fig. 3.8b. The SNR of SIA is also correlated with TTE, Fig. 3.8a, mostly due to the impact of SIA decline and to a lesser extent the variability of SIA (Fig. 3.8c). We find that SIA autocorrelation has little impact on  $SW_{acc}$  TTE (Fig. 3.8d) likely because persistence of sea ice anomalies tend not to extend beyond a year (Blanchard-Wrigglesworth et al., 2011).

The importance of SIA on  $SW_{acc}$  is physically consistent with our understanding of the Arctic energy budget and the ice albedo feedback. However, there are some subtleties that are smoothed over when using  $SW_{acc}$  and SIA. SIA and  $SW_{acc}$  encompass the entire melt season, which removes some of the strong differences between March and September. While sea ice decline is largest in the fall when it reaches its minimum, incoming SW peaks in June. Sea ice in mid-summer, therefore, has a larger impact on the Arctic albedo and absorbed SW. Relating SIA to  $SW_{acc}$  also ignores changes in sea ice albedo throughout the melt seasons, which can be significant when melt ponds form (Perovich et al., 2002).

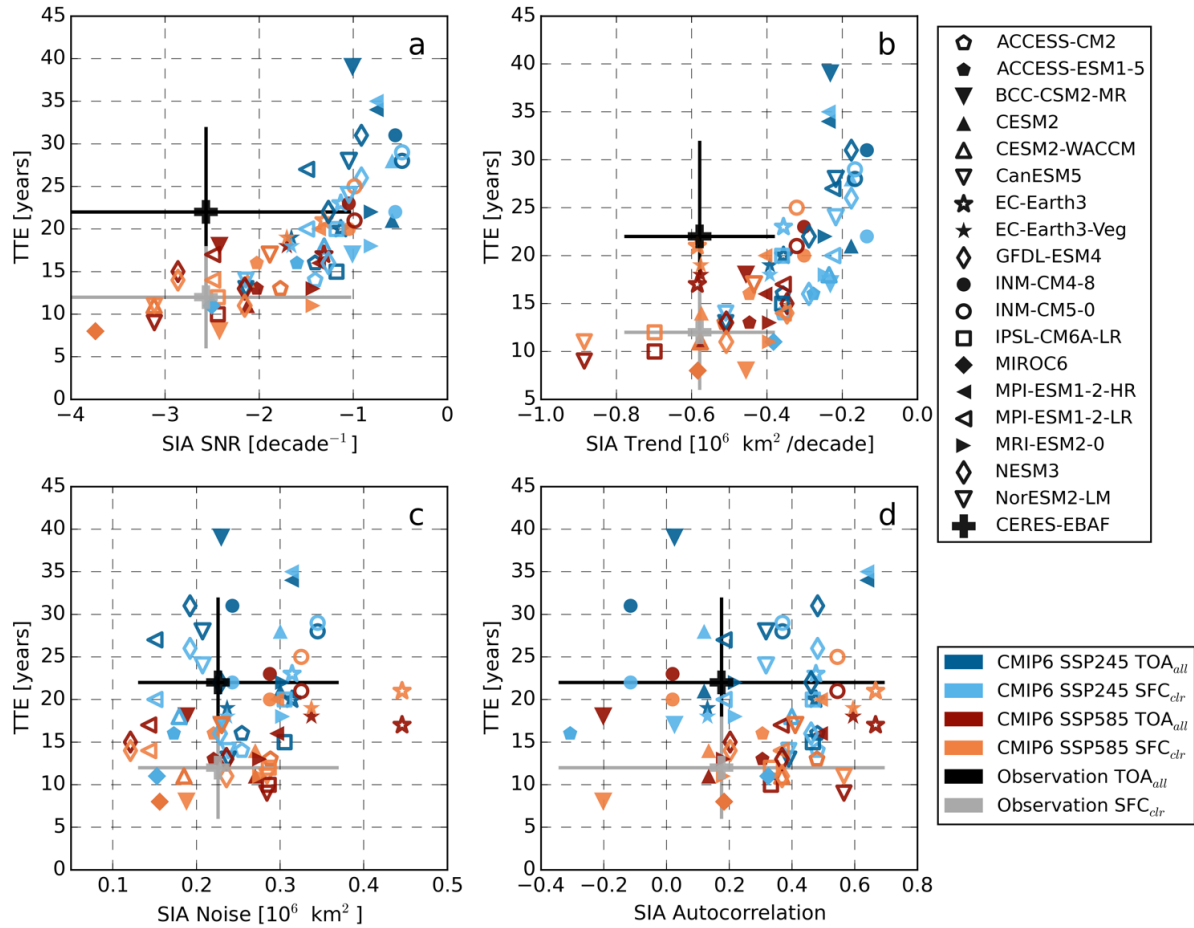


FIGURE 3.8: Relationship between mean time to emergence (TTE) for accumulated short-wave ( $SW_{acc}$ ) and the statistical properties of sea ice area (SIA) averaged over the melt season (March-September) from 2001-2018 (noise and autocorrelation) and 2001-2100 (trend). Error bars represent the  $2\sigma$  range of uncertainty in observations. The greater the SIA decline, the faster the  $SW_{acc}$  trend emerges, regardless of cloud cover. SIA trend and signal to noise ratio (SNR) both impact  $SW_{acc}$  at the surface without clouds ( $SFC_{clr}$ ) and the top of the atmosphere with clouds ( $TOA_{all}$ ). SIA noise is related to  $SFC_{clr}$  TTE but has a minimal influence on  $TOA_{all}$  TTE.

While SIA strongly influences  $SW_{acc}$  under both SSPs, there are some slight differences between the two forcing pathways that are highlighted in Fig. 3.8. As would be expected, SIA trends are larger under SSP585 due to increased GHG emissions and warming for individual models. SIA observations calculated over 2001-2018 are closer to values from SSP585, but there is some overlap in the rate of SIA decline between SSPs when looking at the full

CMIP6 ensemble. SIA noise also seems to influence TTE more in SSP585 than SSP245, as was the case for  $SW_{acc}$  in Fig. 3.7b. This is likely due to the greater trends in SIA pushing TTE into a regime where noise and autocorrelation can have greater impacts, as discussed with theoretical  $SW_{acc}$  TTE in Fig. 3.2d.

### 3.3.2.3 Inconsistent Cloud Impacts on TTE

Figure 3.8 further suggests that model cloud biases may influence their predictions of the emergence of forced variations in all-sky  $SW_{acc}$ . Recently observed trends in SIA fall within the envelope of behavior predicted by the CMIP6 ensemble, and the relationship between  $TTE_{clr}$  and SIA seen in observations is represented in models. All models, however, underestimate the relationship between  $TTE_{all}$  and SIA trend and SNR. For example, while EC-Earth3 produces a similar trend in SIA to observations, the  $TTE_{clr}$  from EC-Earth3 actually resembles the  $TTE_{all}$  projected from observations (Fig. 3.7b). The  $TTE_{all}$  is seven years shorter in EC-Earth3 than observations and is actually shorter than  $SFC_{clr}$ , while observations suggest that clouds lengthen the TTE. This is a common bias in which many models seem to struggle predicting the impact of clouds on forced climate trends.

We now turn to the question of why clouds shorten the TTE in some models contrary to observations and physical intuition. In observations, clouds increase the TTE from  $SFC_{clr}$  to  $TOA_{all}$  because the  $SW_{acc}$  trend is smaller with clouds while the noise and autocorrelations are similar (Table 3.2). Admittedly, the  $TOA_{all}$  trend and therefore TTE are uncertain in observations, but we can find the minimum possible difference in  $TTE_{all}$  and  $TTE_{clr}$ . If

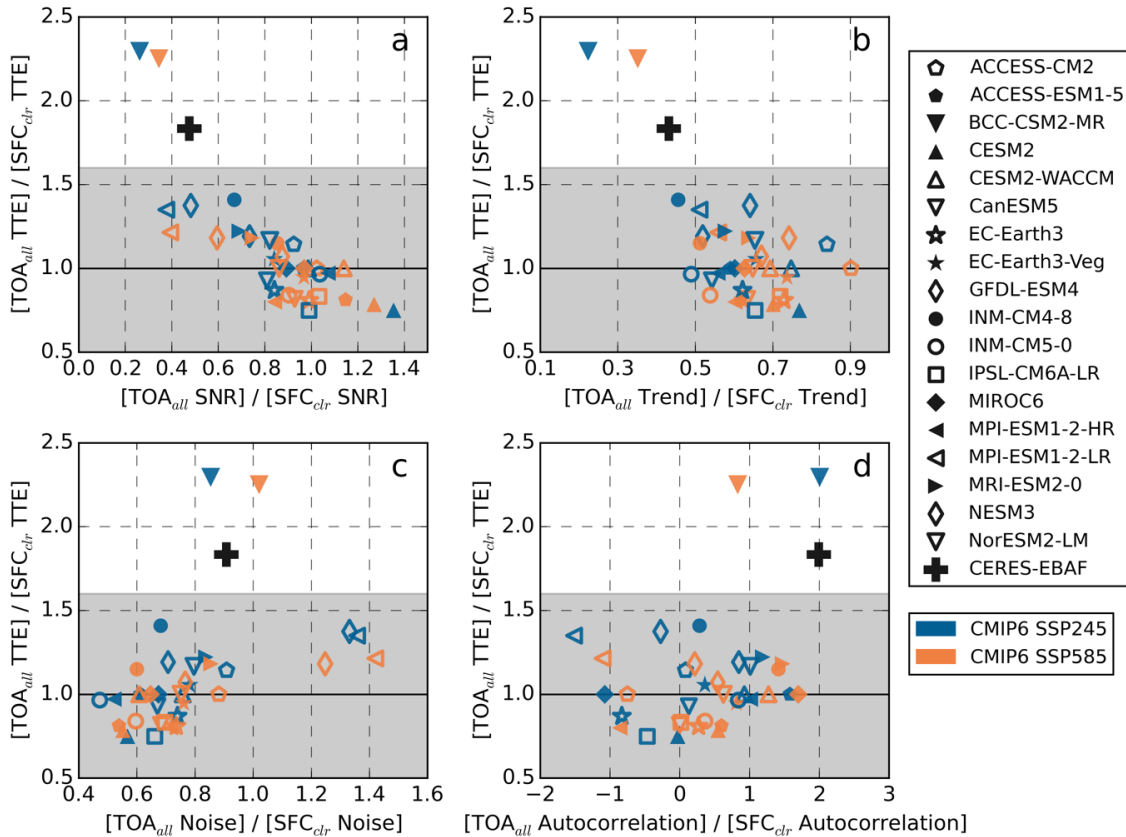


FIGURE 3.9: Dependence of the ratio of  $TOA_{all}$  to  $SFC_{clr}$  accumulated shortwave ( $SW_{acc}$ ) TTE to  $SW_{acc}$  statistical properties. The shaded region represents TTE ratios below the minimum ratio if one more year of observations proved the  $TOA_{all}$  trend significant. The relative strength of the signal to noise ratio (SNR) with and without clouds is negatively related to the relative length of TTE. When the TOA and surface  $SW_{acc}$  trends are similar, the TOA  $SW_{acc}$  trend may emerge sooner if the natural variability at the surface is larger than that at TOA. This relationship holds for both shared societal pathways (SSP). Most models underestimate the influence of clouds damping the  $SW_{acc}$  trend and SNR has on the difference in TTE.

one more year of observations proved the  $TOA_{all}$  trend significant, e.g.  $TTE_{all}=18+1$ , the minimum ratio of  $TTE_{all}$  to  $TTE_{clr}$  would be  $\frac{19}{12} = 1.6$ , over a 50% increase. This cloud masking effect has been documented in several other studies and means that the  $SFC_{clr}$  SNR is larger than that of  $TOA_{all}$ . Many models do not reproduce these relationships, though. In Fig. 3.9, for example, only one model, BCC-CSM2-MR, predicts a  $TTE_{all}$  to  $TTE_{clr}$  ratio larger than observations or even the minimum ratio of  $TOA_{all}$  to  $SFC_{clr}$ , shown with the

shaded region in Fig. 3.9.

Because  $SW_{acc}$  SNR is strongly correlated with TTE, its ratio of  $TOA_{all}$  to  $SFC_{clr}$  is also strongly correlated to the ratio of TTE, shown in Fig. 3.9a. Above an SNR ratio of approximately 0.8, the  $TOA_{all}$  trend may emerge before the  $SFC_{clr}$ . In some models, clouds even cause the SNR to be higher at the TOA compared to the surface ( $\frac{TOA_{all}}{SFC_{clr}} > 1$ ), opposite observations. While the ratio of SNR is dependent on the ratio of trends with and without clouds, clouds dampen the  $SW_{acc}$  signal in all models (Fig. 3.9b). In order for the  $TOA_{all}$  trend to emerge first, clouds must also appreciably dampen the  $TOA_{all}$  variability (Fig. 3.9c).

For any given model, the ratios of TTE and  $SW_{acc}$  properties do not vary appreciably between SSPs. While  $SW_{acc}$  trends can differ by an order of magnitude between SSP245 and SSP585 in Fig. 3.7b, the ratios are never more than twice as large in Fig. 3.9b. For example, the ratio of trends in BCC-CSM2-MR (▼) only vary from 0.2 (SSP 245 - blue) to 3.5 (SSP585 - orange), with most other models varying even less between SSPs. That is to say, the impact of clouds on  $SW_{acc}$  is likely due to inherent model physics rather than uncertainty from external forcings.

So how do clouds influence the climate SNR and resulting TTE? Over the Arctic, models vary widely in their predicted cloud fraction (CF) responses over the melt season with some showing increases, others decreases, and some having no change (Fig. 3.10). The sign of modeled CF trend plays a significant role in defining the how surface albedo changes manifest themselves in changes in absorbed SW radiation at the TOA. Models that predict decreasing CF predict stronger  $TOA_{all}$   $SW_{acc}$  trends, stronger  $TOA_{all}$  SNR, and shorter  $TTE_{all}$

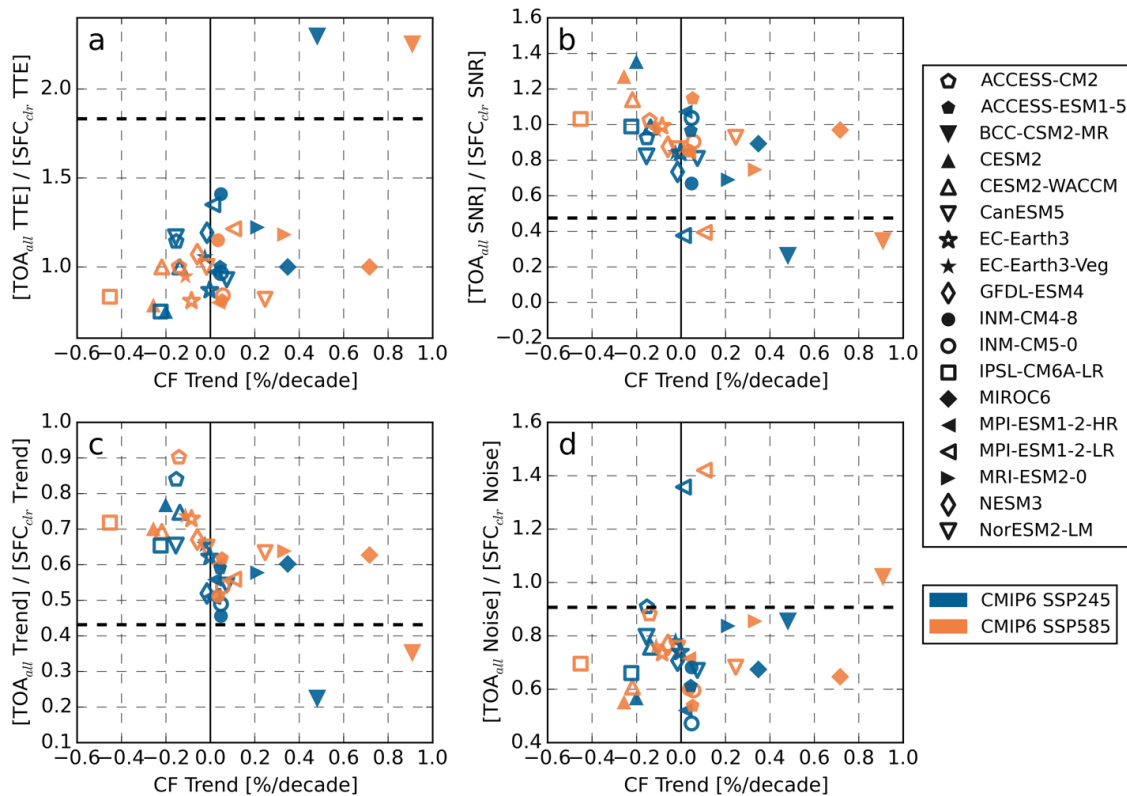


FIGURE 3.10: Role of 21st century cloud fraction (CF) trends in modulating the ratio of  $TOA_{all}$  to  $SFC_{clr}$  accumulated shortwave TTE. The atmosphere, and clouds in particular, account for much of the planetary albedo both globally and in the Arctic. Models that predict decreasing cloud cover over the 21st century amplify the effect of reduced surface albedo from sea ice on  $TOA SW_{acc}$  by both lowering the atmospheric contribution to the planetary albedo and revealing dark open ocean. This impact is linked to the relative strength of  $SW_{acc}$  trends and signal to noise ratio (SNR) with and without clouds in both shared societal pathways (SSP).

than exist at the surface, indicative of a cloud feedback that amplifies the influence of sea ice on absorbed shortwave radiation. This relationship is stronger under SSP585 as the magnitude of CF trends increases with climate forcing for any given model. Reduced cloud cover in models can reduce the planetary albedo in a few ways. Clouds directly reflect incoming SW at the TOA, so reduced cloud cover results in an increase of solar insolation at the surface. In addition, fewer clouds means that changes in the surface albedo are more directly seen from space, amplifying the albedo impact of sea ice loss. Models with negative CF

trend, therefore, have  $SW_{acc}$  trends that are closer in magnitude with and without clouds at the TOA and surface in Fig. 3.10c. At the opposite end of the spectrum, the only model that shows a TTE ratio greater than observations, BCC-CSM2-MR, also has the largest positive trend in CF and greatest difference between  $TOA_{all}$  and  $SFC_{clr} SW_{acc}$  trends.

Cloud fraction alone does not, however, explain all of the differences between  $TOA_{all}$  and  $SFC_{clr} SW_{acc}$  in Fig. 3.10. Mean CF over 2001-2018 has no impact on the ratio between  $TTE_{all}$  and  $TTE_{clr}$ , noise or autocorrelation during the time period (not shown). Furthermore, the radiative impacts of clouds also depend on the microphysical properties. In particular cloud phase can have a substantial impact on SW radiative forcing (Cesana et al., 2012, McIlhatten et al., 2017). We suspect discrepancies in cloud phase between models could further explain differences in noise between  $TOA_{all}$  and  $SFC_{clr} SW_{acc}$  given that such differences in cloud phase have explained past biases in model SW cloud radiative forcing in the Arctic (Gorodetskaya et al., 2008) and can further impact the global mean cloud feedback (Zelinka et al., 2020). While relevant, a detailed analysis linking cloud phase and differences in  $TOA_{all}$  and  $SFC_{clr} SW_{acc}$  would require data with higher temporal resolution than is currently available through CMIP6 for all but a few of the models used in this work.

#### 3.3.2.4 $SW_{acc}$ as a Proxy for Arctic and Global Change

As noted in the introduction, the amount of solar radiation absorbed in the Arctic,  $SW_{acc}$ , is a fundamental driver of Arctic climate. This relationship is shown more directly in Fig. 3.11a that quantifies the relationship between  $TTE_{all}$  and Arctic warming over the 21st

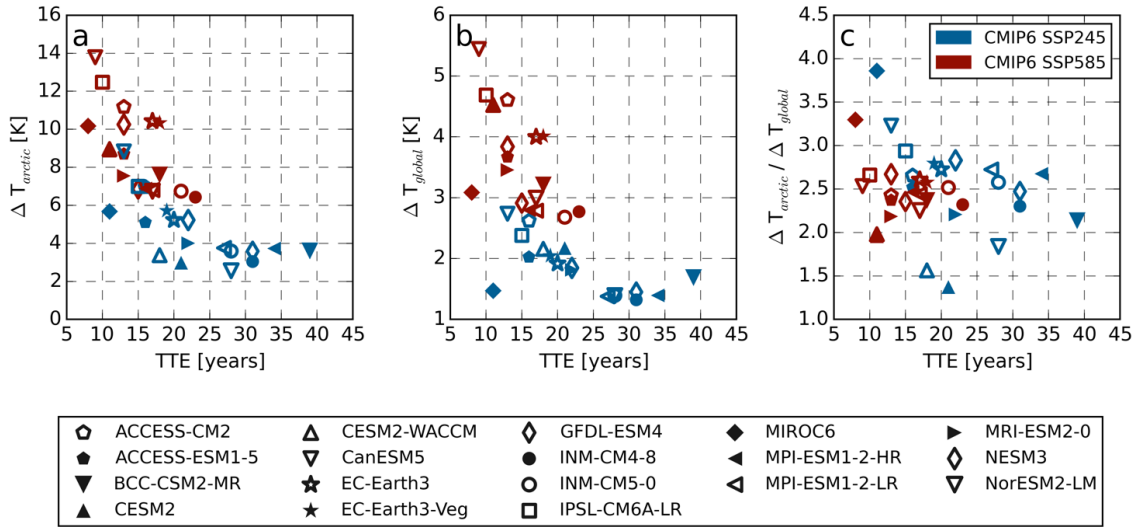


FIGURE 3.11: Relationships between (a) Arctic warming, (b) global warming, and (c) Arctic amplification (AA) and  $TOA_{all}$  TTE from CMIP6. Temperature changes ( $\Delta T$ ) are derived from the difference in annual average surface temperature of 2081-2100 relative to 2001-2018. The time to emergence of all-sky absorbed SW radiation trends in the Arctic may be a good proxy for both Arctic and global temperature change in both warming pathways. Since sea ice loss drives much of the inter-model variability of TTE, models with more warming have quicker sea ice loss and lower TTE, as seen in (a). A similar relationship appears to hold for global temperature (b) but not AA (c).

century in the CMIP6 models. While the calculation of  $TTE_{all}$  is independent of temperature trends, Figure 3.11a shows that it is strongly correlated with the projected change in annual average surface temperature in Arctic ( $\Delta T$ ; defined as the difference between 2081-2100 relative to 2001-2018). This demonstrates very clearly that there is a connection between greater Arctic warming, increasing  $SW_{acc}$ , and increased sea ice loss. Models with stronger ice-albedo feedbacks have warmer oceans that promote more rapid sea ice melt, stronger increases in  $SW_{acc}$  (i.e. shorter TTE), and, in turn, more ocean warming. Yet while  $TTE_{all}$  appears related to both Arctic and global warming, it has essentially no relationship to Arctic amplification (AA), the relative magnitude of Arctic warming to global warming. In Fig. 3.11c a wide range of  $TTE_{all}$  (10-40 years) cluster near AA values around 2.5.

While this analysis does not reveal the precise nature of these processes or their timing (i.e. cause and effect), it suggests that  $TTE_{all}$  could be a useful proxy for Arctic climate change for which we have a growing observational record. In addition,  $TTE_{all}$  may be a good predictor of global temperature changes over the 21st century, particularly for the "business as usual" pathway, SSP585 (Fig. 3.11b). Changes in global mean surface temperature from 2001-2018 to 2081-2100 decrease sharply with increasing TTE. This relationship suggests that the strength of Arctic  $SW_{acc}$  trends, relative to interannual variability, may be a good observation-based proxy for both Arctic and global temperature change but not AA.

### 3.3.3 Conclusions

This work evaluates forced and natural variations in Arctic absorbed shortwave radiation in observations and GCMs to establish the time to emergence of trends and how they are influenced by clouds. We find that the observed trend in clear-sky  $SW_{acc}$  at the surface is significant at the 95% confidence level using only 18 years of satellite observations. Clouds reduce the  $SW_{acc}$  trend measured in observations by at least half at the TOA resulting in the conclusion that the current observational record is insufficient to confirm any forced trend in  $SW_{acc}$  relative to interannual variability.

The 18 CMIP6 models analyzed in this study exhibit large inter-model spread in both forced trends and internal variability:  $SW_{acc}$  trends vary by an order of magnitude and natural variability varies by up to a factor of four. CMIP6 models further disagree on the effect of clouds on trends in  $SW_{acc}$ . While some predict that clouds increase TTE, consistent with observations, many fail to reproduce this fundamental feature in the CERES-EBAF record (Figure

3.1), possibly as a result of cloud feedbacks that artificially augment the SNR of surface albedo signatures at the TOA. The magnitude of TTE is largely driven by the decline of sea ice in models, as the statistical behavior of SIA largely determines those of  $SW_{acc}$  both with and without clouds. Trends in GCM cloud cover over the 21st century dictate whether or not clouds increase or decrease the time needed to detect a trend in  $SW_{acc}$ . Models that predict decreasing CF with Arctic warming predict stronger  $TOA_{all} SW_{acc}$  trends and shorter  $TTE_{all}$  than without clouds, but further work is needed to assess the role of cloud microphysical properties and phase in modulating  $SW_{acc}$  trends in the Arctic.

Accumulated SW radiation is linked to both Arctic and global temperature changes and shows potential as an observational metric of future Arctic climate change impacts. The results presented here suggest that the trend in  $TOA_{all} SW_{acc}$  may emerge from interannual variability in the next decade. Thus the extended observation record provided by continued CERES measurements and the planned Earth Radiation Budget continuity mission, Libera, will hopefully be of sufficient duration to determine the  $TOA_{all}$  trend. In turn this would allow the identification of climate models that best capture the processes that govern this fundamental measure of Arctic climate. Deeper investigation into the sea ice and cloud trends in these models may improve understanding of these key drivers of Arctic climate and, possibly, provide a constraint on anticipated global temperature change.

### 3.4 A closer look at observations of the "New Arctic"

In this section we use the same frameworks just discussed,  $SW_{acc}$  and TTE, but focus on spatial patterns in latest two decades of CERES observations (2000-2019). Unlike the previous section,  $SW_{acc}$  is only calculated at the TOA for clear and all-sky fluxes at latitudes north of  $60^\circ\text{N}$ . We investigate the spatial patterns of  $SW_{acc}$  in the Arctic by calculating it for each grid box  $i, j$ , without multiplying by area, so that maps of  $SW_{acc}$  show units of  $\text{MJm}^{-2}$ :

$$SW_{acc,i,j} = \sum_{m=3}^9 (SW^\downarrow - SW^\uparrow)_{i,j} \times t_m. \quad (3.4)$$

SIC in this section is from the NOAA/NSIDC Climate Data Record of Passive Microwave Sea Ice Concentration Version 3 that uses passive microwave radiometers, the Special Sensor Microwave Imager (SSM/I) and the Special Sensor Microwave Imager/Sounder (SSMIS), from the Defense Meteorological Satellite Program (DMSP) (Peng et al., 2013). SIC in this dataset is derived from a combination of the NASA Team and Bootstrap algorithms. We use SCF from version 6 of the MODIS/Terra Snow Cover Monthly dataset with 0.05 degree resolution of Climate Modeling Grid (CMG) cells, based on Normalized Difference Snow Index (NDSI) snow cover algorithm (Hall and Riggs, 2015).

Land and ocean are distinguished using the land fraction included in ArORIS based on the NCEP re-analysis land mask. NCEP land masks from ArORIS are also used to determine the individual land regions. Marginal seas are based on the Multisensor Analyzed Sea Ice Extent (MASIE) regions from the NSIDC interpolated to the ArORIS grid.

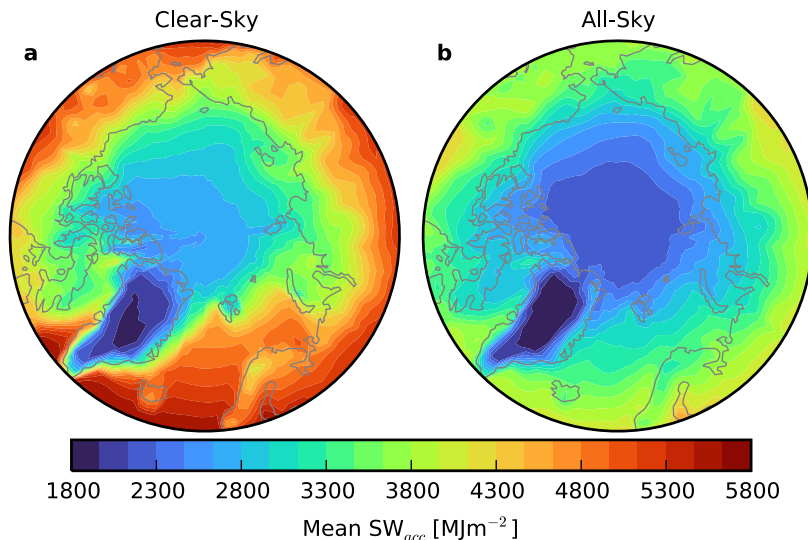


FIGURE 3.12: Mean accumulated SW ( $SW_{acc}$ ) over 2000-2019 from CERES-EBAF, calculated with top of the atmosphere clear-sky (a) and all-sky (b) fluxes.

### 3.4.1 Results

The 2000-2019 average net SW radiation (downwelling SW minus upwelling SW) incident on the TOA from March through September, referred to as the accumulated SW ( $SW_{acc}$ ), is shown in Fig. 3.12. Corresponding average sea ice and snow cover for the same period and same months are shown in Fig. 3.13. Without clouds (Fig. 3.12a), regional differences in  $SW_{acc}$  largely reflect the mean coverage of sea ice and snow (Fig. 3.13a,b). The greatest  $SW_{acc}$ , up to  $5600 MJm^{-2}$ , occur over lower latitudes that receive more solar insolation and are consistently free of sea ice.  $SW_{acc}$  decreases moving poleward in part due to the increasing solar zenith angle, but a sharp transition is visible in the North Atlantic and around Greenland where sea ice is typically present for at least part of the year. Over the interior Arctic Ocean, mean  $SW_{acc}$  ranges from 2000 to  $4400 MJm^{-2}$ .

The lowest clear-sky  $SW_{acc}$  values are found over the central Greenland ice sheet where the

surface is glaciated and relatively bright throughout the year (Stroeve et al., 2013). Regions with high average snow cover on land during the melt season also have low  $SW_{acc}$ , including the Canadian Archipelago, western mountains in Norway and the northern coast of Russia. Overall, clear-sky  $SW_{acc}$  is similar to SW absorption at the surface (Letterly et al., 2018).

Clouds substantially reduce the magnitude of mean  $SW_{acc}$  and smooth its spatial heterogeneity (Fig. 3.12b). Mean all-sky  $SW_{acc}$  is below  $4600 \text{ MJm}^{-2}$  over the entire Arctic, 82% the maximum clear-sky  $SW_{acc}$ , and the range of mean all-sky  $SW_{acc}$  values across the Arctic is about half that of clear-sky  $SW_{acc}$ . While surfaces with high albedos, e.g. perennial sea ice in the central Arctic Ocean and the Greenland ice sheet, still have mean  $SW_{acc}$  lower than the rest of the Arctic, the contrast is substantially reduced relative to clear skies. Thus, while the clear-sky  $SW_{acc}$  illustrates how the Earth's surface interacts with solar energy in the absence of clouds; the all-sky  $SW_{acc}$  actually governs the solar energy input into the Arctic climate system.

The area-weighted sum of the  $SW_{acc}$  in Fig. 3.12 is the total solar energy input into the Arctic system. Given the key role energy imbalances have in driving Arctic climate change, there is considerable interest in whether  $SW_{acc}$  has systematically changed and where such changes have occurred. Figure 3.14 shows anomalies of  $SW_{acc}$  relative to the 2000-2019 mean for both all-sky (solid lines) and clear-sky (dashed lines) conditions over land (pink) and ocean (navy). While  $SW_{acc}$  depends on area, ocean and land cover nearly equal areas in the Arctic north of  $60^\circ$  (Fig. S1). Both clear-sky and all-sky  $SW_{acc}$  trends are greater over ocean than over land,  $8.0 \pm 3.0 \times 10^4 \text{ MJ/year}$  and  $3.4 \pm 1.4 \times 10^4 \text{ MJ/year}$ , respectively (top

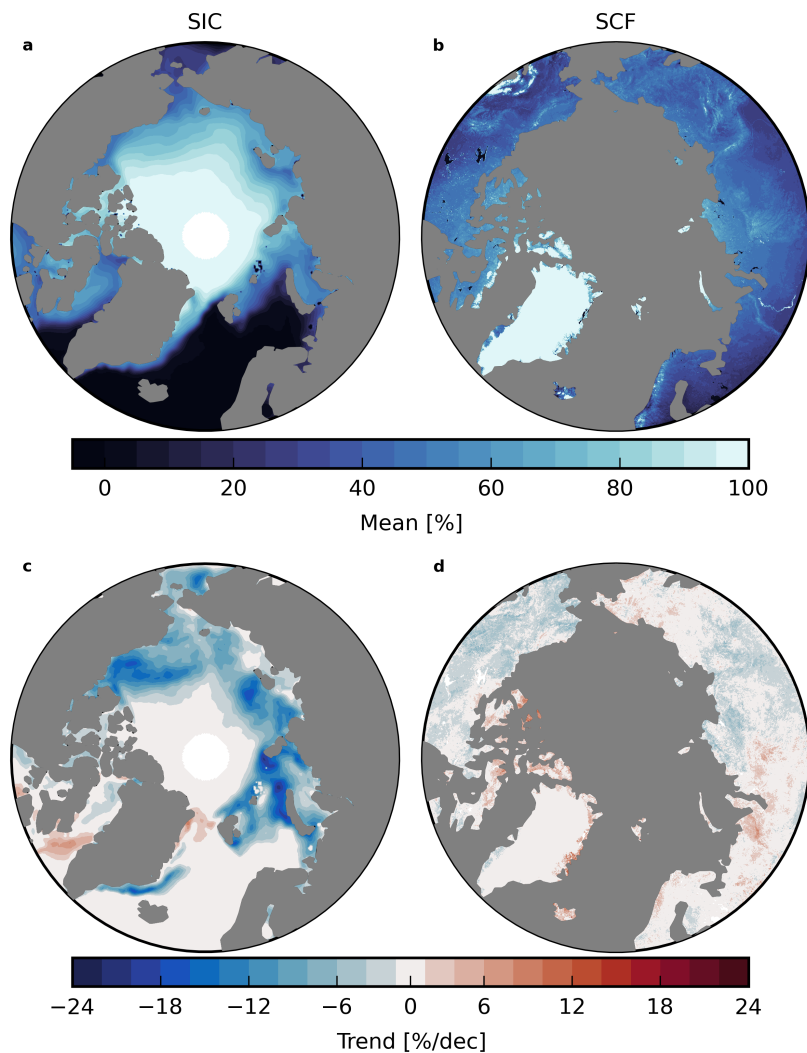


FIGURE 3.13: Average sea ice concentration (SIC) and snow cover fraction (SCF) for March through September from 2000-2019 (a,d) and corresponding trends (c,d). Trends are calculated using linear least-squares regression.

rows of Tables 3.5 and 3.6) confirming that reductions in sea ice are a stronger driver of surface  $SW_{acc}$  trends than snow cover on land (consistent with Letterly et al. (2018)). Large positive clear-sky  $SW_{acc}$  anomalies occur over the ocean for years with record-low September sea ice extent, e.g. 2007, 2012, 2016. All-sky  $SW_{acc}$  anomalies are clearly muted in 2012 and 2016 but are comparable to clear-sky anomalies in 2007 since cloud cover was anomalously low during the 2007 melt season (Kay et al., 2008). Over land, the largest  $SW_{acc}$

anomaly occurs in 2016 coinciding with the lowest spring northern hemisphere snow cover over the period analyzed.

Over both land and ocean, clouds dampen  $SW_{acc}$  trends and variability by more than a third and  $SW_{acc}$  standard deviations by almost 20%. Defining the signal-to-noise ratio (SNR) as the magnitude of the trend in  $SW_{acc}$  divided by its standard deviation, a measure of inter-annual variations; SNR quantifies the strength of secular trends relative to the underlying natural variability present in all climate records. Clouds decrease the SNR over both land and ocean since they reduce trends more than interannual variations. Since trends are more difficult to detect from noisier time series (Weatherhead et al., 1998), clouds effectively reduce the *detectability* of  $SW_{acc}$  trends. To quantify this effect, we estimate the expected number of years needed to detect a trend with 95% confidence, referred to as the time to emergence (TTE). Over the ocean, clouds increase the TTE by more than a third from  $11 \pm 3$  to  $16 \pm 4$  years. However, clouds have a negligible impact on TTE of  $SW_{acc}$  trends over land with trends emerging in 19 years under both all and clear-sky conditions, with standard deviations of 4 and 3 years, respectively. This consistency is due to the impact of autocorrelations on trend detection. Anomalies in clear-sky  $SW_{acc}$  tend to persist in time over land resembling trends. A longer record of observations is needed to discern such propagating natural variations from secular trends in the dataset. The opposite is true in all-sky  $SW_{acc}$  over land where negative autocorrelations exist: anomalies are more likely to be followed by an anomaly of the opposite sign, leading to the earlier emergence of a trend, all else being equal. These competing behaviors close the gap between clear-sky and all-sky TTE over land although the physical reasons for these autocorrelations are not entirely clear.

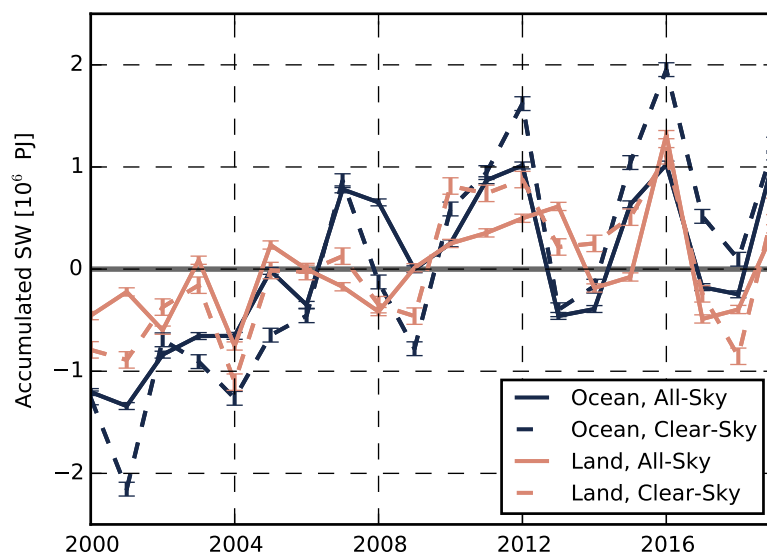


FIGURE 3.14: Anomalies of accumulated SW from CERES-EBAF over ocean (navy) and land (pink) areas in the Arctic under all and clear-sky conditions.

Furthermore, the sample size for measuring 1-lag autocorrelation here is relatively small and the corresponding uncertainties are not insignificant,  $\pm 0.44$ .

Taken together, the TTE of trends in total all-sky Arctic  $SW_{acc}$  is 16 years. This is a significant result: the sea ice and snow cover losses shown in Fig. 3.13c,d have now had a discernible impact on the amount of SW energy absorbed in the Arctic that emerged from natural variability in the last two decades of the CERES observational record. As a result the current 20-year observational record is now long enough to provide a robust test of predicted trends in this key driver of Arctic climate change in climate models despite conventional wisdom that a minimum of 30 years is needed to determine forced climate trends.

While the total accumulated SW absorption over the Arctic provides a useful measure of how ice and snow cover losses have influenced the energy balance of the Arctic system as a

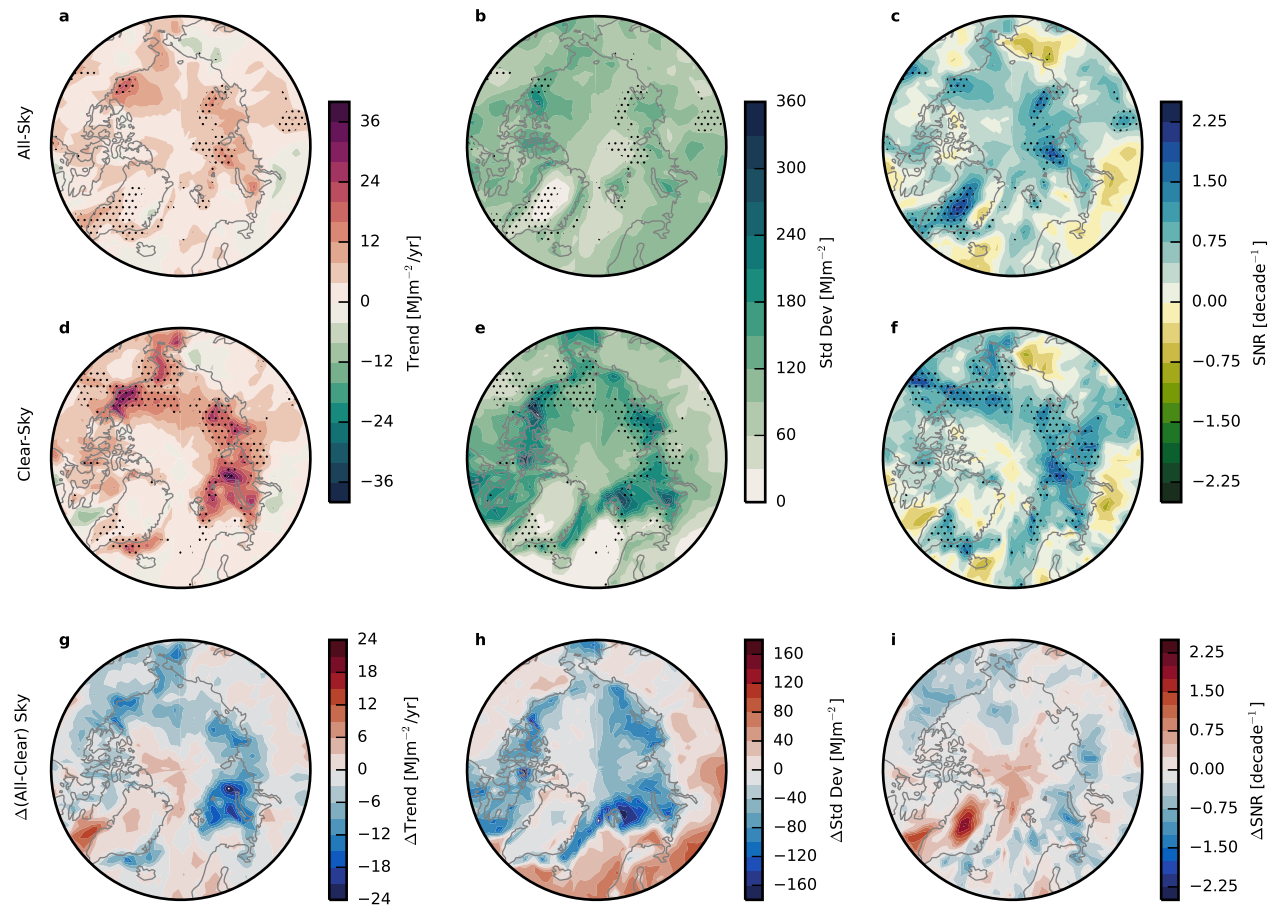


FIGURE 3.15: Accumulated SW trends (a,c), standard deviations (b,e) and signal to noise ratios (SNR) (c,f) calculated with all-sky (a-c) and clear-sky (d-f) fluxes from CERES-EBAF over 2000-2019. Differences between all-sky and clear-sky conditions are shown in (g-i). SNR is calculated by dividing the trend by the standard deviation. Stippling represents grid boxes where trends have emerged in the observational record with 95% confidence. Note that trends and standard deviations have units of  $\text{MJm}^{-2}$  since they have not been weighted by area.

whole, the impacts of changes in absorbed solar radiation are localized. In turn, increased solar absorption is in part responsible for increasing SST in locations of sea ice loss, e.g. Long and Perrie (2017), Timmermans et al. (2018). Recent declines in sea ice and snow cover exhibit distinct spatial patterns (Fig. 3.13c,d) that induce strong regional variations in the resulting  $\text{SW}_{acc}$  responses (Fig. 3.15).

The largest trends under clear-sky conditions correspond to areas with greatest sea ice loss over 2000-2019 (Fig. 3.13c), e.g. Barents, Kara, and Beaufort Seas. In these marginal seas, clear-sky  $SW_{acc}$  trends are on the order of 20-30  $MJm^{-2}/yr$ , but reach a maximum of 40  $MJm^{-2}/yr$  in the Kara Sea. Consistent with Fig. 3.14, trends are generally lower over land masses, with the greatest  $SW_{acc}$  trends observed over Northern Canada, approximately 20  $MJm^{-2}/yr$  without clouds. The few areas with negative  $SW_{acc}$  trends in Fig. 3.15 correspond to regions that have increasing sea ice (Labrador Sea) or snow cover (northeast and northwest coasts of Russia) (Fig. 3.13c). Regions without sea ice or snow cover during March through September, including much of the Atlantic Ocean, have negligible trends.

Clouds decrease the magnitude of  $SW_{acc}$  trends by roughly half over both land and ocean (Fig. 3.15g). Additionally, they reduce the total area of grid cells considered statistically significant by 33%. Clouds lower the trends around the Barents and Kara Seas by upwards of 15  $MJm^{-2}/year$ . Clouds also weaken the magnitude of  $SW_{acc}$  trend in the Labrador Sea, west of Greenland, where clear-sky  $SW_{acc}$  is decreasing because sea ice is increasing.

Large apparent trends over marginal seas do not, however, automatically guarantee rapid identification from natural variability since accumulated SW is also the most variable in these regions. Over regions with seasonal sea ice cover,  $SW_{acc}$  standard deviations reach upwards of 300  $MJm^{-2}$ , which are approximately twice as large as the variability over most land surfaces. The exception to this ocean-land contrast occurs over the Canadian Archipelago, that includes both snow and sea ice. Since regions with the largest trends also experience the largest variability, the SNR is critical for establishing the significance of trends relative

to natural variations. High SNR provides a good indication of where trends are statistically significant with 95% confidence, indicated with stippling in Fig. 3.15a-f.

In spite of their high year to year variability, the marginal seas exhibit large SNR under clear-sky conditions. Clouds not only reduce  $SW_{acc}$  over the ocean, they exert a strong influence on its variability, especially on regional scales. In fact, while clouds reduce variability overall in Fig. 3.14, two distinct regimes emerge in Fig. 3.15h: clouds decrease variability over areas with seasonal or perennial sea ice but increase variability over areas that typically remain ice free, namely the North Atlantic. Over ocean regions that experience seasonal ice loss, clouds reduce the variability of  $SW_{acc}$  by roughly half, upwards of  $150 \text{ MJm}^{-2}$  in the Barents Sea and Canadian Archipelago. When present, clouds can increase the albedo over open ocean, but they also increase  $SW_{acc}$  variability because they are transient while open ocean has low and consistent albedo by comparison. Clouds therefore increase the standard deviation of  $SW_{acc}$  by on the order of  $+75 \text{ MJm}^{-2}$  relative to clear skies over open ocean. On the other hand, clouds have the opposite effect over sea ice edges. While clouds are not always present, they persist in time for sufficiently long periods to dampen the albedo contrast between sea ice and open ocean, in turn reducing  $SW_{acc}$  variability.

As a result of these spatial variations, integrating  $SW_{acc}$  over all land and ocean areas conceals large regional differences in SNR and the time to emergence of trends in absorbed shortwave radiation that may have important local implications. Across individual marginal seas, for example,  $SW_{acc}$  trends vary by a factor of two without clouds and a factor of three with clouds, Tables 3.5 and 3.6. Over most marginal seas, all-sky trends are roughly half

TABLE 3.5: Characteristics of all-sky accumulated shortwave radiation over the Arctic domains defined in Figure S1. The TTE is the mean number of years needed for a trend emerge from 300 synthetic time series based on the trend, standard deviation and autocorrelations. The standard deviation of TTE from the synthetic ensemble is given in parentheses. Trends that have emerged in the current observational record, are noted with asterisks. Regions are noted with a <sup>+</sup> if all-sky and clear-sky mean TTE are statistically different using a students t-test with  $p < 0.05$ .

Region	Trend [10 <sup>3</sup> PJ/yr]	Std Dev [10 <sup>4</sup> PJ]	SNR [dec <sup>-1</sup> ]	Autocor	TTE [yr]
All Arctic <sup>+</sup>	113	86.2	1.3	0.10	16 (4)*
All Ocean <sup>+</sup>	79.9	57.8	1.4	0.28	16 (4)*
All Land	33.6	43.8	0.77	-0.21	19 (6)*
Barents Sea <sup>+</sup>	4.6	8.2	0.57	-0.11	25 (7)
Kara Sea <sup>+</sup>	9.78	8.01	1.22	0.23	18 (4)*
Laptev Sea <sup>+</sup>	7.51	8.26	0.91	-0.03	19 (5)*
East Siberian Sea <sup>+</sup>	4.72	6.73	0.70	-0.07	21 (6)
Chukchi Sea <sup>+</sup>	6.58	8.35	0.79	0.02	21 (6)
Beaufort Sea <sup>+</sup>	11.74	13.45	0.87	0.26	23 (5)
Greenland Sea <sup>+</sup>	4.62	8.34	0.55	-0.14	24 (7)
Central Arctic Ocean <sup>+</sup>	13.99	17.17	0.81	0.22	23 (5)
Europe <sup>+</sup>	-1.92	17.70	-0.11	-0.52	56 (19)
N.America <sup>+</sup>	14.45	16.96	0.85	-0.23	17 (5)*
Greenland	9.90	11.25	0.88	-0.03	19 (6)*
Siberia <sup>+</sup>	11.44	24.85	0.46	-0.26	26 (8)
Eurasia <sup>+</sup>	9.28	36.96	0.25	-0.44	35 (11)

of their clear-sky counterparts. The only exception is the Barents Sea where the all-sky trend is about a quarter of that in clear-skies trend because of persistent cloud cover Liu et al. (2012). The impact of clouds is less consistent over distinct land regions.  $SW_{acc}$  trends over North America, Siberia and Eurasia are diminished by clouds, but the  $SW_{acc}$  trend is actually increased by clouds over Greenland where cloud cover and snow cover have decreased in concert along the northeast edge of the ice sheet Hofer et al. (2017).  $SW_{acc}$  trends over northern Europe are negligible regardless of cloud cover despite significant declines

TABLE 3.6: As in Table 3.5 but for clear-sky  $SW_{acc}$ .

Region	Trend [ $10^3$ PJ/yr]	Std Dev [ $10^4$ PJ]	SNR [dec $^{-1}$ ]	Autocor	TTE [yr]
All Arctic <sup>+</sup>	192	116	1.6	0.10	14 (4)*
All Ocean <sup>+</sup>	134.8	69.9	1.9	0.04	11 (3)*
All Land	57.0	53.5	1.1	0.17	19 (4)*
Barents Sea <sup>+</sup>	17.4	13.2	1.32	0.24	17 (4)*
Kara Sea <sup>+</sup>	19.87	13.18	1.51	0.34	17 (3)*
Laptev Sea <sup>+</sup>	14.66	13.06	1.12	-0.24	14 (5)*
East Siberian Sea <sup>+</sup>	9.05	11.24	0.81	-0.2	18 (6)*
Chukchi Sea <sup>+</sup>	13.48	8.97	1.50	-0.14	12 (4)*
Beaufort Sea <sup>+</sup>	17.85	16.22	1.10	0.03	17 (4)*
Greenland Sea <sup>+</sup>	9.01	9.08	0.99	0.04	18 (5)*
Central Arctic Ocean <sup>+</sup>	14.73	20.80	0.71	0.2	26 (6)
Europe <sup>+</sup>	0.28	11.74	0.02	0.08	224 (50)
N.America <sup>+</sup>	30.18	24.92	1.21	-0.19	14 (4)*
Greenland	6.56	10.99	0.60	-0.37	20 (7)*
Siberia <sup>+</sup>	17.13	21.64	0.79	0.22	23 (5)
Eurasia <sup>+</sup>	16.72	28.98	0.58	0.19	28 (6)

in snow cover (Fig. 3.13d) possibly owing to the relatively high reflectance of the underlying tundra. Regional differences are also evident how cloud influence SNR. Clouds reduce SNR over the Barents, Chukchi, and Greenland Seas as well as over Siberia and Eurasia, while the impact is smaller or even reversed over other regions.

Over the much of the Arctic Ocean, the primary impact of clouds on absorbed solar radiation is to lower the SNR and, in turn, increase the time needed to detect trends. Clear-sky  $SW_{acc}$  trends have emerged in the CERES-EBAF record over all marginal seas, listed in Tables 3.5 and 3.6, but clouds have masked those trends from being statistically significant for two thirds of the marginal seas (Barents, East Siberian, Chukchi, Beaufort, Greenland, Central Arctic). Trends in the Laptev and Kara Seas are statistically significant with 18-19

( $\pm 4$ -5) years of observations, a relatively short time period. However, in the Barents Sea where sea ice trends are large, ubiquitous cloud cover reduces the local  $SW_{acc}$  trends much more than the interannual variability, decreasing the SNR (Fig. 3.15g-i) and substantially increasing the TTE (Tables 3.5 and 3.6). Based on the measured trends and corresponding variability, clouds are also expected to delay the time needed to detect trends in the East Siberian Sea and Chukchi Sea by three and nine years, respectively, enough to mask trends that would otherwise have been detectable in the current satellite record. Clouds have little effect on the estimated time required to detect  $SW_{acc}$  trends in the central Arctic Ocean where perennial sea ice persists (Fig. 3.15) and clear sky trends have not yet emerged. However, if observed changes from the past two decades in the central Arctic Ocean persist into the future, clouds may accelerate the detection of  $SW_{acc}$  trends, although this result is highly uncertain.

There are also two distinct regions of cloud impacts on absorbed solar radiation over land. Clouds impact North America in a similar manner as over the marginal seas, reducing  $SW_{acc}$  SNR and increasing the TTE. Based on Fig. 3.15g, clouds decrease  $SW_{acc}$  trends over continental North America but do not substantially impact their variability. From June through September most land surfaces contribute little to the TOA albedo (Sledd and L'Ecuyer, 2019), so the transient nature of clouds can again provide intermittent contrast to the relatively dark surface albedo. However, while clouds have increased TTE over North America by several years, all-sky  $SW_{acc}$  trends have still emerged in the existing satellite record. This is true along the coast of Eurasia as well, but  $SW_{acc}$  trends have not emerged over Europe, Siberia, or Eurasia.

Clouds have a distinctly opposite effect on  $SW_{acc}$  over the Greenland ice sheet that resembles their impact on the central Arctic Ocean. Accumulated SW trends increase slightly under all-sky conditions compared to clear-sky ( $+5 \text{ MJm}^{-2}/\text{year}$ ), and clouds slightly decrease  $SW_{acc}$  variability. The net effect is that the SNR of  $SW_{acc}$  over Greenland actually increases with cloud cover, and trends are significant under all-sky and clear-sky conditions. Recent studies suggest decreased cloud cover over the Greenland ice sheet, which could reduce the TOA albedo and lead to more SW absorption (Comiso and Hall, 2014, Hofer et al., 2017). Some caution is required interpreting these results over Greenland, though, as biases in CERES-EBAF radiation have been documented over the Greenland ice sheet (Lenaerts et al., 2017).

### **3.4.2 Discussion and Conclusions**

The 20 year CERES record is now long enough to have definitively measured recent increases in total all-sky absorbed shortwave radiation in the Arctic. While clouds generally act to reduce the magnitude of  $SW_{acc}$  trends, and increase the number of years required to measure a trend relative to a clear-sky scenario, sea ice and snow cover have declined sufficiently that their impacts on absorbed solar radiation have emerged in the two decade observational period, in both clear-sky and all-sky conditions. Although 20 years is a short observational period for trend detection, (Landrum and Holland, 2020) found that sea ice

has already declined so much in the satellite era that it is significantly different than pre-industrial conditions during this time period. However, even though sea ice largely determines the pan-arctic surface albedo, it was not obvious that such changes directly manifest themselves in the TOA energy budget due to the substantial influences of intervening clouds. This work demonstrates that the solar energy input into the Arctic has definitively increased as a result of these sea ice losses over the modern satellite era.

Clouds have, however, masked  $SW_{acc}$  trends from emerging over most of the marginal seas individually, except for the Kara and Laptev Seas. Clouds uniformly decrease  $SW_{acc}$  trends over surfaces with declining surface albedo due to snow and sea ice loss, but, clouds' influences on interannual variability fall into two distinct regimes. Clouds decrease variability where the surface changes during the melt season, such as the marginal ice zone, but they increase variability wherever the surface has a consistent albedo, such as open ocean in North Atlantic.

Clouds have comparatively little influence on the detection of  $SW_{acc}$  trends over Arctic land as a whole with increases emerging in the last year of the current CERES record. Yet, clouds have masked increased solar absorption in all individual land domains studied, except North America which exhibits the strongest trends and more modest interannual variability. These results suggest that the emergence of trends in solar absorption by Arctic land regions has been driven by snow cover changes in North America.

These findings generally agree with previous work. Hartmann and Ceppi (2014) also found large trends in the Beaufort Sea and Canadian Archipelago using all-sky TOA fluxes. In

comparison, Wu et al. (2020) found lower trends in June, August and September over marginal seas in the Arctic. Perovich et al. (2007) observed the largest trends in the Pacific sector, from the East Siberian Sea into the Beaufort Sea, and Letterly et al. (2018) found this same region to have strong trends in June and September. We found lower trends in most of the Pacific sector, except for the Beaufort Sea. Our work shows greater trends in the Kara and Laptev Seas compared to Perovich et al. (2007), but agree with Letterly et al. (2018) during the spring and early summer, which are months with significant incoming SW. While earlier work found clouds had small impact on SNR when calculated using the entire Arctic, we expose a more nuanced picture. As in Sledd and L'Ecuyer (2021), clouds reduce the magnitude of trends even on regional and local scales, but we find that clouds have varied impacts on  $SW_{acc}$  variability, either increasing it over consistently dark open ocean or decreasing it over the marginal ice zone. This suggests pan-arctic studies may inadvertently miss important regional differences that are critical for defining local surface and temperature responses.

Because clouds account for the majority of the TOA albedo in the Arctic (Sledd and L'Ecuyer, 2019), any changes in cloud cover impact SW absorption. Earlier studies found positive trends in spring and summer from APP-x over 1982-2000 (Wang and Key, 2005), and from AVHRR, cloud cover over the Arctic is slightly declining over 1981-2012, but the trends are small during summer while the variability is high (Comiso and Hall, 2014). Using cloud variables available in CERES Edition 4.0, Choi et al. (2020) found no significant trend in cloud fraction. However, passive sensors underestimate cloud fraction, on the order of 10% in spring and summer compared to active sensors, e.g. CloudSat and CALIPSO (Chan and

Comiso, 2013). Using such active sensors, no statistically significant trend in Arctic cloud cover has been determined (Kay et al., 2016), but the length of this satellite record is still quite short, beginning in late 2006. Ultimately, longer data records are needed to determine how cloud cover is changing in the Arctic.

Of the regions where trends have not yet emerged, many are predicted to emerge in the next decade. The continuation and continuity of satellite measurements over the Arctic will be critical for determining if and when such trends emerge and to continue monitoring the impacts of climate change in the Arctic. The Libera mission will be key to maintaining this consistent record.

## **Chapter 4**

# **Connections between Arctic TOA albedo and SW trends in CMIP6**

### **4.1 Preface**

Previously we found that the atmosphere, namely clouds, are responsible for at least two thirds of the planetary albedo over the Arctic, depending on the month, despite highly reflective surfaces being present. Our findings also suggest that clouds dampen monthly variability in the planetary albedo. On interannual time scales, clouds reduce the magnitude of SW absorbed over the melt season, the magnitude of accumulated SW trends, and the detectability of those SW trends. Clearly, the TOA albedo impacts SW accumulation. In

---

\*This chapter is part of a manuscript being prepared for submission with coauthor T. S. L'Ecuyer.

this section we explicitly connect those ideas by documenting what the albedos and TOA albedo partitions look like in CMIP6 models, both the mean states under historical forcing as well as broad changes under SSP585. The relationships between albedos and sea ice area (SIA) are then explored and connected to  $SW_{acc}$  TTE to highlight the range of behaviors present in CMIP6. Finally, we end by relating all-sky  $SW_{acc}$  ( $SW_{all}$ ) TTE to broader model behavior. Comparisons to observations are included where appropriate.

## 4.2 Methods

This chapter uses observations from CERES-EBAF and NSIDC as well as output from CMIP6 SSP585, as described in Chapter 3.

This chapter also uses methods from the previous chapters, both TOA albedo partitioning (Chapter 2) and  $SW_{acc}$  TTE (Chapter 3). Following the second analysis in Chapter 3, we calculate  $SW_{acc}$  at the TOA for clear-sky and all-sky conditions. We restrict the years used to calculate  $SW_{acc}$  1-lag autocorrelations and standard deviations to the overlap between the CMIP6 historical record and CERES-EBAF observational record, 2000-2015. This has a limited impact on TTE compared to the results in Chapter 3. Trends are still calculated over the 21<sup>st</sup> century, 2000-2100.

In addition to  $SW_{acc}$ , we also define an accumulated reflection variable.  $SW_{ref_{atm}}$  is the total SW energy that the atmosphere reflects during the melt season, similar to  $SW_{acc}$ :

$$SW_{ref_{atm}} = \sum_{m=3}^9 \sum_{i,j} (\alpha_{p_{atm}} SW^\downarrow)_{i,j} \times A_{i,j} \times t_m, \quad (4.1)$$

where  $\alpha_{p_{atm}}$  is again the atmospheric contribution to the TOA albedo,  $SW^\downarrow$  is the incoming SW at the TOA,  $A_{i,j}$  is the area in gridbox  $i, j$ , and  $t_m$  is the number of seconds in month  $m$ .  $SW_{ref_{atm}}$  helps connect our analysis between the monthly albedo partitioning and seasonal  $SW_{acc}$  TTE frameworks.

## 4.3 Results and Discussion

### 4.3.1 CMIP6 albedo partitioning mean state

Across this CMIP6 ensemble, models have broad agreement on the seasonal cycle and relative magnitudes of TOA and surface albedos and TOA albedo contributions. Figure 4.1 shows monthly albedos and contributions averaged over 2000-2015. Observations (solid red line) fall within the model ensemble for each variable over the melt season, the one exception being the TOA albedo in March (Fig. 4.1a). The surface albedo has the greatest range between models in late summer, 0.16 in September. However, the actual surface contribution to the TOA albedo has a narrow range in late summer,  $<0.05$ , since all models agree that the surface adds little to the planetary albedo at this point in the year. Its largest range is during spring, but the spread is less than 0.10. The atmospheric contribution always has a greater range than the surface contribution, up to 0.13 in July and August. Model differences in the TOA albedo contributions have some compensating behavior, though, since the TOA albedo has a slightly narrower range across models than

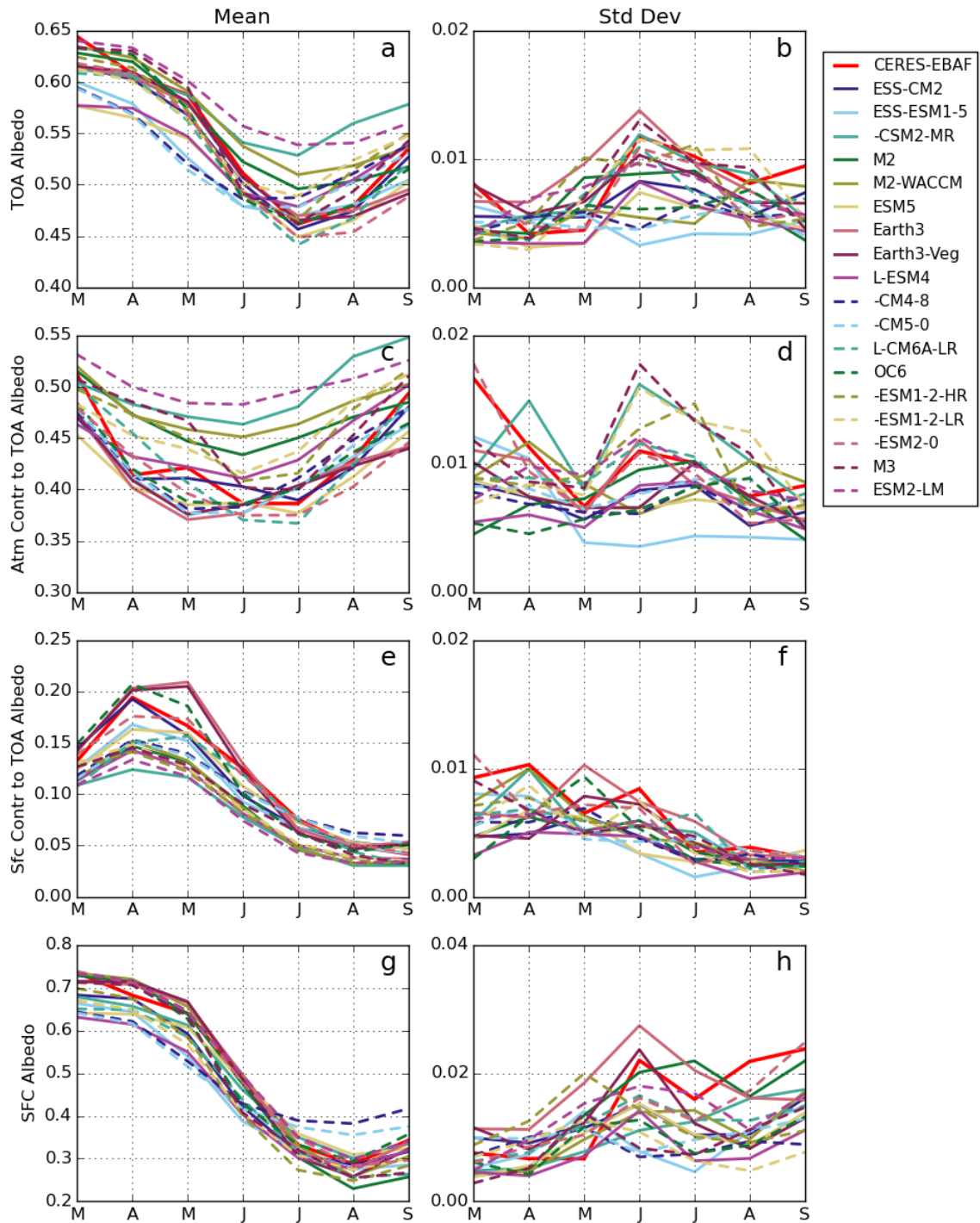


FIGURE 4.1: Monthly means (left column) and standard deviations (right column) of TOA and surface albedos and TOA albedo partitions in CMIP6 during the melt season, March through September. Values are calculated from historical forcing years 1900-2015 and averaged over the area north of the Arctic Circle.

atmospheric contribution, at most 0.11 in August.

While this ensemble does reasonably well capturing the mean behavior of albedo partitioning in the Arctic, some models do show unique behaviors. INM-CM5-0 and INM-CM4-8 (dashed light and dark blue lines in Fig. 4.1) have the lowest amplitude change in the surface albedo cycle, with relatively low surface albedo in spring but high values in late summer. This behavior is largely due to the cycles of sea ice area (not shown). INM-CM5-0 and INM-CM4-8 also have the low TOA albedo means in spring and smaller differences between their minima and maxima (Fig. 4.1a). This is due not only to the low surface albedo, but also the low atmospheric contribution (Fig. 4.1b). NESM3 (dashed dark purple) displays the opposite behavior, with larger albedo differences during the melt season. The atmospheric contribution in particular has an unusually sharp decline between early spring and later summer (Fig. 4.1c; 0.06 drop from May to June). The large amount of sea ice and snow cover in EC-Earth3 and EC-Earth3-Veg (solid rose and dark purple) lead to higher surface albedos and surface contributions in spring, although this is compensated by a lower than average atmospheric contribution to give a moderate TOA albedo. This is all to say that "broad agreement" only extends so far.

In addition to the raw value of the atmosphere and surface contributions, it is also instructive to calculate the percentage the surface and atmosphere each account for in the TOA albedo, found by dividing each contribution by the TOA albedo before averaging over the Arctic. In Fig. 4.1 the surface and atmospheric contributions sum to the TOA albedo, while in Fig. 4.2 the values sum to 1. Before, we observed that the atmospheric contribution was

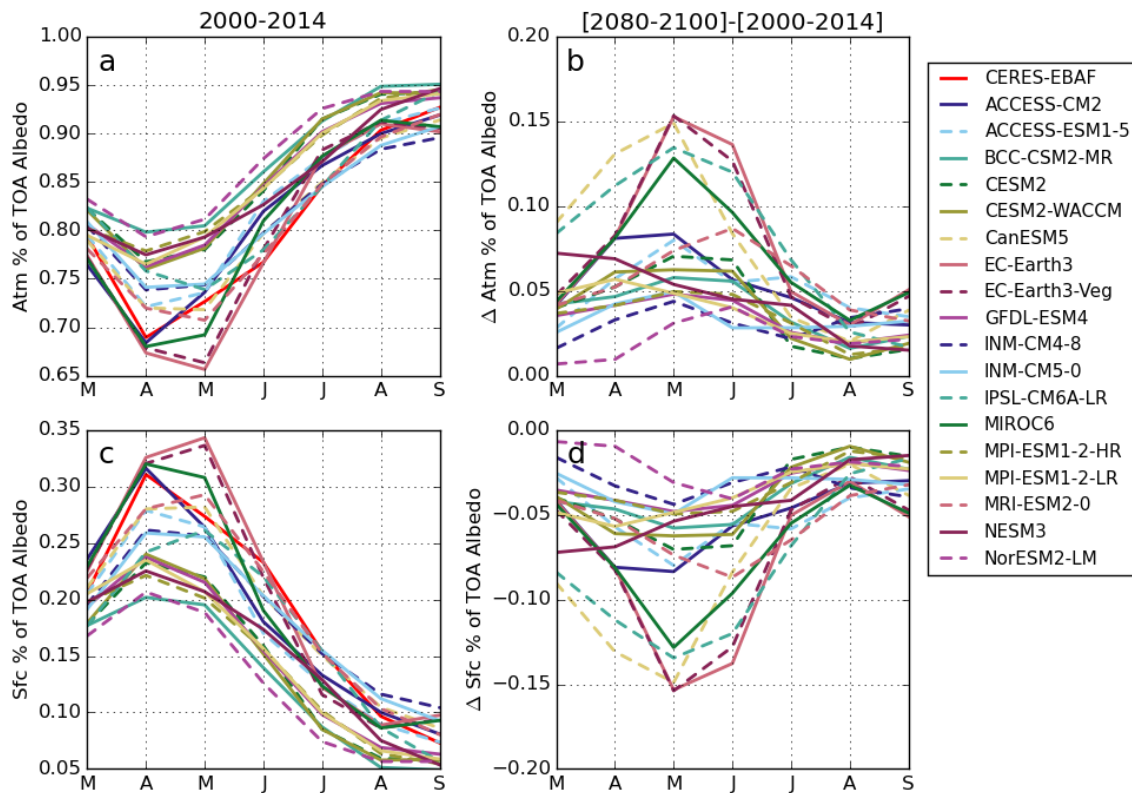


FIGURE 4.2: Fraction of the TOA albedo contributed by the atmosphere (a) and surface (c) over 2000-2015 in CMIP6 and observations (CERES-EBAF), March through September. Differences between historical and end of century (2080-2100) fractional TOA contributions are shown in (b) and (d), calculated with SSP585.

larger than the surface contribution throughout the melt season, and in Fig. 4.2a we now see that on average the atmosphere accounts for at least 65% of the TOA albedo in late spring and up to almost 95% of the TOA albedo by the end of summer. In observations the atmosphere contributes on average about 70% of the TOA albedo in April and over 90% in September. Thus, the surface accounts for a relatively small percent of the TOA albedo. For some models, e.g. NESM3 and BCC-CSM3-MR, the surface accounts for about 20% of the TOA albedo at most (Fig. 4.2c). Models show an approximately 15% range in spring, but the spread decreases in late summer as all models show the atmosphere dominating the TOA albedo. Compared to observations, many models may actually be overestimating the

mean contribution from the atmosphere. Correct surface albedo, namely sea ice, is critical for the surface energy balance, but models also need to correctly represent the intervening atmosphere to accurately model the TOA energy balance.

We also find that the atmosphere grows more important with rising greenhouse gas concentrations. Figures 4.2b and d show changes in percent contributions from the atmosphere and surface over the 21st century. All models predict that the atmosphere contributes a larger percentage of the TOA albedo because sea ice and snow cover decline. Typically, models that show the surface contributing a higher percentage of the TOA albedo experience greater changes with higher greenhouse gases, e.g. EC-Earth3 and EC-Earth3-Veg (solid rose and dark purple). Some of the largest changes occur in spring, up to 15% in May, even though sea ice declines the most in late summer and fall. By late summer the surface contributes so little that there is not much room for further decline.

### **4.3.2 Sea ice and SW albedos**

There is broad consensus across CMIP6 that the surface albedo is highly correlated with SIA over the historical period (Fig. 4.3a). In June (yellow markers) correlations are all greater than 0.7, and in August and September (blue and black) correlations are above 0.9 for all models. This agreement makes physical sense as less bright sea ice means more dark open ocean. That agreement does not extend to the TOA, though. In Fig. 4.3a, correlations between the TOA albedo and SIA range from below 0.3 to above 0.8 in June through September (y-axis range). This spread means that in some models the TOA albedo is strongly linked

to the surface and sea ice (EC-Earth3, EC-Earth3-Veg, MRI-ESM2-0), while in other models the response is relatively weak (MPI-ESM1-2-HR, MPI-ESM1-2-LR, BCC-CSM2-MR). Apparently in those models, what happens at the surface stays at the surface.

The surface and atmospheric contributions to the TOA albedo both exhibit large spreads in their correlations to SIA. The surface contribution correlations with SIA range from about 0.2 to 0.9 (Fig. 4.3b), and the atmospheric contribution ranges from -0.1 to 0.6 (Fig. 4.3c), although correlations with magnitudes less than 0.18 are not statistically significant at the 95% confidence level (shaded region in Fig. 4.3c). The largest correlations between surface contributions and SIA are associated with strong TOA albedo correlations, but below  $\sim 0.8$  there is a fair amount of spread in Fig. 4.3b. Some correlation with SIA from the atmospheric contribution is also needed for high SIA-TOA albedo correlations. For example, in September BCC-CSM2-MR (●) has a significant correlation between the surface contribution and SIA (0.7), but the atmospheric contribution has essentially no correlation to SIA ( $\sim -0.1$ ). This leads to its TOA albedo correlation to SIA being one of the lowest in this ensemble (0.3). The requirement for an atmospheric response to SIA changes in order for the TOA albedo to also respond is consistent with the fact that the atmosphere contributes a large percentage of the TOA albedo (4.2).

However, correlations cannot tell us the magnitude of how the TOA albedo responds to SIA. For that we turn to the sensitivity of TOA and surface albedo to changes in sea ice area, found by regressing albedos against SIA for each month from June through September over 1900-2014 (Figure 4.4a) and 2000-2014 (Figure 4.4b). In all models, the surface

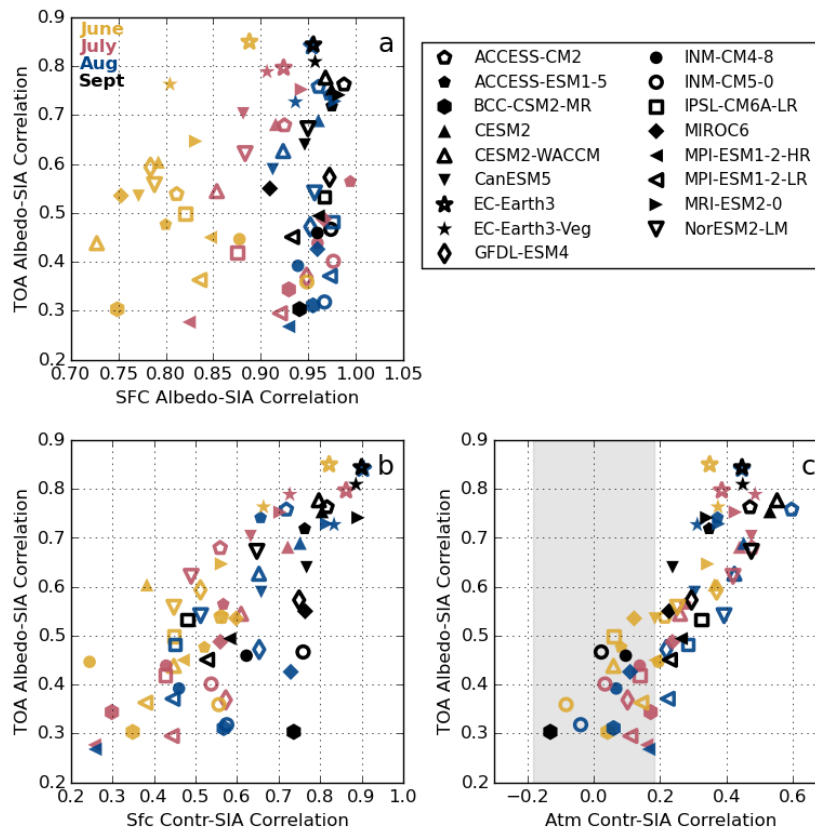


FIGURE 4.3: Correlations between albedos and SIA as they relate to each other during summer months. Correlation coefficients are calculated over the historical period, 1900-2015, using detrended anomalies. Correlation coefficients with magnitudes greater than 0.18 are considered statistically significant using a t-test with 95% significance level; shading in c) indicates statistically insignificant correlations.

albedo is more sensitive to changes in SIA than the TOA albedo in summer and fall (transparent versus solid shading), consistent with observations (Sledd and L'Ecuyer, 2019). The magnitude of the TOA response to SIA changes is strongly related to the magnitude of the surface albedo response (Fig. 4.5a), though. Across models in the full historical period, the surface-SIA sensitivity differs by approximately a factor of two in June-September in Fig. 4.4a. Inter-model differences in surface albedo responses are likely due to the different representations of sea ice that impact its albedo. TOA and surface albedo sensitivities are positively related (Fig. 4.4a), particularly for June (yellow) and September (black). While

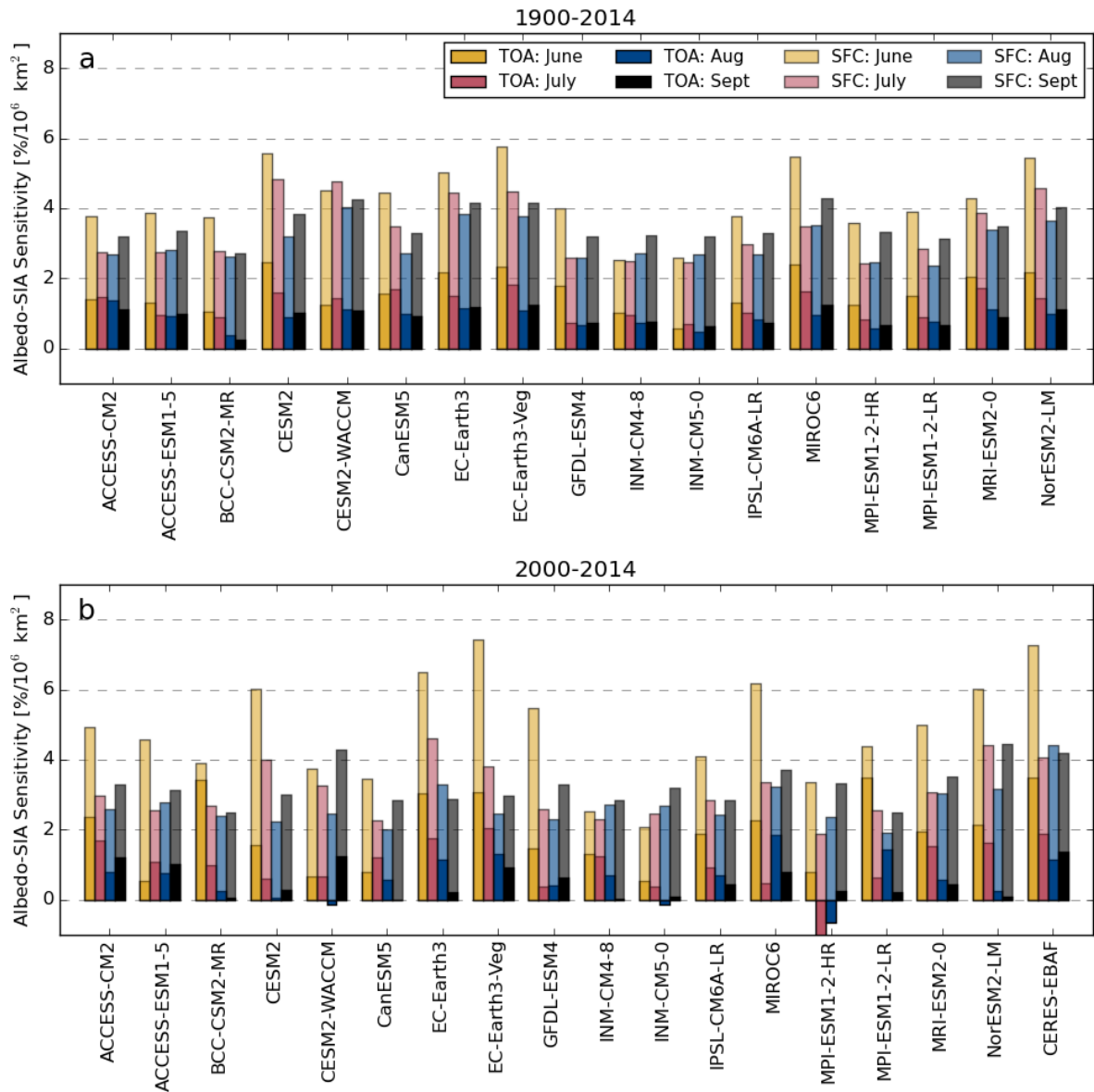


FIGURE 4.4: Sensitivity of TOA and surface albedos to sea ice area (SIA) in summer months. Sensitivity is found from the regression of each albedo against SIA for a given month across the historical time period, 1900-2015 (a) and the overlap with the CERES observational record, 2000-2015 (b).

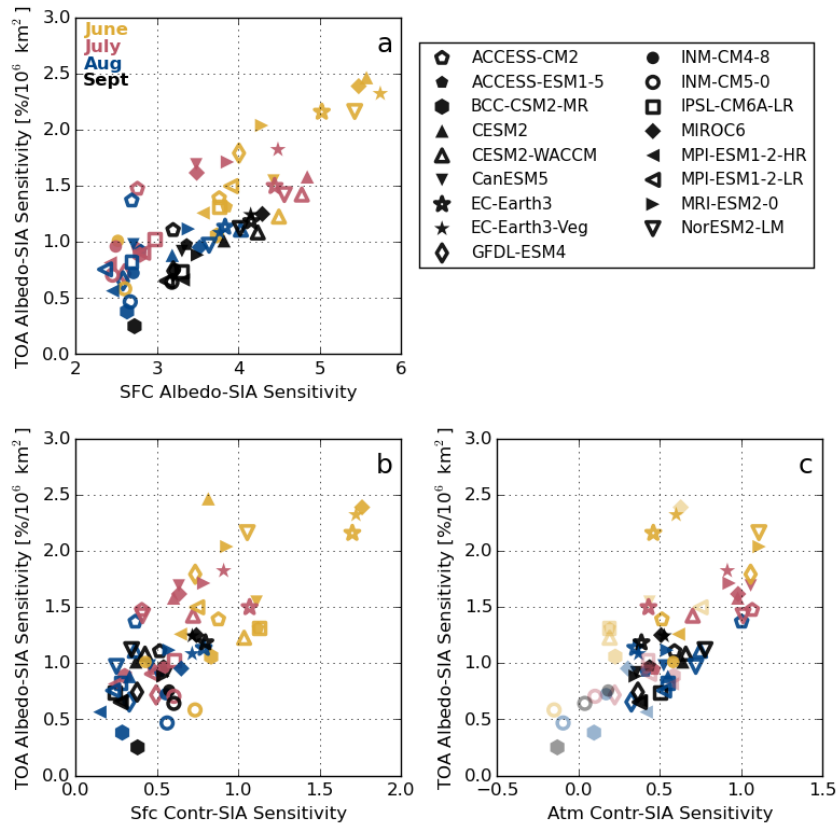


FIGURE 4.5: Regressions of TOA albedo sensitivity to SIA against the sensitivity to SIA of the surface albedo and TOA albedo partitions. Slopes that are statistically insignificant ( $p > 0.05$ ) are indicated by translucent shading, notably in c).

the TOA albedo is always less sensitive than the surface albedo in CMIP6, the sensitivities vary by a greater factor, up to 5x in September between BCC-CSM2-MR and EC-Earth3-Veg. For example, we can compare the responses of INM-CM5-0 and CESM2 in June, with TOA albedo sensitivities of approximately 0.5 and 2.5 %/10<sup>6</sup> km<sup>2</sup>, respectively. Assuming average incoming SW at the TOA of 500 Wm<sup>-2</sup>, if both models had one million km<sup>2</sup> less sea ice, all else being equal, the change in absorbed SW ( $\Delta SW_{absorbed} = -\Delta\alpha_{TOA} * SW_{\downarrow}$ ) would be 2.5 Wm<sup>-2</sup> in INM-CM5-0 and 12.5 Wm<sup>-2</sup> in CESM2, on average.

Observations also have significant sensitivities, but some caution is warranted when comparing them to CMIP6. Figure 4.4b shows sensitivities calculated over the historical overlap with CERES observations, 2000-2014. From CERES, albedo sensitivities are highest in June at the surface and TOA, then stay lower through the end of the summer. Observational sensitivities of both surface and TOA albedos are greater than most CMIP6 values. However, CMIP6 albedos are often less sensitive to SIA over 2000-2014 compared to the full historical record. A few models even display negative relationships between TOA albedos and SIA, e.g. CESM2-WACCM, INM-CM5-0, MPI-ESM1-2-HR. Across models, TOA sensitivity is unrelated between the time periods (not shown). The observational time period has fewer years, and therefore less SIA variability, than the full historical record.

We can further break down the sensitivity of the TOA albedo into the response of the atmosphere and surface. In our albedo partitioning framework, the TOA albedo is a sum of contributions from the surface and atmosphere, so we can quantify each of their relationships to SIA changes, shown in Fig. 4.5 for 1900-2014. The range of sensitivities across the CMIP6 ensemble decreases from June to September. All models have significant, if small, surface contribution sensitivity to SIA over the historical period (Fig. 4.5b). This makes sense because the surface contribution depends on the surface albedo. The atmospheric contribution is a different matter. Some models (EC-Earth3-Veg, IPSL-CM6A-LR, MRI-ESM2-0) do have statistically significant positive relationships between SIA and the atmospheric contributions (Fig. 4.5c). Most other models show noise. It is a clear difference in model behavior that SIA may or may not impact the magnitude of atmospheric contribution, though.

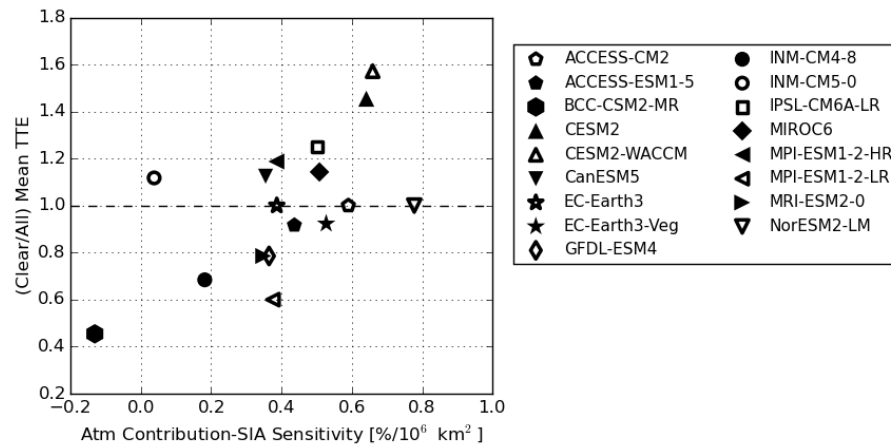


FIGURE 4.6: Sensitivity of TOA albedo to SIA as it relates to the ratio of all-sky to clear-sky  $SW_{acc}$  TTE in September calculated with SSP585.

### 4.3.3 SW albedos and trend detection

In Chapter 3 we found that clouds delay  $SW_{acc}$  TTE in observations but not in all models, and we speculated this had to do with predicted cloud changes or possible feedbacks that amplified surface albedo changes. Here we see that in models where the atmospheric contribution shows a low response to SIA in September, the all-sky  $SW_{acc}$  trend takes relatively longer to emerge than the clear-sky  $SW_{acc}$  trend (Fig. 4.6). This relationship is strongest for models with clear to all-sky TTE ratios less than one (below the dashed horizontal line in Fig. 4.6), although there are a few exceptions, e.g. INM-CM5-0 (○) and NorESM2-LM (▽). Recall that  $SW_{acc}$  represents the net input of SW energy at the TOA into the Arctic system over the melt season, March through September. SIA reaches its minimum in September, which is the result of energy exchanged throughout the preceding melt season, including SW, so it is not unreasonable for there to be a connection across these different time scales. And while Fig. 4.6 is not definitive, it is suggestive that there is a relationship between the atmospheric contribution and  $SW_{acc}$  TTE.

Therefore we turn to  $SW_{ref_{atm}}$ , the total sum of SW radiation reflected by the atmosphere over the melt season (Eq. 4.1). The more SW energy the atmosphere reflects than the surface, the greater the ratio between mean  $SW_{acc}$  with and without clouds across CMIP6 models (Fig. 4.7b). This relationship is largely determined by the mean  $SW_{ref_{atm}}$ , for a model (Fig. 4.7a). The less the atmosphere reflects over the melt season, the closer clear-sky and all-sky  $SW_{acc}$  are to each other; the removal of clouds has a smaller impact when they do not reflect as much SW to begin with. The inverse is also true: when the atmosphere reflects more SW, there is a greater difference between mean all-sky and clear-sky  $SW_{acc}$ .

In turn the standard deviation of  $SW_{ref_{atm}}$  influences if clouds increase or decrease  $SW_{acc}$  variability across models. This is notable because the relative noisiness of all-sky versus clear-sky  $SW_{acc}$  is a main factor in whether clouds increase or decrease  $SW_{acc}$  TTE. If clouds increase the  $SW_{acc}$  variability, they can increase the TTE because it takes longer for a trend emerge from a noisier timeseries, and vice versa.  $SW_{ref_{atm}}$  standard deviations vary by almost a factor of three across CMIP6 models in Fig. 4.7c. Models with the greatest  $SW_{ref_{atm}}$  standard deviations (MPI-ESM1-2-LR and NESM3) are the only models where clouds increase the variability of  $SW_{acc}$ , i.e. the ratio is less than 1. In models where the atmospheric reflectivity is less variable, clouds decrease  $SW_{acc}$  variability (ratio > 1). In observations clouds slightly decrease  $SW_{acc}$  variability when averaged over the full Arctic, although the regional impact of clouds on  $SW_{acc}$  depends on the underlying surface (Chapter 3). Model biases could be directly from their representations from clouds as well as from the underlying distribution of sea ice and snow cover.

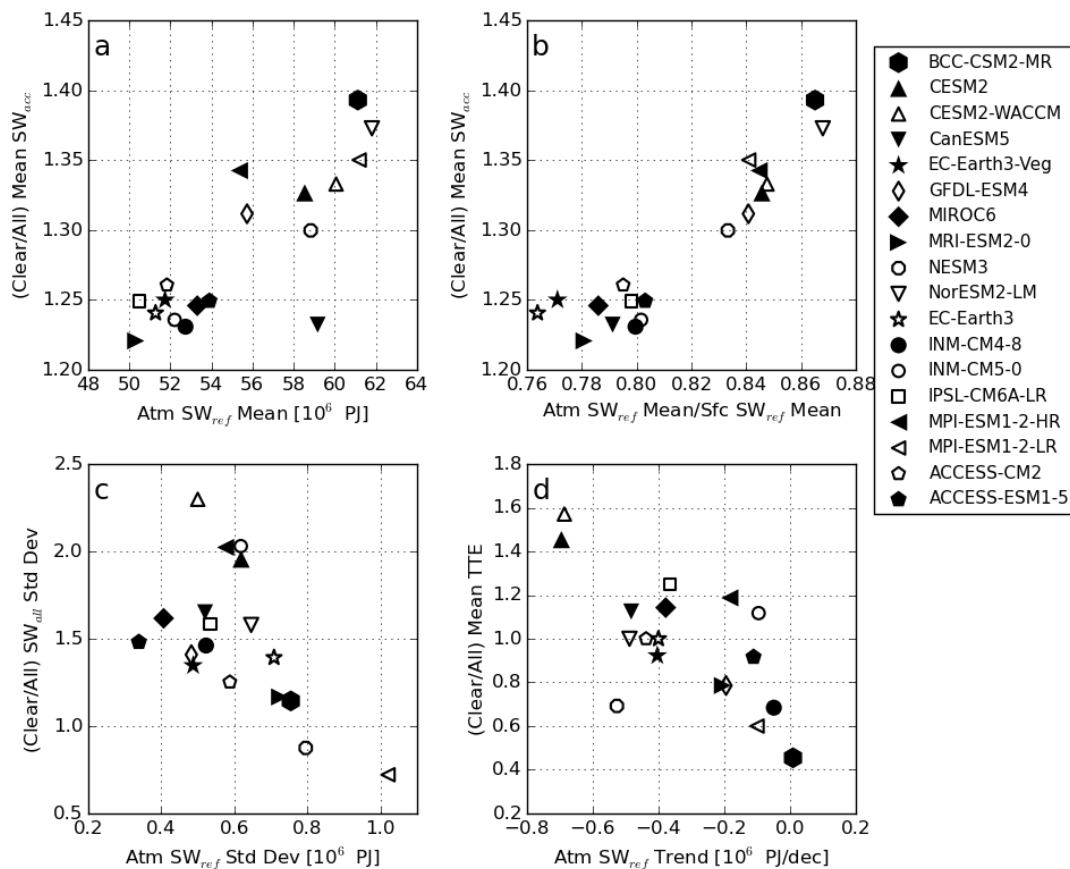


FIGURE 4.7: Total SW reflected due to the atmosphere ( $Atm SW_{ref}$ ) as it relates to accumulated SW ( $SW_{acc}$ ) ratios of all-sky to clear-sky for a) means, b) standard deviations, and c) trends and time to emergence (TTE).  $SW_{acc}$  TTE are calculated using SSP585 over 2000-2100.

Furthermore, the ratio of clear-sky to all-sky TTE has a negative relationship with the  $SW_{ref_{atm}}$  trend over the 21<sup>st</sup> century (Fig. 4.7d). All of these models agree that the total SW reflected by the atmosphere decreases in the future, but the magnitude of that decline ranges from essentially zero (BCC-CSM2-MR,  $\bullet$ ) to about  $-0.7 \times 10^6$  PJ/decade (CESM2-CAM5 and CESM2-WACCM,  $\blacktriangle$  and  $\triangle$ ). From Eq. 2.4 back in Chapter 2, the atmospheric contribution does depend on multiple reflections from the surface, so with a lower surface albedo there would be less upwelling SW at the surface and consequently a lower amount of SW reflected by the atmosphere to space over the melt season. This is in spite of the fact

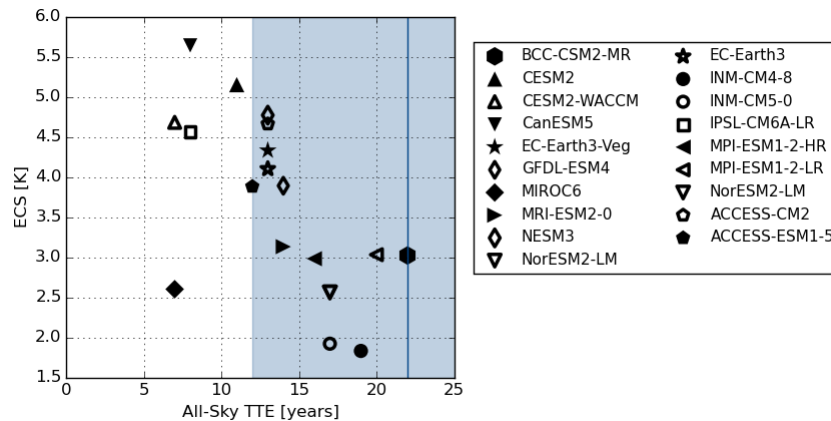


FIGURE 4.8: Relationship between all-sky  $SW_{acc}$  TTE and equilibrium climate sensitivity (ECS) in CMIP6. ECS values are from Zelinka *et al.* (2020), calculated using the Gregory method. Solid blue line is the mean all-sky  $SW_{acc}$  TTE from CERES, and blue shading represents  $\pm 1$  standard deviations of TTE.

that the atmosphere does increase as a percentage of the TOA albedo in the future (Fig. 4.2); the surface contribution just decreases much more (not shown). Our previous conclusions in Chapter 2 attributed TTE ratios to cloud fraction (CF) trends (Fig. 3.10). These results complement those earlier ones by showing that models with greater declines in CF, e.g. CESM2, have corresponding drops in  $SW_{ref_{atm}}$ . As previously noted, other cloud properties besides CF, e.g. phase and opacity, likely influence SW reflection over the 21<sup>st</sup> century, but an analysis of those variables is beyond the current scope of this work.

#### 4.3.3.1 $SW_{acc}$ TTE and Equilibrium Climate Sensitivity

We saw previously in Chapter 3 that all-sky TTE had a negative relationship with global temperature change over the 21<sup>st</sup> century —  $SW_{acc}$  trends emerge sooner in models that experience greater global warming — demonstrating a connection between Arctic and global climate change. All-sky TTE also shows a (loosely) negative relationship to the expected

warming due to a doubling of  $\text{CO}_2$ , i.e. the equilibrium climate sensitivity (ECS) (Fig. 4.8). ECS values are from Zelinka et al. (2020), calculated using the Gregory method. The expected mean all-sky  $\text{SW}_{acc}$  TTE from observations is shown in blue at 22 years, with  $\pm 2$  standard deviations shaded ( $\pm 12$  years). Broadly speaking, in models with higher ECS,  $\text{SW}_{acc}$  trends take a shorter time to emerge. The six models with ECS above 4.5 K have an average all-sky  $\text{SW}_{acc}$  TTE of 10 years, and the models with the highest ECS (CanESM5 and CESM2) show TTE outside the observational uncertainty. Models within one standard deviation of observations (16-28 years) have ECS below 3.5 K. The exception in our CMIP6 ensemble is MIROC6 ( $\blacklozenge$ ), that has both a low ECS and short TTE. While Fig. 4.8 is far from being a useful emergent constraint, it is interesting to see any sort of association between Arctic SW trends and broader model characteristics.

## 4.4 Conclusions

As we expected, albedo partitioning does align with our TTE framework: in models with greater SW reflection by the atmosphere there is a greater difference between all-sky and clear-sky  $\text{SW}_{acc}$  and TTE. Although most models generally agree on seasonal cycles of albedos, there is still a 10-15% of range in monthly means. There is an even larger spread in relationships between albedo and SIA. All the CMIP6 models have strong correlations between SIA and the surface albedo ( $>0.7$ ), but the responses of TOA albedos to SIA vary markedly. In some models the TOA albedo is strongly correlated to SIA, just as the surface albedo is, but in other models the TOA albedo is disconnected from changes at the surface. The different model behavior is linked to how the atmospheric contribution responds to

changing SIA. Thus, correctly modeling the atmosphere is needed for accurately capturing the TOA energy balance variability and response to SIA decline.

Our findings further linked changes in the atmospheric contribution over the 21<sup>st</sup> century to ratios of clear-sky to all-sky  $SW_{acc}$  TTE. When the atmosphere reflects more SW, there is a greater difference between mean all-sky and clear-sky  $SW_{acc}$ . As the atmosphere contributes a larger percentage of the TOA albedo, its changes may influence our ability to detect SW trends. Additional analysis could be done to link CF trends and mean state with trends in  $SW_{ref_{atm}}$ . Future work will include a comparison with CMIP5 models to document albedo partitioning across CMIP generations.

## **Chapter 5**

# **The influence of clouds on Arctic SST in CESM2**

### **5.1 Preface**

The previous chapters investigated how clouds can impact the Arctic energy budget, with a particular focus on solar radiation. Now we turn to what those radiative effects of clouds can mean for the physical environment, specifically upper ocean temperatures. Declining sea ice in the Arctic means there is more open ocean for longer periods of time. Previous work has looked at how radiative anomalies and clouds can impact sea ice variability, finding that LW anomalies and increased cloud cover can precondition sea ice melt in the spring and SW anomalies dominate in the summer (Huang et al., 2019, Kapsch et al., 2014). But

the timing of when radiative anomalies have the largest impact on SST maxima likely differs from that for sea ice. While LW radiation can precondition sea ice in spring and in turn cause more melt in summer, the presence of sea ice insulates the underlying ocean from the atmosphere. Similarly, the amount of SW radiation that reaches the ocean through sea ice is less than what can be absorbed for open ocean (Perovich et al., 2007), meaning that how radiative fluxes drive sea ice loss may not apply equally for ocean heat uptake. For example, 2012 has the lowest SIE minimum on record, followed by 2007, but 2007 had SST anomalies in the Pacific sector that were nearly three times greater than in 2012 (Steele and Dickinson, 2016).

Motivated in part by the differences between 2007 and 2012 melt seasons, Steele and Dickinson (2016) determined that the timing of when sea ice begins melting and fully retreats are connected to fall SST maxima in the Pacific Basin of the Arctic. Anomalously early ice retreat is linked to anomalously high SSTs due to increased energy input into the ocean surface, as was the case in 2007. However, there was no discussion of how the energy balance can be influenced by clouds, which have been linked to the low sea ice extent in 2007 (Kay et al., 2008). The surface energy budget largely determines heat uptake in the Arctic Ocean (Steele et al., 2010), and clouds are a key control of the Arctic surface energy budget (Kay and L'Ecuyer, 2013). Here we investigate if clouds can influence fall SST in the Arctic using the Community Earth System Model, version 2 (CESM2). We ask if clouds can affect ocean surface warming in the Arctic, and if so is it through warming or cooling effects? And do the impacts of clouds on SST change with a warming climate? We use model experiments

with variable CO<sub>2</sub> concentrations to answer these questions and show how the influence of clouds on upper ocean temperatures may increase with rising greenhouse gases.

## 5.2 Methods

### 5.2.1 CESM2

We use the CESM version 2.1.3 (CESM2; Danabasoglu et al. (2020)) for this work with the following components: Community Atmosphere Model version 6 (CAM6), Parallel Ocean Program (POP) version 2, Community Land Model (CLM) version 5.0, Los Alamos Sea Ice Model (CICE) version 5, OAA WaveWatch-III ocean surface wave prediction model (WW3), Community Ice Sheet Model (CISM) Version 2.1, and Model for Scale Adaptive River Transport (MOSART). All models runs are fully coupled with nominal atmosphere grid resolution 0.9x1.25 degrees. The first 100-year control run uses pre-industrial forcing, nominally year 1850 with 284.7 ppm CO<sub>2</sub> concentration, hereafter the PI-control. Additional runs were branched from a separate pre-industrial run with 1% annually increasing CO<sub>2</sub>. Branches were started after years 40 and 140, corresponding the CO<sub>2</sub> levels of 424 ppm and 1193.3 ppm, respectively. The former run represents near future conditions (global average CO<sub>2</sub> concentrations were 409.8 ppm in 2019 (Lindsey, 2020)), and the former is roughly 4x pre-industrial CO<sub>2</sub> concentration. These branches were each run for 50 years with constant CO<sub>2</sub> levels and additional daily output, including daily SST and SIC on the atmosphere grid.

### 5.2.2 Season definitions

To study the impacts of clouds on fall SST, we use several key dates and periods throughout the year, as defined in Steele and Dickinson (2016). These dates are determined using daily time series of sea ice concentration (SIC) and SST for an individual grid box. These periods are shown in Fig. 5.1, and as in Steele and Dickinson (2016), a 15-day running mean boxcar smoother is applied to daily time series. In a given year, the day of melt onset for a grid box is defined as the last day the SIC is greater or equal to 0.95 (vertical blue line in Fig. 5.1). This date is the start of the melt season. The melt season ends on the last day the SIC is at or above 0.15, called the day of heat onset (purple line). The heating, or warming, season lasts from the day of heat onset until the day of maximum SST ( $SST_{max}$ ; orange line). Defining these seasons allows for more physical comparisons than monthly lag-correlations often used. Additional variables - total cloud fraction (CF), cloud liquid water path (LWP), radiative fluxes - are averaged over these seasons to correlate with  $SST_{max}$ .

While not a focus of this chapter, a breakdown of the mean annual upper ocean heat budget for a fixed depth is included. From Yeager (2020), the total temperature tendency is given by:

$$\int_D^\eta \frac{\partial T}{\partial t} dz = - \int_D^\eta \nabla \cdot (\mathbf{u}T + \mathbf{u}^*T) dz - \int_D^\eta (\nabla \cdot \mathbf{K}) dz + \frac{Q_{net}}{\rho c_p}, \quad (5.1)$$

where  $D$  is the fixed depth,  $\eta$  is the sea surface height,  $T$  is temperature,  $\mathbf{u}$  ( $\mathbf{u}^*$ ) is the (sub-gridscale) velocity,  $\mathbf{K}$  is the three-dimensional diffusive flux,  $Q_{net}$  is the net surface flux,  $c_p$

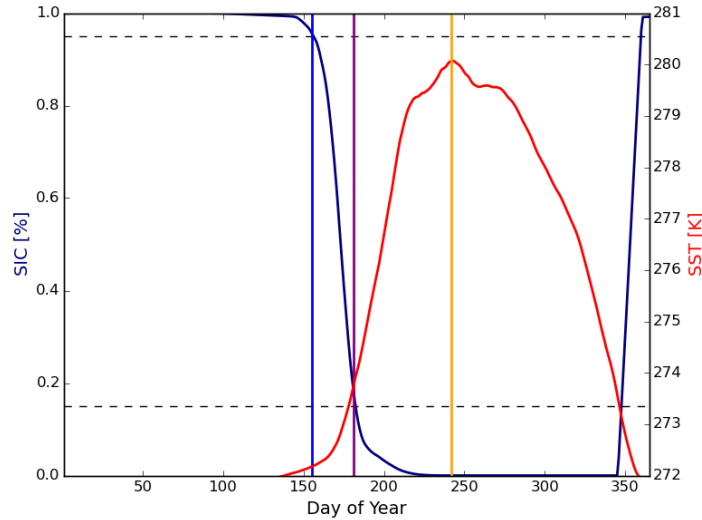


FIGURE 5.1: Daily time series of sea ice concentration (SIC; navy) and sea surface temperature (SST; red) for one grid cell ( $52^{\circ}\text{N}$ ,  $280^{\circ}\text{E}$ ) of one year in the pre-industrial control simulation. The last day SIC is greater than or equal to 0.95, the melt onset, is marked by the bright blue line, and the last day SIC is greater than or equal to 0.15, the heat onset, is marked by the purple line. The day of maximum SST is shown by the orange line. This figure is adapted from Steele and Dickinson (2016).

is the ocean heat capacity, and  $\rho$  is saltwater density. In Fig. 5.2, the temperature tendency is integrated over the upper 50 m and summed over ocean grid cells north of  $60^{\circ}\text{N}$ . The net surface flux is the sum of terms listed in Fig. 5.2b. In CESM2, ocean heat uptake in the interior Arctic appears largely dominated by surface fluxes March through September (Fig. 5.2a), particularly radiative fluxes (Fig. 5.2b), consistent with observations (Steele et al., 2010). We thus expect clouds to be able to influence upper ocean temperatures because they can influence radiative fluxes.

### 5.3 Results and Discussion

We know clouds can reduce incoming SW from reaching the surface and increase downwelling LW. The net effect of clouds on the radiation budget, warming or cooling, strongly

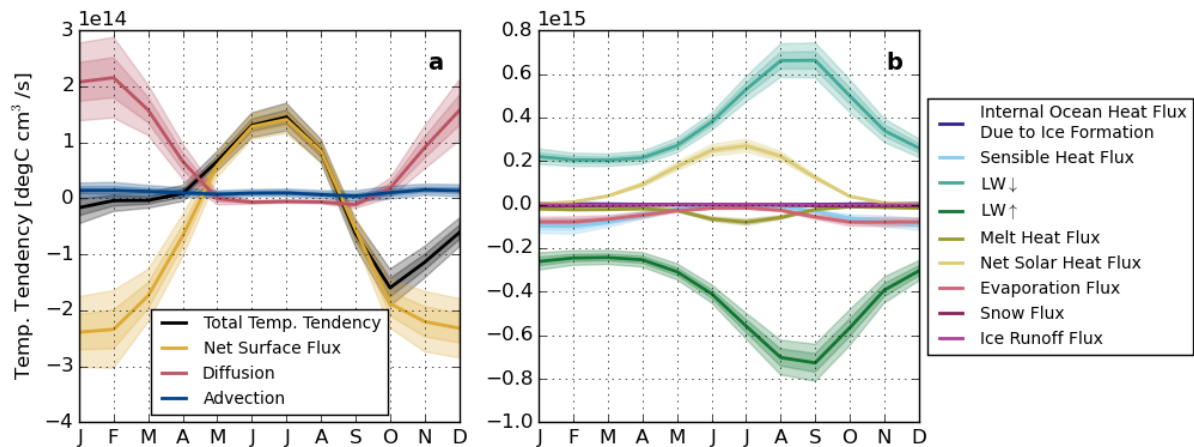


FIGURE 5.2: a) Annual cycle of ocean heat budget terms, summed over ocean grid cells poleward of 60°N for the upper 50m in pre-industrial control. b) Individual terms of the total surface flux term in (yellow line in a). Shading represents one and two standard deviations.

depends on the time of year, though, due to the strong seasonal cycle of SW in the Arctic. Figure 5.3 shows the sensitivity of downwelling LW and SW at the surface to cloud LWP, i.e. the slope of each flux regressed against LWP, for each day of the year using all ocean grid cells (land fraction < 0.5) poleward of 60°N. The magnitude of downwelling SW sensitivity (Fig. 5.3b) follows the same seasonal cycle as downwelling SW, with the greatest magnitude in summer, around day of year (DOY) 150 (June 1=DOY 152), because there is more incoming SW that can be reflected for a similar range of LWP. Downwelling LW has the opposite seasonal cycle in Fig. 5.3a. Its sensitivity to LWP decreases in summer, with a minimum near the end of July (July 31=212 DOY). During the melt season, the net impact of LWP on downwelling fluxes (SW↓ + LW↓) has its greatest magnitude ( $-0.5 \text{ Wm}^{-2}/\text{gm}^{-2}$ ) over June (approximately 150-180 DOY).

We begin with the mean state of the PI-control run. In the interior Arctic, sea ice begins

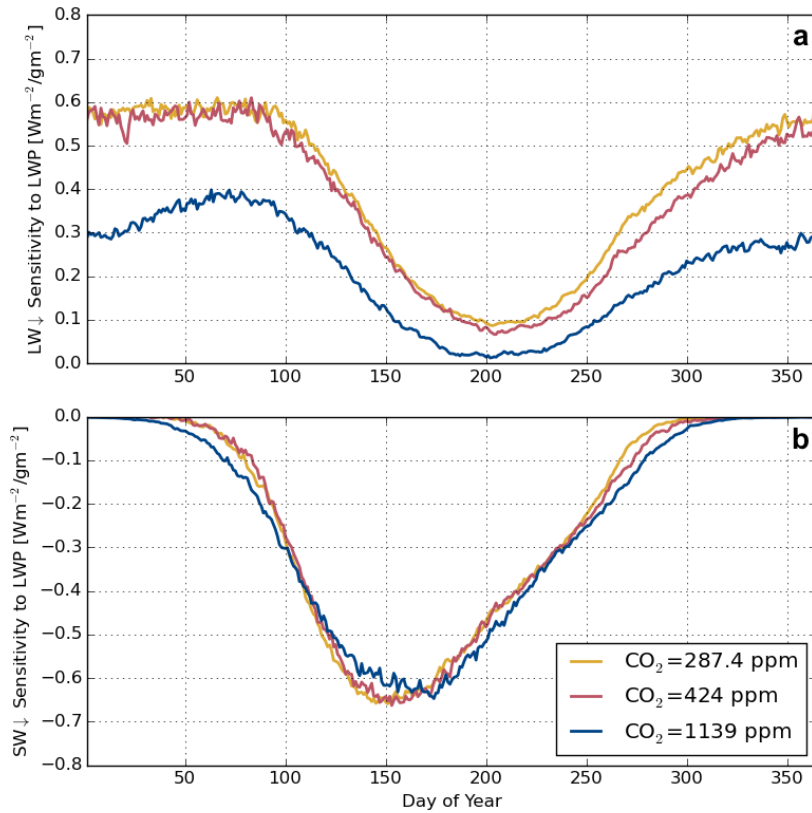


FIGURE 5.3: Sensitivity of downwelling LW (a) and SW (b) for total grid box cloud liquid water path (LWP) throughout the year. Sensitivity is calculated from the regression of all ocean grid cells north of  $60^\circ$  for each day of the year.

melting in April, gradually occurring later moving north, typically May at the highest latitudes (Fig. 5.4a). Heat onset typically occurs in August at lower latitudes, and again is delayed towards the north pole, as late as September in some areas (Fig. 5.4b).  $F_{net}$  maxima generally occur between these two dates while sea ice is melting in the interior Arctic (not shown). Around the coast, the average length of the heat season is about a month, but towards the pole it may only be a few weeks ((Fig. 5.4c).  $SST_{max}$  is strongly controlled by the date of heat onset at these high latitudes (Fig. 5.5b), negative correlations meaning that earlier heat onset leads to warmer  $SST_{max}$ . The date of melt onset has a weaker relationship to  $SST_{max}$  than heat onset (Fig. 5.5a).

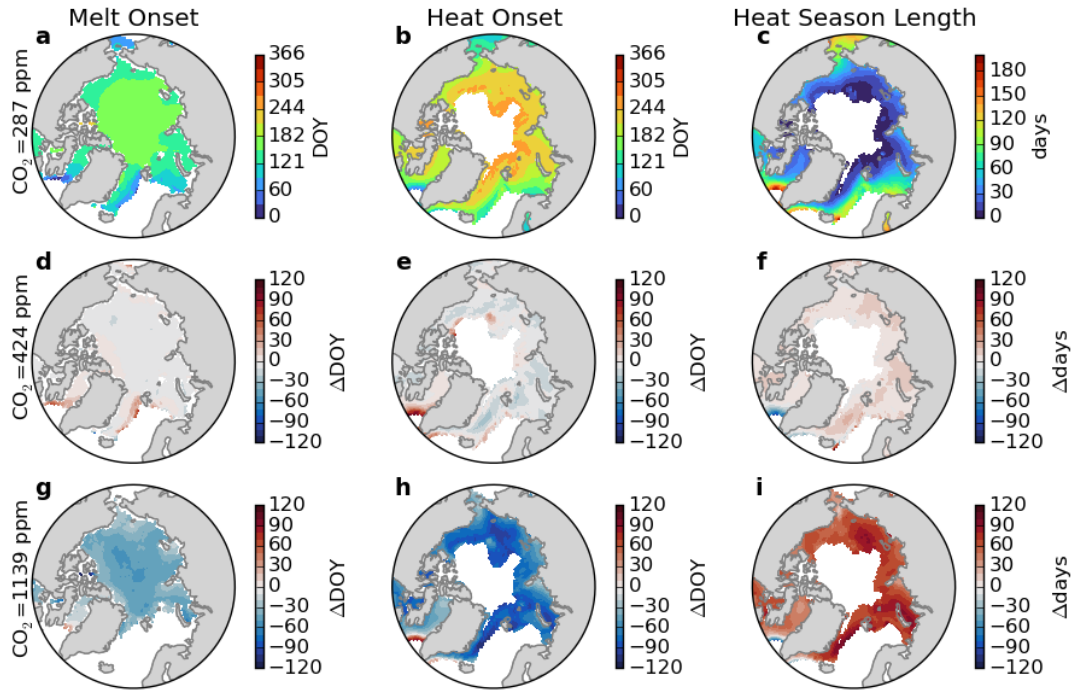


FIGURE 5.4: PI-control ( $\text{CO}_2=287.4\text{ppm}$ ) mean date of melt onset (a), heat onset (b), and length of heat season (c). Differences are given for near future ( $\text{CO}_2=424\text{ppm}$ ; d-f) and  $4\times\text{CO}_2$  ( $1139\text{ppm}$ ; g-i) values.

While we expected clouds to play a significant role on fall SST, in the PI-control their direct influence is limited. Figures 5.5c and d show correlations between average LWP during melt and heat phases with  $\text{SST}_{max}$ . Around the interior coast,  $\text{LWP}_{heat}$  and  $\text{SST}_{max}$  have weak negative correlations, suggesting clouds have a net cooling effect on ocean temperatures. The correlations become positive moving poleward, but most of these correlations are not statistically significant (t-test with 95% confidence). Regions along the interior coast are ice-free sooner than further north, so the melt season can occur early enough to experience a net cooling effect from clouds when downwelling SW is highly sensitive to LWP (Fig. 5.3b). Around the permanent ice edge, if any ocean becomes completely free of ice, it usually does not begin warming until late in the season when clouds have a net warming

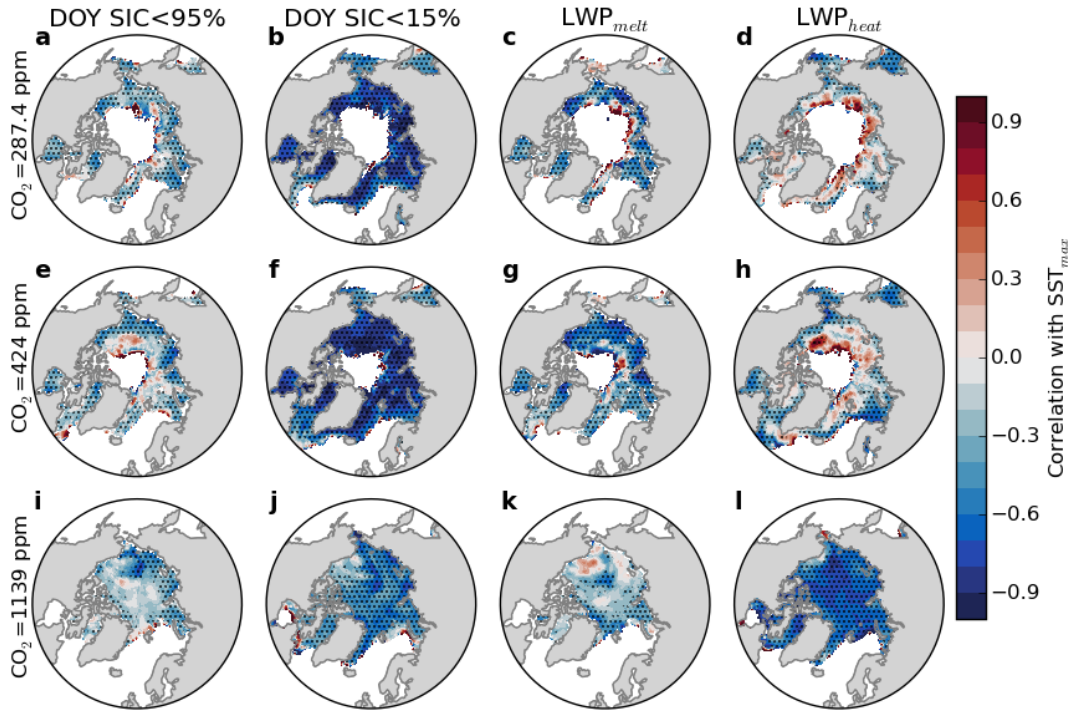


FIGURE 5.5: Correlations between  $SST_{max}$  and day of melt onset (DOY SIC<0.95; a,e,i), day of heat onset (DOY SIC<0.15; b,f,j), cloud LWP during the melt season ( $LWP_{melt}$ ; c,g,k) and heat season ( $LWP_{heat}$ ; d,h,l) for pre-industrial (287.4 ppm; a-d), near future (424 ppm; e-h) and 4xPI-control (1139 ppm; i-l)  $CO_2$  levels. Stippling represents statistically significant correlations using a t-test with 95% confidence.

effect. In both cases the impact is relatively small, though.

However, clouds can indirectly impact  $SST_{max}$  during the melt season. In the PI-control, peak SW sensitivity to LWP occurs when most grid boxes have sea ice that is melting. During this time period,  $LWP_{melt}$  negatively correlates with  $SST_{max}$  (Fig. 5.5c), with correlations typically on the order of -0.5. Increased cloud cover during the melt season has a net cooling effect that increases the length of the melt season and delays the starting of the heat season (not shown). Because the date of heat onset is strongly correlated to  $SST_{max}$  (Fig. 5.5b), its delay leads to lower SST maxima.

With higher CO<sub>2</sub> concentrations there is less sea ice and earlier ocean warming (Fig. 5.4). Under a moderate CO<sub>2</sub> increase (CO<sub>2</sub>=424 ppm), heat onset typically occurs a week or two sooner than in the PI-control (Fig. 5.4e). Earlier melt onset leads to slightly stronger correlations between SST<sub>max</sub> and LWP the melt phase compared to the PI-control, but only slightly (Fig. 5.5g). The Beaufort, East Siberian, and Laptev Seas have larger negative correlations between SST<sub>max</sub> and LWP<sub>melt</sub> compared to the control. Similarly, LWP<sub>heat</sub> and SST<sub>max</sub> also have greater correlations in this run. The increases are most notable in regions that consistently become ice free by the end of summer, such as the Barents Sea and along the coast near the Chukchi and Beaufort Seas. Some areas in the central Arctic Ocean shows increased positive correlations between LWP<sub>heat</sub> and SST<sub>max</sub> north of the Beaufort Sea, whereas most other regions have more strongly negative correlations. The heat phase of this region still primarily occurs when clouds have a net warming effect, i.e. LW is more sensitive than SW, at the end of summer. The relative importance of clouds during the melt phase compared to the heat phase remains unchanged in the near-future run compared to the PI-control, though, because the sensitivities of fluxes to LWP are similar (red compared to yellow lines in Fig. 5.3). The one exception is a slight decrease in downwelling LW sensitivity in fall that could be related to cloud feedbacks (e.g. Morrison et al. (2018)), but further investigation is needed.

A stronger increase in CO<sub>2</sub> causes stronger changes in the relationships between clouds and SST<sub>max</sub>. With 4xCO<sub>2</sub> forcing, correlations between day of heat onset and SST<sub>max</sub> decrease in magnitude compared to the control, from at least -0.8 to less than -0.5. On average, most grid cells begin warming in June, at least a month earlier than the control simulation,

around the time the net surface flux peaks (Fig. 5.4h). This shift in the timing of heat and melt seasons to earlier in the year means that the peak of SW sensitivity to LWP typically occurs during the heat season instead of the melt season. Indeed, correlation between  $LWP_{melt}$  and  $SST_{max}$  are both weaker (less than  $|0.3|$ ) and less often statistically significant compared to the lower  $CO_2$  runs (Fig. 5.5k), while  $LWP_{heat}$  has stronger correlations with  $SST_{max}$  throughout the interior Arctic Ocean (Fig. 5.5l). In fact,  $LWP_{heat}$ - $SST_{max}$  correlations are actually higher than DOY heat onset- $SST_{max}$  correlations for much of the Arctic under the  $4xCO_2$  forcing. This change occurs even though downwelling SW is less sensitive to LWP around DOY 150 (navy in Fig. 5.3b) by  $0.1 \text{ Wm}^{-2}/\text{gm}^{-2}$ . With less sea ice in the  $4xCO_2$  run, there could be fewer multiple reflections that could lower the SW sensitivity. Downwelling LW is also less sensitive to LWP in the  $4xCO_2$  run, on the order of  $0.05 \text{ Wm}^{-2}/\text{gm}^{-2}$  in summer, which could further contribute to the strong negative relationship between  $LWP_{heat}$  and  $SST_{max}$ . LW may be less sensitive to LWP because greenhouse gases play a larger role in determining LW.

## 5.4 Preliminary Conclusions and Future Work

From this initial analysis, we find that clouds can play a bigger role in determining fall SST in climate with more  $CO_2$ . In PI and near-future CESM2, clouds primarily impact  $SST_{max}$  indirectly. In these runs, clouds modulate downwelling SW to impact the length of the melt season and start of the warming season, i.e. fewer clouds allow more sunlight to reach the surface and melt sea ice sooner. Clouds during the heat season are less influential on  $SST_{max}$  than the timing of when the ocean begins warming in these runs. With  $4xCO_2$ ,

more Arctic sea ice melts completely and earlier in the summer. This shift in timing allows clouds to directly influence  $SST_{max}$  by altering the amount of incoming SW and thus the surface energy budget.

While our preliminary results seem promising, there is still work to be done. Future analyses will include quantifying the influence of clouds on the upper ocean heat and surface energy budgets, as well as exploring any differences in clouds between the CO<sub>2</sub> experiments using output from satellite simulators. Thought should also be given to the caveats of this study. Does CESM2 adequately represent clouds and cloud forcing in the Arctic? And how realistic and/or relevant are these results given the shortcomings of CESM2, specifically the low sea ice volume?

## Chapter 6

### Synthesis

This thesis covers research on Arctic climate, clouds and radiative energy across multiple data sources. In Chapter 2 we used satellite observations to determine how much the atmosphere and surface each contribute to the planetary albedo; quantified the contribution from clouds and their masking effect; and compared the observational results with reanalyses. Chapter 3 evaluated how clouds impact SW absorption trends and their detection in observations and CMIP6, both pan-Arctic and regionally. Chapter 4 bridged the ideas of TOA albedo partitioning with accumulated SW in CMIP6. Finally, Chapter 5 showed preliminary results for how clouds can impact SST anomalies in the Arctic by modulating radiative fluxes in CESM2.

The overarching theme of this work is that clouds are important to the Arctic energy balance, particularly in determining how much SW is reflected or absorbed. From satellite

observations, the atmosphere, namely clouds, contribute at least 60% and up to 90% of the TOA albedo on average during sunlit months, in spite of the high surface albedos found in the Arctic. Clouds have a damping effect on the seasonal cycle of the TOA albedo, also making it less sensitive to changes in surface cover; during the melt season the TOA albedo is roughly half as sensitive to changes in sea ice as the surface albedo. This damping effect leads to less SW being absorbed relative to clear-sky values on a seasonal scale. Over the full Arctic, clouds have delayed the emergence of  $SW_{acc}$  trends beyond the CERES record because they reduce the magnitude of the  $SW_{acc}$  trend. However, regional effects of clouds on  $SW_{acc}$  trends and variability differ based on the surface properties. Clouds reduce  $SW_{acc}$  trends and variability over sea ice, which is consistent with the large impact of clouds on the atmospheric contribution to the TOA albedo over such surfaces, but clouds can increase  $SW_{acc}$  variability over open ocean. In CESM2 we looked for the physical results of clouds modulating radiative fluxes in the Arctic. We find that while downwelling fluxes are sensitive to cloud cover, the seasonal cycles of fluxes and sea ice determine when fall SST is itself sensitive to clouds. We expect clouds to have stronger connections to SST as global  $CO_2$  levels continue to increase, though.

The frameworks presented in Chapters 2 and 3, albedo partitioning and time to emergence, respectively, were also used to benchmark other data sources, namely reanalyses and GCMs. We found a 10% spread in mean TOA albedo and its contributions across reanalyses. The sensitivity of the TOA albedo and its contributions to sea ice also vary in magnitude and sign, suggesting that fluxes from reanalyses may not be considered equivalent to observations in the Arctic. Models participating in CMIP6 have a similar spread

in albedos as reanalyses, on the order of 10% during the melt season, and they further disagree on how correlated the TOA albedo is to sea ice. These differences between models appear related to the representation of the atmospheric contribution and its response to sea ice. GCMs further diverge in their predictions of how the atmospheric contribution may change in the coming decades, although they all agree that it will contribute a larger percentage of the planetary albedo. These differences are surely related to different projections of cloud cover in the Arctic. Understanding model biases is necessary, although insufficient, for improving them. Investigating and comparing GCMs is also important as those outside academia, and specifically policy makers, looks towards climate science to answer what Earth may look like under possible warming scenarios. While reanalyses and GCMs can fill in gaps from the observations, being aware of their limitations is imperative for using them wisely, both in terms of moving forward and communicating to the public.

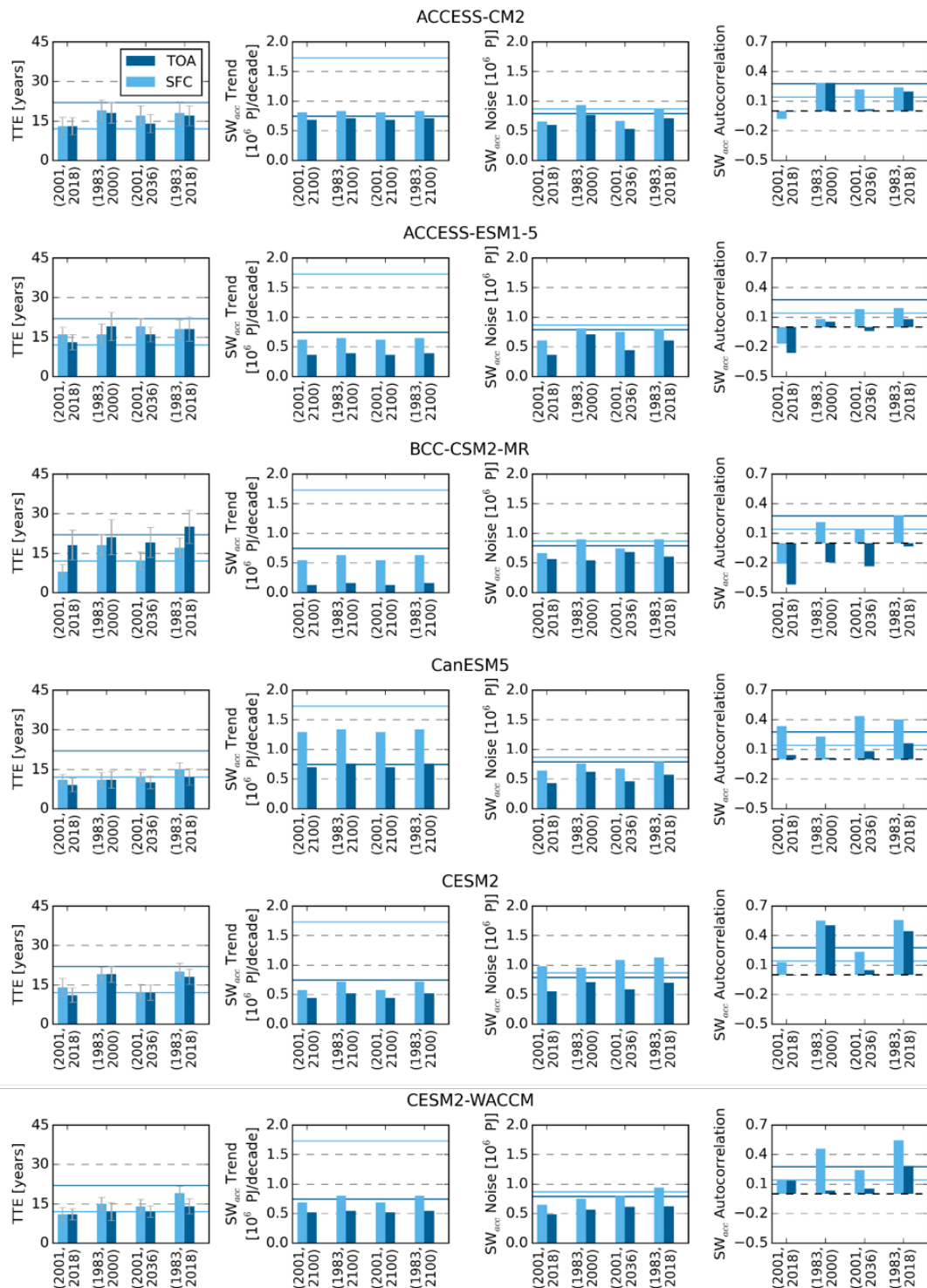
Future work is planned for the unanswered questions that arose in Chapters 4 and 5. Albedo partitioning and  $SW_{acc}$  analyses will be repeated in CMIP5 to benchmark any changes between CMIP generations. Continuing from Chapter 5, work will include further analysis of how Arctic clouds can impact SST in CESM2 by looking at the upper ocean heat budget and cloud variables from satellite simulators. The possibility also exists for future studies on the role of cloud-feedbacks on ocean heat uptake in the Arctic using CESM2. Taken altogether, this research has laid the groundwork for my understanding of how clouds can impact radiative fluxes in a changing Arctic, as well as the limitations of available data sources.

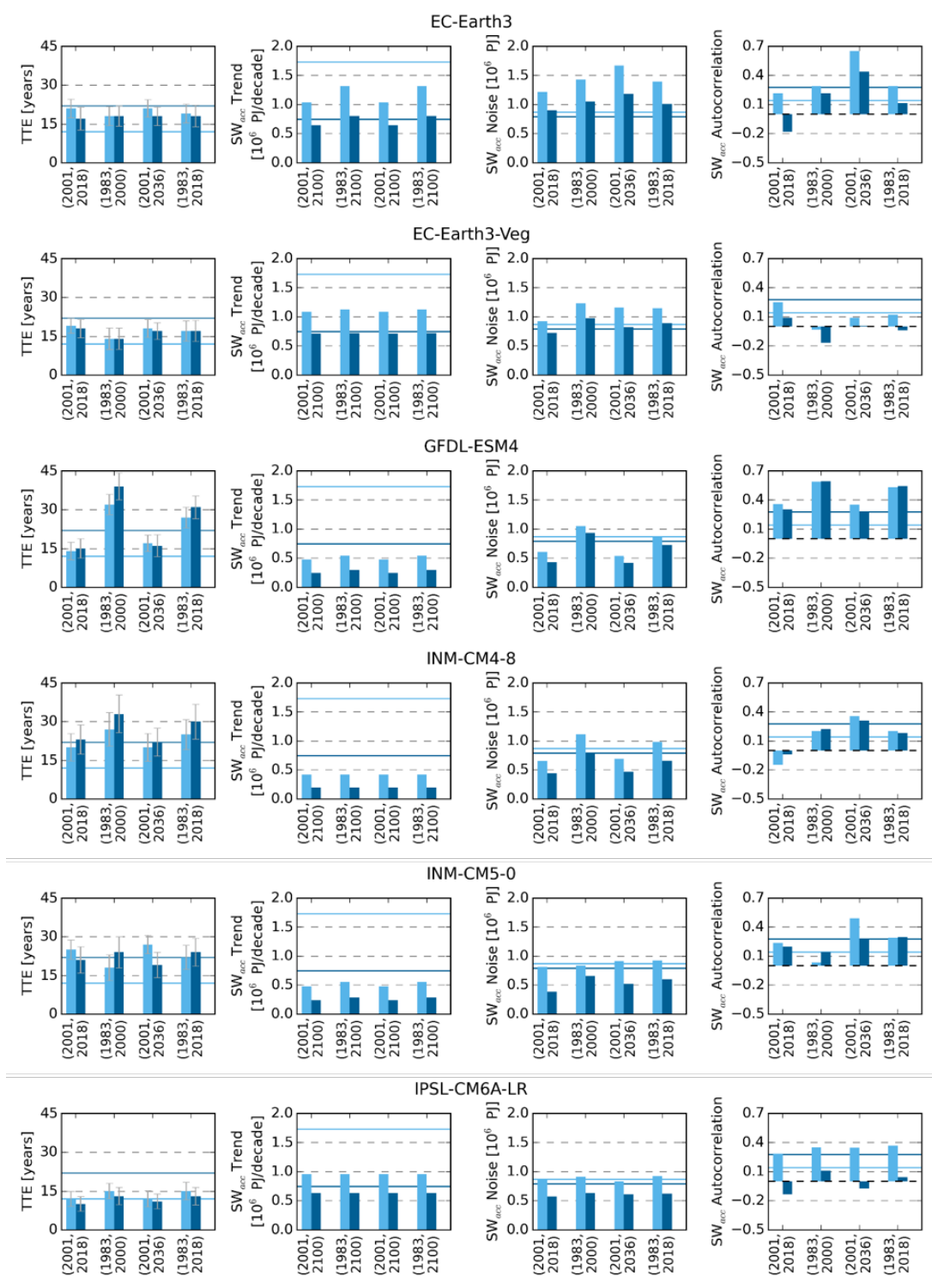
# Appendix A

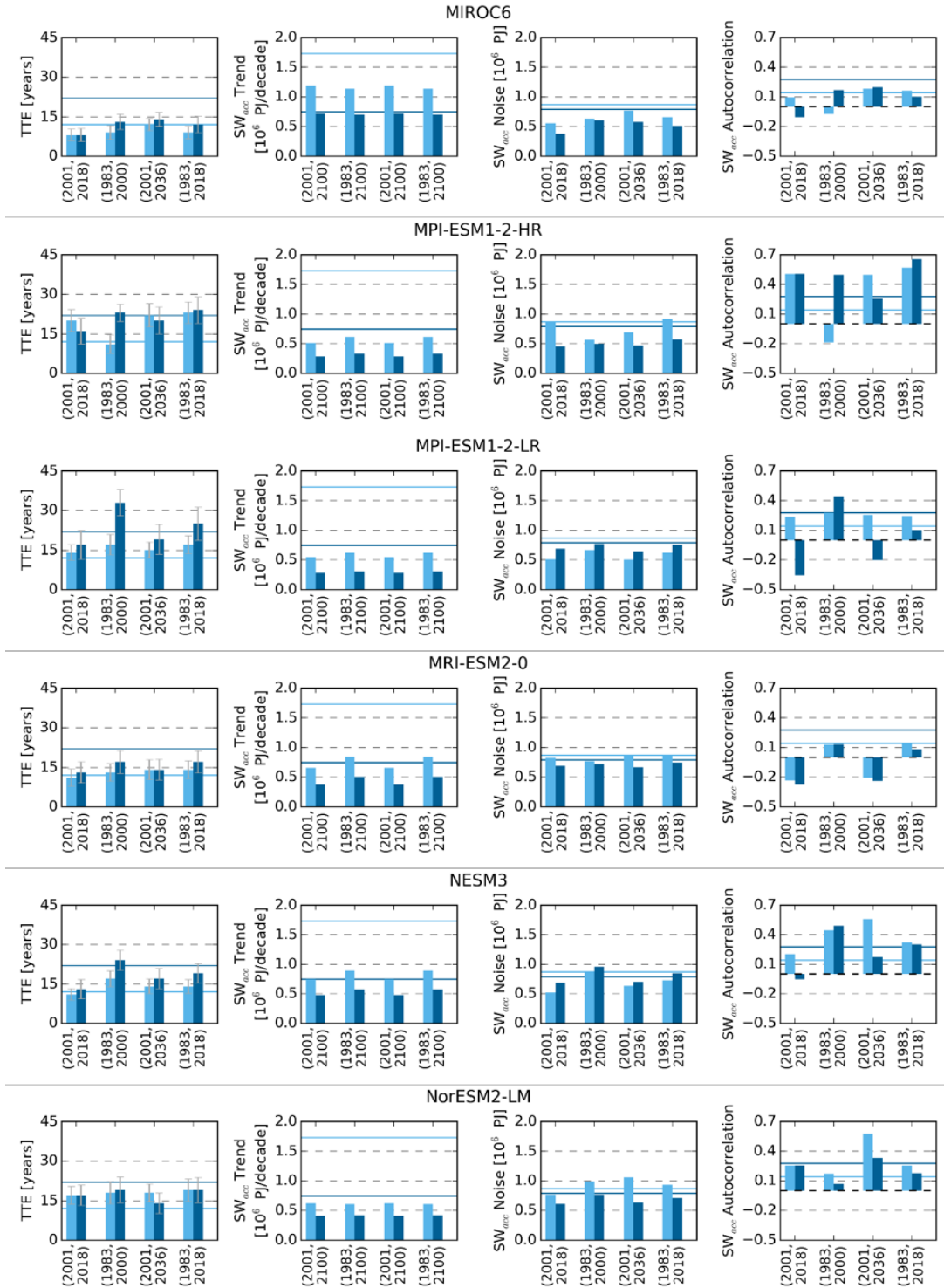
## Supplemental Figures

### A.1 Supplemental Figures for Section 3.3

All-sky top of atmosphere ( $TOA_{all}$ ) and clear-sky surface ( $SFC_{clr}$ ) accumulated shortwave ( $SW_{acc}$ ) time to emergence (TTE), trend, noise and one-lag autocorrelation calculated from four different time periods for each of the CMIP6 models investigated here using SSP245. Solid lines represent values from CERES-EBAF. Of the 18 models, six have  $SFC_{clr}$  TTE that are within one standard deviation of each other across all time periods, and seven have  $TOA_{all}$  TTE that are consistent in this way. The results are consistent for SSP585 and if additional time periods are used.







## A.2 Supplemental Figure for Section 3.4

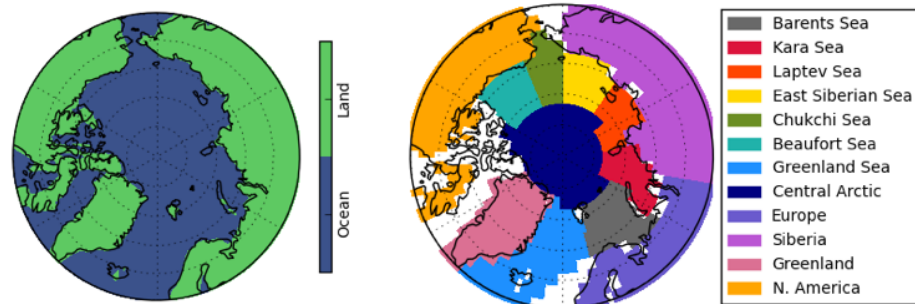


FIGURE A.1: Maps of Arctic regions. (left) Area considered land or ocean in the Arctic based on regrided land fraction variable from NCEP reanalysis. (right) Individual land areas and seas used in the text. Eurasia is the total area encompassing Europe and Siberia. NCEP land masks from ArORIS are also used to determine the individual land regions. Marginal seas are based on the Multisensor Analyzed Sea Ice Extent regions from the National Snow and Ice Data Center interpolated to the ArORIS grid.

## Bibliography

- Bacmeister, J. T., M. J. Suarez, and F. R. Robertson, 2006: Rain reevaporation, boundary layer–convection interactions, and pacific rainfall patterns in an agcm. *Journal of the Atmospheric Sciences*, **63**, 3383–3403.
- Bintanja, R. and F. Krikken, 2016: Magnitude and pattern of arctic warming governed by the seasonality of radiative forcing. *Scientific reports*, **6**, 1–7.
- Blanchard-Wrigglesworth, E., K. C. Armour, C. M. Bitz, and E. DeWeaver, 2011: Persistence and inherent predictability of Arctic sea ice in a GCM ensemble and observations. *Journal of Climate*, **24**, 231–250.
- Bosilovich, M. G., 2015: *MERRA-2: Initial evaluation of the climate*. National Aeronautics and Space Administration, Goddard Space Flight Center.
- Box, J. E., D. H. Bromwich, and L.-S. Bai, 2004: Greenland ice sheet surface mass balance 1991–2000: Application of polar mm5 mesoscale model and in situ data. *Journal of Geophysical Research: Atmospheres*, **109**.

- Box, J. E., W. T. Colgan, T. R. Christensen, N. M. Schmidt, M. Lund, F.-J. W. Parmentier, R. Brown, U. S. Bhatt, E. S. Euskirchen, V. E. Romanovsky, et al., 2019: Key indicators of Arctic climate change: 1971–2017. *Environmental Research Letters*, **14**, 045010.
- Brodzik, M. J. and R. Armstrong, 2013: Northern Hemisphere EASE-grid 2.0 weekly snow cover and sea ice extent, version 4. <https://doi.org/10.5067/P7O0HGJLYUQU>.
- Bromwich, D., Y.-H. Kuo, M. Serreze, J. Walsh, L.-S. Bai, M. Barlage, K. Hines, and A. Slater, 2010: Arctic system reanalysis: call for community involvement. *Eos, Transactions American Geophysical Union*, **91**, 13–14.
- Bromwich, D., A. Wilson, L. Bai, Z. Liu, M. Barlage, C.-F. Shih, S. Maldonado, K. Hines, S.-H. Wang, J. Woollen, et al., 2018: The arctic system reanalysis, version 2. *Bulletin of the American Meteorological Society*, **99**, 805–828.
- Cao, Y., S. Liang, T. He, and X. Chen, 2016: Evaluation of four reanalysis surface albedo data sets in Arctic using a satellite product. *IEEE Geoscience and Remote Sensing Letters*, **13**, 384–388.
- Carmack, E., I. Polyakov, L. Padman, I. Fer, E. Hunke, J. Hutchings, J. Jackson, D. Kelley, R. Kwok, C. Layton, et al., 2015: Toward quantifying the increasing role of oceanic heat in sea ice loss in the new Arctic. *Bulletin of the American Meteorological Society*, **96**, 2079–2105.
- CERES, 2014: CERES\_EBAF\_Ed2.8 data quality summary. [https://ceres.larc.nasa.gov/documents/DQ\\_summaries/CERES\\_EBAF\\_Ed2.8\\_DQS.pdf](https://ceres.larc.nasa.gov/documents/DQ_summaries/CERES_EBAF_Ed2.8_DQS.pdf).

— 2020: CERES\_EBAF\_Surface\_Ed4.1 data quality summary. [https://ceres.larc.nasa.gov/documents/DQ\\_summaries/CERES\\_EBAF\\_Ed4.1\\_DQS.pdf](https://ceres.larc.nasa.gov/documents/DQ_summaries/CERES_EBAF_Ed4.1_DQS.pdf).

Cesana, G., J. Kay, H. Chepfer, J. English, and G. De Boer, 2012: Ubiquitous low-level liquid-containing Arctic clouds: New observations and climate model constraints from CALIPSO-GOCCP. *Geophysical Research Letters*, **39**.

Chan, M. A. and J. C. Comiso, 2013: Arctic cloud characteristics as derived from modis, calipso, and cloudsat. *Journal of climate*, **26**, 3285–3306.

Chepfer, H., V. Noël, M. Chiriaco, B. Wielicki, D. Winker, N. Loeb, and R. Wood, 2018: The potential of a multidecade spaceborne lidar record to constrain cloud feedback. *Journal of Geophysical Research: Atmospheres*, **123**, 5433–5454.

Chernokulsky, A. and I. I. Mokhov, 2012: Climatology of total cloudiness in the arctic: An intercomparison of observations and reanalyses. *Advances in Meteorology*, **2012**.

Choi, Y.-S., J. Hwang, J. Ok, D.-S. R. Park, H. Su, J. H. Jiang, L. Huang, and T. Limpasuvan, 2020: Effect of arctic clouds on the ice-albedo feedback in midsummer. *International Journal of Climatology*, **40**, 4707–4714.

Christensen, M. W., A. Behrangi, T. S. L'ecuyer, N. B. Wood, M. D. Lebsock, and G. L. Stephens, 2016: Arctic observation and reanalysis integrated system: A new data product for validation and climate study. *Bulletin of the American Meteorological Society*, **97**, 907–916.

- Comiso, J. C., 2002: A rapidly declining perennial sea ice cover in the Arctic. *Geophysical Research Letters*, **29**, 17–1.
- Comiso, J. C. and D. K. Hall, 2014: Climate trends in the arctic as observed from space. *Wiley Interdisciplinary Reviews: Climate Change*, **5**, 389–409.
- Comiso, J. C., C. L. Parkinson, R. Gersten, and L. Stock, 2008: Accelerated decline in the Arctic sea ice cover. *Geophysical research letters*, **35**.
- Curry, J. A., J. L. Schramm, and E. E. Ebert, 1995: Sea ice-albedo climate feedback mechanism. *Journal of Climate*, **8**, 240–247.
- Curry, J. A., J. L. Schramm, W. B. Rossow, and D. Randall, 1996: Overview of arctic cloud and radiation characteristics. *Journal of Climate*, **9**, 1731–1764.
- Danabasoglu, G., J.-F. Lamarque, J. Bacmeister, D. Bailey, A. DuVivier, J. Edwards, L. Emmons, J. Fasullo, R. Garcia, A. Gettelman, et al., 2020: The community earth system model version 2 (cesm2). *Journal of Advances in Modeling Earth Systems*, **12**.
- Dolinar, E. K., X. Dong, B. Xi, J. H. Jiang, and H. Su, 2015: Evaluation of CMIP5 simulated clouds and TOA radiation budgets using NASA satellite observations. *Climate Dynamics*, **44**, 2229–2247.
- Donohoe, A. and D. S. Battisti, 2011: Atmospheric and surface contributions to planetary albedo. *Journal of Climate*, **24**, 4402–4418.

- Dutra, E., G. Balsamo, P. Viterbo, P. M. Miranda, A. Beljaars, C. Schär, and K. Elder, 2010: An improved snow scheme for the ecmwf land surface model: Description and offline validation. *Journal of Hydrometeorology*, **11**, 899–916.
- Duynkerke, P. G. and S. R. de Roode, 2001: Surface energy balance and turbulence characteristics observed at the sheba ice camp during fire iii. *Journal of Geophysical Research: Atmospheres*, **106**, 15313–15322.
- Ebert, E. E. and J. A. Curry, 1993: An intermediate one-dimensional thermodynamic sea ice model for investigating ice-atmosphere interactions. *Journal of Geophysical Research: Oceans*, **98**, 10085–10109.
- Eyring, V., S. Bony, G. A. Meehl, C. A. Senior, B. Stevens, R. J. Stouffer, and K. E. Taylor, 2016: Overview of the Coupled Model Intercomparison Project Phase 6 (CMIP6) experimental design and organization. *Geoscientific Model Development (Online)*, **9**.
- Feldman, D. R., C. A. Algeri, W. D. Collins, Y. L. Roberts, and P. A. Pilewskie, 2011: Simulation studies for the detection of changes in broadband albedo and shortwave nadir reflectance spectra under a climate change scenario. *Journal of Geophysical Research: Atmospheres*, **116**.
- Gelaro, R., W. McCarty, M. J. Suárez, R. Todling, A. Molod, L. Takacs, C. A. Randles, A. Darmenov, M. G. Bosilovich, R. Reichle, et al., 2017: The modern-era retrospective analysis for research and applications, version 2 (merra-2). *Journal of Climate*, **30**, 5419–5454.

- Gero, P. J. and D. D. Turner, 2011: Long-term trends in downwelling spectral infrared radiance over the US Southern Great Plains. *Journal of climate*, **24**, 4831–4843.
- Gorodetskaya, I. V., M. A. Cane, L.-B. Tremblay, and A. Kaplan, 2006: The effects of sea ice and land-snow concentrations on planetary albedo from the earth radiation budget experiment. *Atmosphere-Ocean*, **44**, 195–205.
- Gorodetskaya, I. V., L.-B. Tremblay, B. Liepert, M. A. Cane, and R. I. Cullather, 2008: The influence of cloud and surface properties on the Arctic Ocean shortwave radiation budget in coupled models. *Journal of climate*, **21**, 866–882.
- Gregory, D., J.-J. Morcrette, C. Jakob, A. Beljaars, and T. Stockdale, 2000: Revision of convection, radiation and cloud schemes in the ecmwf integrated forecasting system. *Quarterly Journal of the Royal Meteorological Society*, **126**, 1685–1710.
- Hall, D. K. and G. A. Riggs, 2015: MODIS/Terra snow cover monthly L3 global 0.05deg CMG, version 6.  
URL <https://doi.org/10.5067/MODIS/MOD10CM.006>
- Hartmann, D. L. and P. Ceppi, 2014: Trends in the ceres dataset, 2000–13: The effects of sea ice and jet shifts and comparison to climate models. *Journal of climate*, **27**, 2444–2456.
- Hines, K. M. and D. H. Bromwich, 2017: Simulation of late summer arctic clouds during ascos with polar wrf. *Monthly Weather Review*, **145**, 521–541.
- Hofer, S., A. J. Tedstone, X. Fettweis, and J. L. Bamber, 2017: Decreasing cloud cover drives the recent mass loss on the greenland ice sheet. *Science Advances*, **3**, e1700584.

Hogan, R., 2017: Radiation quantities in the ecmwf model and mars.

Huang, Y., G. Chou, Y. Xie, and N. Souldard, 2019: Radiative control of the interannual variability of arctic sea ice. *Geophysical Research Letters*.

Huang, Y., X. Dong, B. Xi, E. K. Dolinar, R. E. Stanfield, and S. Qiu, 2017: Quantifying the uncertainties of reanalyzed arctic cloud and radiation properties using satellite surface observations. *Journal of Climate*, **30**, 8007–8029.

Hwang, J., Y.-S. Choi, W. Kim, H. Su, and J. H. Jiang, 2018: Observational estimation of radiative feedback to surface air temperature over Northern High Latitudes. *Climate Dynamics*, **50**, 615–628.

Intrieri, J., C. Fairall, M. Shupe, P. Persson, E. Andreas, P. Guest, and R. Moritz, 2002: An annual cycle of arctic surface cloud forcing at sheba. *Journal of Geophysical Research: Oceans*, **107**, SHE–13.

Kalnay, E., M. Kanamitsu, R. Kistler, W. Collins, D. Deaven, L. Gandin, M. Iredell, S. Saha, G. White, J. Woollen, et al., 1996: The ncep/ncar 40-year reanalysis project. *Bulletin of the American meteorological Society*, **77**, 437–472.

Kanamitsu, M., W. Ebisuzaki, J. Woollen, S.-K. Yang, J. Hnilo, M. Fiorino, and G. Potter, 2002: Ncep–doe amip-ii reanalysis (r-2). *Bulletin of the American Meteorological Society*, **83**, 1631–1643.

- Kapsch, M.-L., R. G. Graversen, T. Economou, and M. Tjernström, 2014: The importance of spring atmospheric conditions for predictions of the arctic summer sea ice extent. *Geophysical Research Letters*, **41**, 5288–5296.
- Katlein, C., S. Hendricks, and J. Key, 2017: Brief communication: Antarctic sea ice gain does not compensate for increased solar absorption from Arctic ice loss. *The Cryosphere Discussions*, 1–8.
- Kato, S., N. G. Loeb, P. Minnis, J. A. Francis, T. P. Charlock, D. A. Rutan, E. E. Clothiaux, and S. Sun-Mack, 2006: Seasonal and interannual variations of top-of-atmosphere irradiance and cloud cover over polar regions derived from the CERES data set. *Geophysical Research Letters*, **33**.
- Kato, S., N. G. Loeb, F. G. Rose, D. R. Doelling, D. A. Rutan, T. E. Caldwell, L. Yu, and R. A. Weller, 2013: Surface irradiances consistent with ceres-derived top-of-atmosphere shortwave and longwave irradiances. *Journal of Climate*, **26**, 2719–2740.
- Kato, S., F. G. Rose, D. A. Rutan, T. J. Thorsen, N. G. Loeb, D. R. Doelling, X. Huang, W. L. Smith, W. Su, and S.-H. Ham, 2018: Surface irradiances of edition 4.0 clouds and the earth's radiant energy system (CERES) energy balanced and filled (EBAF) data product. *Journal of Climate*, **31**, 4501–4527.
- Kay, J. E. and A. Gettelman, 2009: Cloud influence on and response to seasonal Arctic sea ice loss. *Journal of Geophysical Research: Atmospheres*, **114**.

- Kay, J. E. and T. L'Ecuyer, 2013: Observational constraints on Arctic Ocean clouds and radiative fluxes during the early 21st century. *Journal of Geophysical Research: Atmospheres*, **118**, 7219–7236.
- Kay, J. E., T. L'Ecuyer, A. Gettelman, G. Stephens, and C. O'Dell, 2008: The contribution of cloud and radiation anomalies to the 2007 Arctic sea ice extent minimum. *Geophysical Research Letters*, **35**.
- Kay, J. E., T. L'Ecuyer, H. Chepfer, N. Loeb, A. Morrison, and G. Cesana, 2016: Recent advances in Arctic cloud and climate research. *Current Climate Change Reports*, **2**, 159–169.
- Landrum, L. and M. M. Holland, 2020: Extremes become routine in an emerging new arctic. *Nature Climate Change*, **10**, 1108–1115.
- Lenaerts, J., K. Van Tricht, S. Lhermitte, and T. S. L'Ecuyer, 2017: Polar clouds and radiation in satellite observations, reanalyses, and climate models. *Geophysical Research Letters*, **44**, 3355–3364.
- Leroy, S. S., J. G. Anderson, and G. Ohring, 2008: Climate signal detection times and constraints on climate benchmark accuracy requirements. *Journal of Climate*, **21**, 841–846.
- Letterly, A., J. Key, and Y. Liu, 2018: Arctic climate: Changes in sea ice extent outweigh changes in snow cover. *The Cryosphere*, **12**, 3373–3382.

- Li, J.-L., D. Waliser, G. Stephens, S. Lee, T. L'Ecuyer, S. Kato, N. Loeb, and H.-Y. Ma, 2013: Characterizing and understanding radiation budget biases in CMIP3/CMIP5 GCMs, contemporary GCM, and reanalysis. *Journal of Geophysical Research: Atmospheres*, **118**, 8166–8184.
- Lian, T., 2017: Uncertainty in detecting trend: a new criterion and its applications to global SST. *Climate Dynamics*, **49**, 2881–2893.
- Lindsay, R. and A. Schweiger, 2015: Arctic sea ice thickness loss determined using subsurface, aircraft, and satellite observations. *Cryosphere*, **9**.
- Lindsay, R., M. Wensnahan, A. Schweiger, and J. Zhang, 2014: Evaluation of seven different atmospheric reanalysis products in the arctic. *Journal of Climate*, **27**, 2588–2606.
- Lindsey, R., 2020: Climate change: Atmospheric carbon dioxide.
- URL <https://www.climate.gov/news-features/understanding-climate/climate-change-atmospheric-carbon-dioxide#:~:text=The%20global%20average%20atmospheric%20carbon,least%20the%20past%20800%2C000%20years.>
- Liu, Y. and J. R. Key, 2016: Assessment of arctic cloud cover anomalies in atmospheric reanalysis products using satellite data. *Journal of Climate*, **29**, 6065–6083.
- Liu, Y., J. R. Key, S. A. Ackerman, G. G. Mace, and Q. Zhang, 2012: Arctic cloud macrophysical characteristics from cloudsat and calipso. *Remote Sensing of Environment*, **124**, 159–173.

Loeb, N. G., D. R. Doelling, H. Wang, W. Su, C. Nguyen, J. G. Corbett, L. Liang, C. Mitrescu, F. G. Rose, and S. Kato, 2018: Clouds and the earth's radiant energy system (CERES) energy balanced and filled (EBAF) top-of-atmosphere (TOA) edition-4.0 data product. *Journal of Climate*, **31**, 895–918.

Loeb, N. G., F. G. Rose, S. Kato, D. A. Rutan, W. Su, H. Wang, D. R. Doelling, W. L. Smith, and A. Gettelman, 2020: Toward a consistent definition between satellite and model clear-sky radiative fluxes. *Journal of Climate*, **33**, 61–75.

Long, Z. and W. Perrie, 2017: Changes in ocean temperature in the barents sea in the twenty-first century. *Journal of Climate*, **30**, 5901–5921.

L'Ecuyer, T. S., H. K. Beaudoin, M. Rodell, W. Olson, B. Lin, S. Kato, C. A. Clayson, E. Wood, J. Sheffield, R. Adler, et al., 2015: The observed state of the energy budget in the early twenty-first century. *Journal of Climate*, **28**, 8319–8346.

McIlhattan, E. A., T. S. L'Ecuyer, and N. B. Miller, 2017: Observational evidence linking Arctic supercooled liquid cloud biases in CESM to snowfall processes. *Journal of Climate*, **30**, 4477–4495.

Morrison, A., J. Kay, H. Chepfer, R. Guzman, and V. Yettella, 2018: Isolating the liquid cloud response to recent arctic sea ice variability using spaceborne lidar observations. *Journal of Geophysical Research: Atmospheres*, **123**, 473–490.

- Morrison, A., J. E. Kay, W. Frey, H. Chepfer, and R. Guzman, 2019: Cloud response to Arctic sea ice loss and implications for future feedback in the CESM1 climate model. *Journal of Geophysical Research: Atmospheres*, **124**, 1003–1020.
- Myers-Smith, I. H., J. T. Kerby, G. K. Phoenix, J. W. Bjerke, H. E. Epstein, J. J. Assmann, C. John, L. Andreu-Hayles, S. Angers-Blondin, P. S. Beck, et al., 2020: Complexity revealed in the greening of the arctic. *Nature Climate Change*, **10**, 106–117.
- Onarheim, I. H. and M. Årthun, 2017: Toward an ice-free Barents Sea. *Geophysical Research Letters*, **44**, 8387–8395.
- Onarheim, I. H., T. Eldevik, L. H. Smedsrud, and J. C. Stroeve, 2018: Seasonal and regional manifestation of Arctic sea ice loss. *Journal of Climate*, **31**, 4917–4932.
- O’Neill, B. C., C. Tebaldi, D. P. Van Vuuren, V. Eyring, P. Friedlingstein, G. Hurtt, R. Knutti, E. Kriegler, J.-F. Lamarque, J. Lowe, et al., 2016: The scenario model intercomparison project (ScenarioMIP) for CMIP6.
- Peng, G., W. N. Meier, D. Scott, and M. Savoie, 2013: A long-term and reproducible passive microwave sea ice concentration data record for climate studies and monitoring. *Earth System Science Data*, **5**, 311–318.
- Perovich, D., T. Grenfell, B. Light, and P. Hobbs, 2002: Seasonal evolution of the albedo of multiyear arctic sea ice. *Journal of Geophysical Research: Oceans*, **107**, SHE–20.
- Perovich, D. K., 2018: Sunlight, clouds, sea ice, albedo, and the radiative budget: the umbrella versus the blanket. *The Cryosphere*, **12**, 2159–2165.

- Perovich, D. K., B. Light, H. Eicken, K. F. Jones, K. Runciman, and S. V. Nghiem, 2007: Increasing solar heating of the arctic ocean and adjacent seas, 1979–2005: Attribution and role in the ice-albedo feedback. *Geophysical Research Letters*, **34**.
- Phojanamongkolkij, N., S. Kato, B. A. Wielicki, P. C. Taylor, and M. G. Mlynczak, 2014: A comparison of climate signal trend detection uncertainty analysis methods. *Journal of climate*, **27**, 3363–3376.
- Pistone, K., I. Eisenman, and V. Ramanathan, 2014: Observational determination of albedo decrease caused by vanishing Arctic sea ice. *Proceedings of the National Academy of Sciences*, **111**, 3322–3326.
- Qu, X. and A. Hall, 2005: Surface contribution to planetary albedo variability in cryosphere regions. *Journal of Climate*, **18**, 5239–5252.
- Rienecker, M. M., M. J. Suarez, R. Gelaro, R. Todling, J. Bacmeister, E. Liu, M. G. Bosilovich, S. D. Schubert, L. Takacs, G.-K. Kim, et al., 2011: Merra: Nasa’s modern-era retrospective analysis for research and applications. *Journal of climate*, **24**, 3624–3648.
- Riihelä, A., T. Manninen, and V. Laine, 2013: Observed changes in the albedo of the Arctic sea-ice zone for the period 1982–2009. *Nature Climate Change*, **3**, 895.
- Screen, J. A. and I. Simmonds, 2010: The central role of diminishing sea ice in recent Arctic temperature amplification. *Nature*, **464**, 1334.
- Sedlar, J., 2018: Spring Arctic atmospheric preconditioning: Do not rule out shortwave radiation just yet. *Journal of Climate*, **31**, 4225–4240.

Sedlar, J., M. Tjernström, T. Mauritsen, M. D. Shupe, I. M. Brooks, P. O. G. Persson, C. E.

Birch, C. Leck, A. Sirevaag, and M. Nicolaus, 2011: A transitioning Arctic surface energy budget: the impacts of solar zenith angle, surface albedo and cloud radiative forcing. *Climate dynamics*, **37**, 1643–1660.

Serreze, M., A. Barrett, J. Stroeve, D. Kindig, and M. Holland, 2009: The emergence of surface-based Arctic amplification. *The Cryosphere*, **3**, 11.

Serreze, M. C. and R. G. Barry, 2011: Processes and impacts of arctic amplification: A research synthesis. *Global and planetary change*, **77**, 85–96.

— 2014: *The Arctic climate system*. Cambridge University Press.

Sledd, A. and T. L’Ecuyer, 2019: How much do clouds mask the impacts of Arctic sea ice and snow cover variations? Different perspectives from observations and reanalyses. *Atmosphere*, **10**, 12.

— 2021: Uncertainty in forced and natural arctic solar absorption variations in cmip6 models. *Journal of Climate*, **34**, 931–948.

Smithson, P., K. Addison, and K. Atkinson, 2013: *Fundamentals of the physical environment*. Routledge.

Soden, B. J., I. M. Held, R. Colman, K. M. Shell, J. T. Kiehl, and C. A. Shields, 2008: Quantifying climate feedbacks using radiative kernels. *Journal of Climate*, **21**, 3504–3520.

Steele, M. and S. Dickinson, 2016: The phenology of a rctic o cean surface warming. *Journal of Geophysical Research: Oceans*, **121**, 6847–6861.

- Steele, M., W. Ermold, and J. Zhang, 2008: Arctic ocean surface warming trends over the past 100 years. *Geophysical Research Letters*, **35**.
- Steele, M., J. Zhang, and W. Ermold, 2010: Mechanisms of summertime upper arctic ocean warming and the effect on sea ice melt. *Journal of Geophysical Research: Oceans*, **115**.
- Stephens, G. L., D. O'Brien, P. J. Webster, P. Pilewski, S. Kato, and J.-l. Li, 2015: The albedo of earth. *Reviews of geophysics*, **53**, 141–163.
- Stroeve, J., J. E. Box, Z. Wang, C. Schaaf, and A. Barrett, 2013: Re-evaluation of modis mcd43 greenland albedo accuracy and trends. *Remote Sensing of Environment*, **138**, 199–214.
- Stroeve, J. C., M. C. Serreze, M. M. Holland, J. E. Kay, J. Malanik, and A. P. Barrett, 2012: The arctic's rapidly shrinking sea ice cover: a research synthesis. *Climatic Change*, **110**, 1005–1027.
- Tanelli, S., S. L. Durden, E. Im, K. S. Pak, D. G. Reinke, P. Partain, J. M. Haynes, and R. T. Marchand, 2008: Cloudsat's cloud profiling radar after two years in orbit: Performance, calibration, and processing. *IEEE Transactions on Geoscience and Remote Sensing*, **46**, 3560–3573.
- Tiao, G. C., G. C. Reinsel, D. Xu, J. Pedrick, X. Zhu, A. Miller, J. DeLuisi, C. Mateer, and D. Wuebbles, 1990: Effects of autocorrelation and temporal sampling schemes on estimates of trend and spatial correlation. *Journal of Geophysical Research: Atmospheres*, **95**, 20507–20517.

- Tiedtke, M., 1993: Representation of clouds in large-scale models. *Monthly Weather Review*, **121**, 3040–3061.
- Tietsche, S., D. Notz, J. Jungclaus, and J. Marotzke, 2011: Recovery mechanisms of Arctic summer sea ice. *Geophysical Research Letters*, **38**.
- Timmermans, M.-L., J. Toole, and R. Krishfield, 2018: Warming of the interior Arctic Ocean linked to sea ice losses at the basin margins. *Science advances*, **4**, eaat6773.
- Tjernström, M., J. Sedlar, and M. D. Shupe, 2008: How well do regional climate models reproduce radiation and clouds in the arctic? an evaluation of arcmip simulations. *Journal of Applied Meteorology and Climatology*, **47**, 2405–2422.
- Uppala, S. M., P. Kållberg, A. Simmons, U. Andrae, V. D. C. Bechtold, M. Fiorino, J. Gibson, J. Haseler, A. Hernandez, G. Kelly, et al., 2005: The era-40 re-analysis. *Quarterly Journal of the royal meteorological society*, **131**, 2961–3012.
- Vignesh, P. P., J. H. Jiang, P. Kishore, H. Su, T. Smay, N. Brighton, and I. Velicogna, 2020: Assessment of CMIP6 cloud fraction and comparison with satellite observations. *Earth and Space Science*, **7**, e2019EA000975.
- Walsh, J. E., W. L. Chapman, and D. H. Portis, 2009: Arctic cloud fraction and radiative fluxes in atmospheric reanalyses. *Journal of Climate*, **22**, 2316–2334.
- Wang, X., J. Key, Y. Liu, C. Fowler, J. Maslanik, and M. Tschudi, 2012: Arctic climate variability and trends from satellite observations. *Advances in Meteorology*, **2012**.

- Wang, X. and J. R. Key, 2005: Arctic climate characteristics and recent trends from space. *Applications with Weather Satellites II*, International Society for Optics and Photonics, volume 5658, 257–268.
- Wang, Y., X. Huang, H. Liang, Y. Sun, Q. Feng, and T. Liang, 2018: Tracking snow variations in the Northern Hemisphere using multi-source remote sensing data (2000–2015). *Remote Sensing*, **10**, 136.
- Weatherhead, E. C., G. C. Reinsel, G. C. Tiao, X.-L. Meng, D. Choi, W.-K. Cheang, T. Keller, J. DeLuisi, D. J. Wuebbles, J. B. Kerr, et al., 1998: Factors affecting the detection of trends: Statistical considerations and applications to environmental data. *Journal of Geophysical Research: Atmospheres*, **103**, 17149–17161.
- Wesslén, C., M. Tjernström, D. Bromwich, G. De Boer, A. M. Ekman, L.-S. Bai, and S.-H. Wang, 2014: The arctic summer atmosphere: an evaluation of reanalyses using ascos data. *Atmospheric Chemistry and Physics*, **14**, 2605–2624.
- Wielicki, B. A., D. Young, M. Mlynczak, K. Thome, S. Leroy, J. Corliss, J. Anderson, C. Ao, R. Bantges, F. Best, et al., 2013: Achieving climate change absolute accuracy in orbit. *Bulletin of the American Meteorological Society*, **94**, 1519–1539.
- Winker, D. M., M. A. Vaughan, A. Omar, Y. Hu, K. A. Powell, Z. Liu, W. H. Hunt, and S. A. Young, 2009: Overview of the calipso mission and caliop data processing algorithms. *Journal of Atmospheric and Oceanic Technology*, **26**, 2310–2323.

Wu, D. L., J. N. Lee, K.-M. Kim, and Y.-K. Lim, 2020: Interannual variations of toa albedo over the arctic, antarctic and tibetan plateau in 2000–2019. *Remote Sensing*, **12**, 1460.

Yeager, S., 2020: The abyssal origins of north atlantic decadal predictability. *Climate Dynamics*, **55**, 2253–2271.

Zelinka, M. D., T. A. Myers, D. T. McCoy, S. Po-Chedley, P. M. Caldwell, P. Ceppi, S. A. Klein, and K. E. Taylor, 2020: Causes of higher climate sensitivity in CMIP6 models. *Geophysical Research Letters*, **47**, e2019GL085782.

Zhang, J. and D. Rothrock, 2003: Modeling global sea ice with a thickness and enthalpy distribution model in generalized curvilinear coordinates. *Monthly Weather Review*, **131**, 845–861.

Zhu, Z., S. Piao, R. B. Myneni, M. Huang, Z. Zeng, J. G. Canadell, P. Ciais, S. Sitch, P. Friedlingstein, A. Arneeth, et al., 2016: Greening of the earth and its drivers. *Nature climate change*, **6**, 791–795.